

©Copyright 2010-2016

Pedro H. Sales de Bruin

Searches for Beyond Standard Model Higgs Bosons in pp collisions
at $\sqrt{s} = 8$ and 13 TeV with the ATLAS detector

Pedro H. Sales de Bruin

A dissertation submitted in partial fulfillment of the
requirements for the degree of

Doctor of Philosophy

University of Washington

2010-2016

Reading Committee:

Anna Goussiou, Chair

Ann Nelson

Shih-Chieh Hsu

Program Authorized to Offer Degree:
Department of Physics

University of Washington

Abstract

Searches for Beyond Standard Model Higgs Bosons in pp collisions at $\sqrt{s} = 8$ and 13 TeV with the ATLAS detector

Pedro H. Sales de Bruin

Chair of the Supervisory Committee:
Professor Anna Goussiou
Department of Physics

The searches for a Beyond Standard Model (BSM) heavy CP-odd Higgs boson A decaying to Zh in the context of two-Higgs-doublet models (2HDM), and Minimal Supersymmetric Standard Model (MSSM) neutral Higgs bosons H/A decaying to a tau pair are presented. The search for the heavy CP-odd Higgs boson, A , is conducted through the $A \rightarrow Zh \rightarrow \ell\ell\tau_{lep}\tau_{had}$ decay channel using 20.3 fb^{-1} of proton-proton collision data collected by the ATLAS detector at a center-of-mass of 8 TeV. The search for the neutral MSSM H/A decaying to a tau pair in the $\tau_{lep}\tau_{had}$ b -veto final state is done using 3.2 fb^{-1} of proton-proton collision data recorded by the ATLAS detector at a center-of-mass of 13 TeV. The observed data agrees with the Standard Model background prediction, and upper limits are set on cross-section times branching ratio of neutral BSM Higgs bosons.

TABLE OF CONTENTS

	Page
List of Figures	iii
List of Tables	ix
Chapter 1: Introduction	1
Chapter 2: Theory	4
2.1 The Standard Model	4
2.2 Two-Higgs-Doublet Models	10
2.3 The MSSM	13
Chapter 3: Apparatus	21
3.1 Overview	21
3.2 The Accelerator Complex	21
3.3 LHC	21
3.4 ATLAS	25
Chapter 4: $A \rightarrow Zh \rightarrow \ell\ell\tau_{lep}\tau_{had}$	36
4.1 Samples	36
4.2 Reconstruction	39
4.3 Event Selection	45
4.4 Background Estimation	46
4.5 Systematic Uncertainties	54
4.6 Results	63
Chapter 5: Neutral MSSM $A/H \rightarrow \tau_{lep}\tau_{had}$	68
5.1 Samples	68
5.2 Reconstruction	70

5.3	Event Selection	72
5.4	Background Estimation	76
5.5	Systematic Uncertainties	101
5.6	Results	109
Chapter 6:	Summary and Conclusion	117
	Bibliography	118
Appendix A:	Tau Identification	125
A.1	Overview	125
A.2	Discriminating variables	128
A.3	Final performance and working points	135
A.4	Updates for Run-2	135
Appendix B:	Statistical Treatment of Results	137
B.1	Overview	137

LIST OF FIGURES

Figure Number	Page	
1.1	The reconstructed invariant mass distribution of $\gamma\gamma$ (a) and $\tau\tau$ (b) events, from References [1] and [7], respectively. The solid red line is a fit to the observed data using a SM Higgs signal hypotheses. Events in (b) are weighted according to a measure of the likelihood they correspond to a signal event, as determined by a multivariate classifier.	2
2.1	The Standard Model of elementary particles.	5
2.2	The Higgs potential with its non-zero vacuum expectation value.	10
2.3	One-loop corrections to the Higgs mass from fermions and a supersymmetric scalar.	11
2.4	The right plot shows the allowed region of the $[X_t, M_S]$ plane of the pMSSM for a range of $\tan\beta$ values, where M_S is the SUSY scale and X_t is the stop mixing parameter. The condition of $X_t/M_S \lesssim 3$ is imposed to avoid a non-viable spectrum of the model. The left plots shows the maximal values of m_h for different X_t/M_S values. Plots from Reference [23].	17
2.5	Masses of the h , H and H^\pm as a function of the mass of the CP-odd A for stop mixing values $X_t = 0$ (left) and $X_t = \sqrt{6}M_S$ (right). Plots from Reference [22].	17
2.6	Production cross sections of neutral Higgs bosons from gluon fusion (a) and b -associated production (b) at 14 TeV. Plots from Reference [22].	19
2.7	Branching ratios of the h , H and A Higgs bosons for $\tan\beta$ values of 5 (left) and 30 (right) in the m_h^{mod+} scenario. Plots from Reference [27].	20
3.1	A schematic overview of the CERN accelerator complex.	22
3.2	The eight sectors of LHC tunnel with the physics experiments depicted. . . .	24
3.3	The ATLAS detector and its subsystems.	26
3.4	Overview of the ATLAS Inner Detector.	27
3.5	IBL structure in the xy plane.	29
3.6	Fractional energy resolution of a barrel LAr calorimeter module as a function of beam energy.	30
3.7	Structural layout of the ATLAS muon spectrometer.	32

3.8	Cross-sectional and longitudinal view of a muon drift tube.	33
3.9	Cross-sectional view of a CSC cell.	34
3.10	Cross-sectional view of the ATLAS muon spectrometer end-cap.	34
4.1	Example distributions of the angular distance between visible and invisible momenta of tau decay products for the cases of 1-track (left), 3-track(middle) and leptonic (right) tau decay types. Plots from Reference [46].	44
4.2	A comparison of $m_{\ell\ell\tau\tau}$ (solid) mass and m_A^{rec} (dashed) for 260 GeV, 500 GeV, 800 GeV and combined background. The background prediction shown here is exclusively from simulated events.	46
4.3	The signal acceptance efficiency for the full $\ell\ell\tau_{lep}\tau_{had}$ selection.	47
4.4	The shape of the reconstructed A boson mass, m_A^{rec} , for events passing in the Higgs sidebands region (a) and the Z sidebands region (b) compared to Region A of Z sidebands and Higgs sidebands respectively. The truth-matched $\ell\ell\tau\tau$ events have been subtracted in both cases.	51
4.5	The shape of the reconstructed A boson mass, m_A^{rec} , for events passing in the Z sidebands region, the Higgs sidebands region and the template region for the full selection. The truth-matched $\ell\ell\tau\tau$ events have been subtracted in both cases.	52
4.6	The default template shape compared to the shape that is obtained if the R1 – R5 control regions are used instead. For more details see in the text.	53
4.7	The reconstructed Z boson mass is shown in (a), while (b) shows the reconstructed h boson mass. Both distributions are for the full signal region selection apart from the Z and h mass window requirements, respectively. Events with true τ_{had} are taken from simulation and events with jets misidentified as τ_{had} are estimated using the template method.	55
4.8	Comparisons of the distributions of kinematic variables for the full background prediction, observed data and a $m_A = 340$ GeV signal sample in the signal region.	56
4.9	The reconstructed A boson mass, m_A^{rec} , for the full $\tau_{lep}\tau_{had}$ selection. The truth-matched background from simulation is shown stacked on the data-normalized template. The signal point shown here corresponds to $\sigma(gg \rightarrow A) \times BR(A \rightarrow Zh \rightarrow \ell\ell\tau\tau) = 1 \text{ fb}^{-1}$. For more details see the text.	64
4.10	Expected and observed 95% CL upper limits of $\sigma(\text{gluon-fusion}) \times BR(A \rightarrow Zh \rightarrow \ell\ell\tau_{lep}\tau_{had})$ as a function of m_A	65
4.11	Excluded parameter space of type-I (a) and type-II (b) 2HDM derived from $A \rightarrow Zh \rightarrow \tau_{lep}\tau_{had}$ search result.	66

4.12	Exclusions in the $\cos(\beta - \alpha) - \tan\beta$ plane of the combined ($\ell\ell\tau\tau$, $\nu\nu\tau\tau$, $bb\tau\tau$) $A \rightarrow Zh$ search for type-I and type-II 2HDM. The blue shaded area is the exclusion provided by the Run-1 $A \rightarrow \tau\tau$ search result. Plots from Reference [52].	67
5.1	Lowest order Feynman diagrams for gluon fusion (a) and b -associated production (b) of a neutral MSSM Higgs boson.	69
5.2	Distribution of the transverse mass $m_T(\ell, E_T^{miss})$ for the (a) $e\tau_{had}$ and (b) $\mu\tau_{had}$ channels.	75
5.3	Visible mass distributions in the $e\tau_{had}$ channel for events with (a) $\eta < 2$ and (b) $ \eta > 2.3$, after applying the η_τ -dependent scale factor	79
5.4	Scale factors for misidentified e -to- τ_{had} events.	80
5.5	Distributions of $m_T(\ell, \tau_{had})$ for events with one-prong (a) and three-prong (b) τ_{had} before the $m_T(\ell, E_T^{miss})$ cut requirement.	81
5.6	Distributions of the total transverse mass for events with one-prong (a) and three-prong (b) τ_{had}	81
5.7	The $M_T(\ell, E_T^{miss})$ of the W +jets control region after preselection in the (a) electron and (b) muon channel, respectively. The E_T^{miss} distributions after the full W +jets control region selection is shown in (c) and (d). Only MC samples are shown for the prediction and no multi-jet estimation is included. The signal plotted here is $m_\phi = 600$ GeV, gluon-fusion produced with a cross section times branching ratio of 100 pb (far beyond the excluded region of the MSSM, which is below 0.1 pb.)	84
5.8	Distributions of $m_T(\ell, E_T^{miss})$ for events (a,b) passing and (c,d) failing the τ_{had} identification requirement in the W +jets control region and 1-prong τ_{had} . Only MC samples are shown for the prediction, no multi-jet estimation is included. The signal plotted here is $m_\phi = 600$ GeV, gluon-fusion produced with a cross section times branching ratio of 100 pb.	85
5.9	Distributions of $m_T(\ell, E_T^{miss})$ for events (a,b) passing and (c,d) failing the τ_{had} identification requirement in the W +jets control region and 3-prong τ_{had} . Only MC samples are shown for the prediction. No multi-jet estimation is included. The signal plotted here is $m_\phi = 600$ GeV, gluon-fusion produced with a cross section times branching ratio of 100 pb.	86

5.10	Fake factors from the W +jets control region (with b-veto) as a function of $p_T(\tau_{had})$ calculated in data for (a) 1-prong and (b) 3-prong τ_{had} candidates shown with red circular markers. The ratio of the signal region over the anti- τ_{had} region after subtracting the true backgrounds from simulations is shown for comparison. In (c,d) and (e,f) the same plots for the electron and the muon channel, respectively are shown.	87
5.11	Some distributions in the W +jets control region of $\Delta\phi(\tau, E_T^{miss})$ for truth-subtracted data passing τ identification and the prediction of τ fakes from the anti- τ region.	88
5.12	Correction scale factors that are applied to the W +jets fake factors as a function of $\Delta\phi(\tau, E_T^{miss})$. The scale factors are shown for the (a) $e\tau_{had}$, (b) $\mu\tau_{had}$ channels and (c) combined channels. ,	89
5.13	Distribution of the total transverse mass in the high $m_T(\ell, E_T^{miss})$ region for the inclusive $e\tau_{had} + \mu\tau_{had}$ channels.	90
5.14	Fake factors for jets from multi-jet events misidentified as τ_{had} . Fake factors are shown as a function of p_T , for 1-prong and 3-prong τ , with (left) statistical uncertainty only and (right) all statistical and systematic uncertainties with the exception of the uncertainty on the denominator definition (evaluated by varying the jet BDT cut).	94
5.15	The transverse mass of the lepton and missing transverse momentum in the fake lepton region for e and μ channels combined, (a) with the anti-isolation applied and (b) with the isolation requirement applied, but without the cuts on jet multiplicity and transverse mass applied.	96
5.16	The number of jets in the fake lepton region for the $e\tau_{had}$ (a) and $\mu\tau_{had}$ (b) channels with no requirement on the lepton isolation.	97
5.17	Fake factors from the fake lepton control region as a function of lepton η for (a) electrons, (b) muons with $p_T < 55$ GeV and (c) muons with $p_T > 55$ GeV.	98
5.18	The trend of r_{QCD} as a function of τp_T at the end of the event selection, along with the total up and down shifts for the uncertainties, shown separately for (left) the muon and (right) the electron channels.	99
5.19	$\Delta\Phi(l, MET)$ distribution in (a) ehad 1 prong, (b) muHad 1 prong, (c) ehad 3 prong, (d) muhad 3 prong: The blue curve are the events passing TauID selection in the anti-lepton-isolation region. The red one there is for events that failed TauID but weighted with the fake factor.	100
5.20	The transverse mass between the lepton and the E_T^{miss} before the $m_T(\ell, E_T^{miss})$ requirement for the electron (a) and the muon (b) channel.	101

5.21	The distributions of $\Delta\phi(\tau_{had}, E_T^{miss})$ (a,b) and number of tau tracks (c,d) for the full selection in the $e\tau_{had}$ and $\mu\tau_{had}$ channels.	102
5.22	Final distributions of the total transverse mass for $e\tau_{had}$ (a), $\mu\tau_{had}$ (b) and inclusive (c) categories.	110
5.23	Distributions in the electron and muon channels of the $\tau_{had}p_T$, lepton p_T , E_T^{miss} and visible mass. The background predictions and uncertainties used are from the likelihood fit result (see Appendix B).	111
5.24	Distributions in the electron and muon channels of the $\tau_{had}p_T$, lepton p_T , E_T^{miss} and visible mass. The background predictions and uncertainties used are from the likelihood fit result (see Appendix B).	112
5.25	The 95% CL upper limit on the production times branching ratio to $\tau\tau$ of a single scalar boson produced via gluon fusion or b-associated production for 3210 pb^{-1} of integrated luminosity at 13 TeV.	113
5.26	The 95% CL upper limit on the production times branching ratio to $\tau\tau$ of a single scalar boson produced via gluon fusion or b-associated production for 3210 pb^{-1} of integrated luminosity at 13 TeV. Each channel in the b-veto category is shown separately.	114
5.27	Interpretation of the results in the m_h^{mod+} scenario of the MSSM.	115
5.28	Comparison of the exclusion in the $m_A - \tan\beta$ plane of the m_h^{max} scenario for the combined $(\tau_{lep}\tau_{had} + \tau_{had}\tau_{had})$ Run-2 $H/A \rightarrow \tau\tau$ search and the Run-1 and preliminary Run-2 results (labeled ‘‘EOYE’’).	116
A.1	A typical BDT score distribution from the TauID classifier (left) and an over-trained BDT from an early iteration of the TauID (right), where the background rejection with events used for training was higher than for events used for testing.	127
A.2	Distributions of the variables used in the training of the Run-1 TauID classifier of 1-track hadronic taus.	130
A.3	Distributions of the variables used in the training of the Run-1 TauID classifier of 1-track hadronic taus.	131
A.4	Distributions of the variables used in the training of the Run-1 TauID classifier of 3-track hadronic taus.	132
A.5	Distributions of the variables used in the training of the Run-1 TauID classifier of 3-track hadronic taus.	133
A.6	The signal efficiency as a function of the reconstructed number of primary vertices for 1-track (a) and 3-track (b) hadronic taus.	135

A.7	The background rejection as a function of the signal efficiency for low ($p_T < 40$ GeV) and high ($p_T > 40$ GeV). transverse momenta hadronic taus. Red markers indicate the three efficiency working points described in the text.	136
B.1	Nuisance parameter rankings in the $e\tau_{had}$ channel for signal mass hypothesis of 300 and 1000 GeV.	140
B.2	Nuisance parameter rankings in the $\mu\tau_{had}$ (bottom) channel for signal mass hypothesis of 300 and 1000 GeV.	141

LIST OF TABLES

Table Number	Page
2.1 Yukawa couplings of leptons, vector bosons and <i>up</i> and <i>down</i> -type quarks to the neutral Higgs bosons h , H and A for 2HDMs of type-I and type-II. . . .	14
3.1 Parameters of the ATLAS calorimeter.	31
4.1 Cross sections and branching ratios at different m_A hypotheses for type-I 2HDM.	37
4.2 Cross sections and branching ratios at different m_A hypotheses for type-II 2HDM.	38
4.3 Number of events passing the $\tau_{lep}\tau_{had}$ channel selection in the template control region. For a better overview, the events are also split in regions B ($\tau_{lep}\tau_{had}$ is SS, τ_{had} passes TauID), C ($\tau_{lep}\tau_{had}$ is OS, τ_{had} fails TauID) and D ($\tau_{lep}\tau_{had}$ is SS, τ_{had} fails TauID). The signal region is also shown for comparison. Signal numbers assume $\sigma(gg \rightarrow A) \times BR(A \rightarrow Zh \rightarrow ll\tau\tau) = 1$ fb.	48
4.4 Number of events passing the $\tau_{lep}\tau_{had}$ channel selection in the Higgs sidebands control region. For a better overview, the events are also split in regions B ($\tau_{lep}\tau_{had}$ is SS, τ_{had} passes TauID), C ($\tau_{lep}\tau_{had}$ is OS, τ_{had} fails TauID) and D ($\tau_{lep}\tau_{had}$ is SS, τ_{had} fails TauID). Region A is defined such that all the requirements of the signal region are satisfied apart from the Higgs mass window constrain. Signal numbers assume $\sigma(gg \rightarrow A) \times BR(A \rightarrow Zh \rightarrow ll\tau\tau) = 1$ fb.	49
4.5 Normalization factors and predicted event yields for the nominal and alternate definitions of the template region. Regions R4 and R5 have loose Higgs lepton in the control regions (but passing Medium ID in signal region). This study was conducted using a different generator for the diboson background, so there is a slight shift compared to quoted values in the text. The uncertainties quoted here are due to the data statistics and the finite number of generated MC. The uncertainty of the predicted yield that stems from the calculation of the normalization factor is shown second.	54
4.6 Table showing the up and down detector systematic fluctuations of the $\tau_{lep}\tau_{had}$ MC signal and background samples after full selection, along with the corresponding statistical uncertainty	58

4.7	Factorization/Renormalization shift up uncertainty on acceptance of lephad channel	59
4.8	Factorization/Renormalization shift down uncertainty on acceptance of lephad channel	60
4.9	ISR shift up uncertainty on acceptance of lephad channel	60
4.10	ISR shift down uncertainty on acceptance of lephad channel	60
4.11	acceptance uncertainties on NNPDF21_lo_as_0119_100 PDF of lephad channel	61
4.12	acceptance uncertainties on MSTW2008lo68cl PDF of lephad channel	61
4.13	Overview of the $\tau_{lep}\tau_{had}$ channel systematic uncertainties as implemented in the fit model.	62
4.14	Final event yields of the $A \rightarrow Zh \rightarrow \ell\ell\tau_{lep}\tau_{had}$ search. The signal is given for a mass of 300 GeV, and assuming a cross section times branching ratio of 10 fb ⁻¹	64
5.1	Electron channel cutflow. The predictions correspond to a luminosity of 3.2 fb ⁻¹ . The errors are due solely to the finite number of simulated events.	75
5.2	Electron channel cutflow for signal samples. The predictions correspond to a luminosity of 3.2 fb ⁻¹ and a cross section of 1 pb ⁻¹ . The errors are due solely to the finite number of simulated events.	76
5.3	Muon channel cutflow. The predictions correspond to a luminosity of 3.2 fb ⁻¹ . The errors are due solely to the finite number of simulated events.	77
5.4	Muon channel cutflow for signal samples. The predictions correspond to a luminosity of 3.2 fb ⁻¹ and a cross section of 1 pb ⁻¹ . The errors are due solely to the finite number of simulated events.	78
5.5	Relative difference between W +jets fake factors computed in the high and low $m_T(\ell, E_T^{miss})$ regions for 1-prong and 3-prong separately	91
5.6	W +jets b-veto control region composition for 1-prong τ_{had}	92
5.7	W +jets b-veto control region composition for 3-prong τ_{had}	92
5.8	Events in the fake lepton region. The numbers correspond to an integrated luminosity of 3.2 fb ⁻¹ . The quoted uncertainties are due to the finite number of generated events in the simulated samples.	97
5.9	The effect of the systematic uncertainties in the MC samples used for the background estimation for the $e\tau_{had}$, b -veto category. The effect on the normalization in % is shown per sample.	104

5.10	The effect of the systematic uncertainties in the MC samples used for the background estimation for the $\mu\tau_{had}$, b -veto category. The effect on the normalization in % is shown per sample.	104
5.11	The effect of the systematic uncertainties in the MC samples used signal events in the $e\tau_{had}$, b -veto category. The effect on the normalization in % is shown per sample.	105
5.12	The effect of the systematic uncertainties in the MC samples used for signal events in the $\mu\tau_{had}$, b -veto category. The effect on the normalization in % is shown per sample.	106
5.13	Summary of uncertainties of ggH lephad signal samples in bveto category.	107
5.14	Summary of uncertainties of bbH lephad signal samples in bveto category.	108
A.1	The list of variables used by the Run-1 TauID algorithm. The bullets indicate whether the variable is used in the training of the 1-track and/or 3-track classifier.	134

ACKNOWLEDGMENTS

I would first like to thank my advisor, Anna Goussiou, who provided me with precious guidance and support throughout my PhD. Special thanks also to Nikolaos Rompotis, whose constant help has been instrumental in all of the achievements of my graduate career. Many thanks to my colleagues in the Higgs and tau groups, with whom I have had the great fortune of collaborating with. Sincere thanks to my parents, not only for making this possible but also for showing me the value of scientific thought. Lastly, thanks to my wife, Emily, whose constant support helped me endure the stresses of graduate life.

DEDICATION

To my grandparents, Henricus and Iêda.

Chapter 1

INTRODUCTION

The Standard Model (SM) is currently the most complete theory of fundamental particles and their interactions. Despite its success, the SM fails to explain, among other things, the presence of Dark Matter, gravity, and the matter-antimatter asymmetry of the universe, and suffers from severe fine-tuning of some of its parameters. Therefore, it must be extended with compatible “Beyond Standard Models” (BSM) if we are to have a complete and unified description of particle physics.

On July 4th, 2012, the observation of a new particle was announced by the ATLAS and CMS experiments [1, 2]. Subsequent studies done in both ATLAS and CMS have found that the new particle is compatible with the SM Higgs boson, h [3, 4, 5, 6]. The discovery was realized by detecting a 125 GeV resonance in the invariant mass spectrum of diphoton, shown in Figure 1.1, as well as WW and ZZ events. Strong supporting evidence has also been found in the $h \rightarrow \tau\tau$ channel [7]. Searches in the $h \rightarrow bb$ channel have also been carried out [8, 9], but the large multijet background at the LHC have hindered a discovery in that channel.

The existence of the Higgs field was first predicted in 1964, almost 50 years prior to its discovery, by P. Higgs [10, 11, 12], F. Englert and R. Brout [13], and G. Guralnik, C.R. Hagen, and T. Kibble [14]. Their influential work showed that adding a doublet of complex scalar fields leads to the spontaneous breaking of the gauge symmetry of the SM electroweak sector, which in turn explains why the W and Z vector bosons are massive particles. The process of electroweak symmetry breaking (EWSB) through the addition of this Higgs field is known as the “Higgs Mechanism”. The observation of the h boson was the last fundamental particle required in the construction of the SM and has become a crowning achievement of

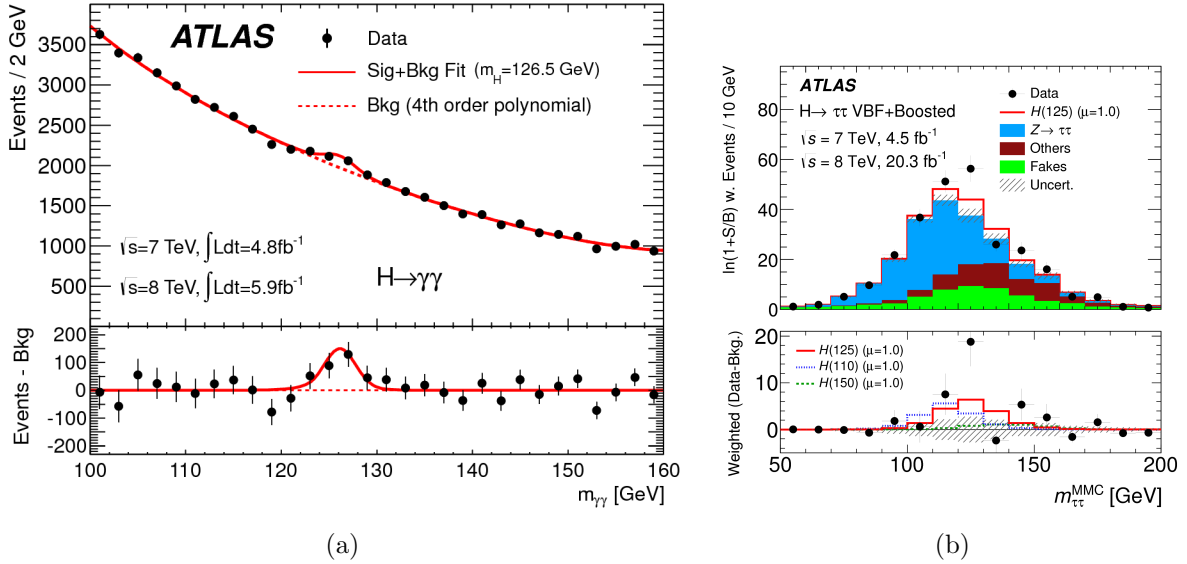


Figure 1.1: The reconstructed invariant mass distribution of $\gamma\gamma$ (a) and $\tau\tau$ (b) events, from References [1] and [7], respectively. The solid red line is a fit to the observed data using a SM Higgs signal hypotheses. Events in (b) are weighted according to a measure of the likelihood they correspond to a signal event, as determined by a multivariate classifier.

25 decades of work from particle theorists and experimentalists.

26 As we will see in Chapter 2, the Higgs boson has radiative corrections that tend to
 27 make it far heavier than its observed mass, necessitating heavy fine-tuning of its parameters
 28 to give the observed mass. This is called the naturalness problem. An early proposed
 29 solution to it was the imposition of an additional symmetry to the SM called Supersymmetry
 30 [15, 16, 17]. The Minimal Supersymmetric Standard Model (MSSM) is a popular theory
 31 because it achieves supersymmetry through minimal modifications to the SM [18]. It belongs
 32 to a larger class of models that have an extended Higgs sector containing an additional
 33 Higgs doublet, named Two-Higgs-Doublet Models (2HDM) [19]. In 2HDM there are five
 34 predicted Higgs bosons: two that are CP -even, h and H , one that is CP -odd, A , and two
 35 charged scalars, H^\pm . In this thesis, two BSM Higgs searches are described: the search for
 36 a heavy CP -odd neutral Higgs boson, A , decaying to Zh , and the search for heavy neutral
 37 MSSM Higgs bosons decaying to a tau-lepton pair. The $A \rightarrow Zh$ search is conducted in

38 the $Z \rightarrow \ell\ell$, $h \rightarrow \tau_{lep}\tau_{had}$ final state ($\ell = e, \mu$), where τ_{lep} and τ_{had} denote leptonically and
39 hadronically decaying taus, respectively. The MSSM $H/A \rightarrow \tau\tau$ is also done in the $\tau_{lep}\tau_{had}$
40 final state and focuses on events without b -tagged jets.

41 The layout of this document is as follows: Chapter 2 contains a description of the
42 Standard Model, as well as the BSM theories relevant to the work, Chapter 3 provides
43 details on the Large Hadron Collider and the ATLAS detector, Chapter 4 describes the
44 $A \rightarrow Zh \rightarrow \ell\ell\tau_{lep}\tau_{had}$ analysis, Chapter 5 describes the MSSM $H/A \rightarrow \tau_{lep}\tau_{had}$ analysis,
45 and Chapter 6 contains a short summary. The analysis chapters are further subdivided into
46 subsections concerning (in order of appearance): the data and simulated samples used, the
47 techniques developed by ATLAS to reconstruct particle objects, the event selection criteria
48 used to maximize a potential signal detection, the methods to describe the background events
49 passing our selection, and finally the search results. Finally, Appendices A and B describe
50 the τ_{had} identification algorithm and the statistical procedure used to interpret the results.

Chapter 2

THEORY

2.1 *The Standard Model*

The Standard Model (SM) of particle physics is the prevailing theory of particles and their interactions. It successfully explains and predicts many phenomena of particles physics, a large fraction of which have been experimentally confirmed. The SM is essentially a unified theoretical description of three different forces of nature: the strong force, the weak force, and electromagnetism. The gravitational force has not yet been explained in the context of the SM.

It is illuminating to present the fundamental aspects of the SM in terms of its particle content. All fundamental particles described in the SM can be categorized into the following groups: particles with half-integer spin called fermions (which are divided into leptons and quarks), and particles with integer spin called bosons. There are six types of quarks: the 1st generation *up* (u) and *down* (d), the 2nd generation *charm* (c) and *strange* (s), and the 3rd generation *bottom* (b) and *top* (t). The lepton group is also composed of three generations: electrons (e), muons (μ), taus (τ), and their respective neutrinos (ν_e, ν_μ, ν_τ). All fundamental particles are also predicted to have antiparticles with opposite electrical charge, effectively doubling the particle content of the SM.

Formally, SM interactions are described by gauge-invariant quantum fields, meaning they are invariant under a continuous group of local transformations. The quanta of the gauge fields are the gauge bosons. These are the photon, γ , the vector bosons W and Z , the gluons g , and finally the Higgs boson, h . For a summary of the SM particles, see Figure 2.1

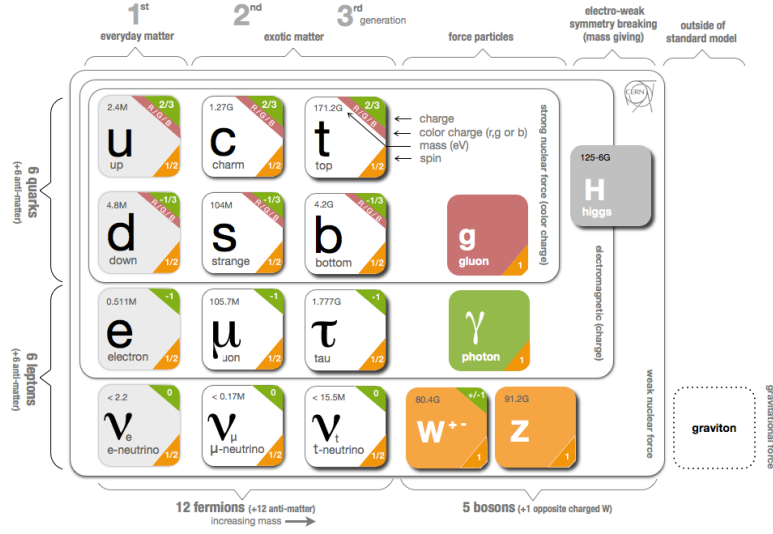


Figure 2.1: The Standard Model of elementary particles.

73 2.1.1 The Strong Sector

74 The description of strong interactions in the SM is done by Quantum Chromodynamics
 75 (QCD), a gauge theory with SU(3) symmetry [20]. Only quarks and gluons interact via the
 76 strong force. The QCD lagrangian is given by

$$\mathcal{L} = \bar{\psi}_q^i (i\gamma^\mu) (D_\mu)_{ij} \psi_q^j - \frac{1}{4} G_{\mu\nu}^a G_a^{\mu\nu}, \quad (2.1)$$

77 where ψ_q^i is the field of a quark q with color index i , $\bar{\psi}_q^i \equiv \psi_q^\dagger \gamma^0$ is its Dirac adjoint, γ^μ are
 78 the Dirac matrices, $G_{\mu\nu}^a$ is the field-strength tensor of a gluon with color a ($a = 1, \dots, 8$). The
 79 term D_μ is the covariant derivative that maintains gauge invariance under SU(3), given by

$$(D_\mu)_{ij} = \delta_{ij} \partial_\mu - \frac{1}{2} i g_s \lambda_{ij}^a G_\mu^a, \quad (2.2)$$

80 where g_s is the coupling of the strong force, G_μ^a the field of a gluon with color a , and λ_{ij}^a
 81 traceless and hermitian matrices that are the generators of the fundamental representation
 82 of SU(3), also known as the Gell-Mann matrices.

83 An interesting property of QCD is how the coupling strength parameter α_s changes (or
84 “runs”) with the energy scale (Q), a dependency given by the *beta function*:

$$\beta(\alpha_s) \equiv Q^2 \frac{\partial \alpha_s}{\partial Q^2} = -\alpha_s^2 (b_0 + b_1 \alpha_s + b_2 \alpha_s^2 + \dots), \quad (2.3)$$

85 where b_0, b_1, \dots are the coefficients of processes at leading order (LO), next-to-leading order
86 (NLO), and so on. The b_i parameters depend only on the number of quark states accessible,
87 and the LO and NLO terms are

$$b_0 = \frac{33 - 2n_f}{12\pi}, \quad (2.4)$$

88

$$b_1 = \frac{153 - 19n_f}{24\pi^2}, \quad (2.5)$$

89 where n_f is the number of quark states accessible at the energy scale Q . Note that if $n_f < 16$,
90 then b_0 is positive such that the coupling strength α_s gets progressively smaller as we go to
91 higher energies. This property of QCD is called *asymptotic freedom*. Opposite to this effect
92 is the fact that the interaction energy between partons does not vanish at large distances but
93 continues to grow, so that it is energetically more favorable for the QCD potential to generate
94 new quark-antiquark pairs than to allow indefinite separation of color-charged particles. This
95 leads to the phenomenon of *confinement*, where quarks and gluons cannot be isolated, but
96 instead decay into collimated showers of colorless hadrons, a process called hadronization.
97 The top quark is an exception to this rule because it may decay before it hadronizes. The
98 reconstructed objects from these hadronic decays are referred to as *jets*.

99 2.1.2 The Electroweak Sector

100 In modern particle theory, electromagnetism and the weak force are unified under the
101 Glashow-Weinberg-Salam (GSW) model [21]. The gauge-covariant formulation of the GSW
102 model is based on the symmetry group $SU(2) \times U(1)$. The generator of the $U(1)$ group is the
103 weak hypercharge operator, \hat{Y} , and the generators of the $SU(2)$ group are the weak isospin
104 operators, \hat{T} . Leptons are represented according to their helicity: right-handed leptons are

105 isospin singlets ($T = 0$), while left-handed leptons are isospin doublets ($T = \frac{1}{2}$, $T_3 = \pm\frac{1}{2}$).

$$L_\ell = \frac{1 - \gamma_5}{2} \begin{pmatrix} \psi_{\nu_\ell} \\ \psi_\ell \end{pmatrix}, \quad R_\ell = \frac{1 + \gamma_5}{2} \psi_\ell \quad (2.6)$$

106 Requiring the invariance of the theory with respect to gauge transformations leads to the
107 introduction of two isovector fields: A_μ and B_μ . The lagrangian density of the electroweak
108 sector can then be written as

$$\mathcal{L}_{\text{EW}} = \bar{L}_\ell \gamma^\mu i D_\mu L_\ell + \bar{R}_\ell \gamma^\mu i D_\mu R_\ell - \frac{1}{4} F_{\mu\nu} F^{\mu\nu} - \frac{1}{4} B_{\mu\nu} B^{\mu\nu}. \quad (2.7)$$

109 In the equation above, γ^μ are the Dirac matrices and $F_{\mu\nu} = \partial_\mu A_\nu - \partial_\nu A_\mu + g A_\mu \times A_\nu$ and
110 $B_{\mu\nu} = \partial_\mu B_\nu - \partial_\nu B_\mu$ are the field-strength tensors. The covariant derivative is introduced so
111 that the kinetic terms in Equation 2.7 are gauge invariant. It is given by

$$D_\mu = \partial_\mu - ig \hat{T} \cdot A_\mu - i \frac{g'}{2} \hat{Y} B_\mu, \quad (2.8)$$

112 where g and g' are the coupling strengths to A_μ and B_μ . The fields for the physical Z and
113 W^\pm bosons are a mixture of A_μ and B_μ according to the Weinberg angle θ :

$$Z_\mu = -\sin(\theta) B_\mu + \cos(\theta) A_\mu^3 \quad (2.9)$$

114 and

$$W_\mu^\pm = \frac{1}{\sqrt{2}} (A_\mu^1 \mp i A_\mu^2). \quad (2.10)$$

115 2.1.3 The Higgs Mechanism

116 Up to now, the electroweak gauge bosons γ , Z_μ and W^\pm have been treated as massless in
117 order to preserve the gauge symmetry. However, the weak force is known to have a very
118 short range, and thus large masses for the particles that propagate it. The solution to this
119 problem is to add a new field that breaks the $SU(2)_L \times U(1)$ gauge symmetry of the GSW
120 model and gives mass to the vector bosons dynamically. This process is known as the Higgs
121 mechanism.

122 Consider the Higgs field, a weak isospin doublet ($T = \frac{1}{2}$, $T_3 = \pm\frac{1}{2}$) of complex scalar
 123 fields

$$\Phi = \begin{pmatrix} \phi^+ \\ \phi^0 \end{pmatrix} \quad (2.11)$$

124 where $\phi^{+(0)}$ has a positive (neutral) electric charge and hypercharge $Y = 1$. The Higgs
 125 lagrangian is then

$$\mathcal{L}_{\text{Higgs}} = |D_\mu \Phi|^2 - U(\Phi), \quad (2.12)$$

126 where D_μ is the covariant derivative of Equation 2.8, and the energy potential $U(\Phi)$ is given
 127 by

$$U(\Phi) = -\mu^2 |\Phi|^2 + h\Phi^4, \quad (2.13)$$

128 where $\mu^2 > 0$ and $h > 0$. The Higgs potential above has a ‘‘Mexican hat’’ shape, as shown in
 129 Figure 2.2. An interesting property of such a potential is that the minima occur for non-zero
 130 values of the field. Thus, the Higgs field is said to have a positive *vacuum expectation value*
 131 (vev). Without restricting generality, we can set the top isospin component to zero by a
 132 suitable gauge choice. In this gauge, the bottom neutral component becomes

$$\phi' = \frac{1}{\sqrt{2}}(\lambda + \chi(x)) \begin{pmatrix} 0 \\ 1 \end{pmatrix}, \quad (2.14)$$

133 where $\lambda = \sqrt{\frac{\mu^2}{h}}$ is the non-zero vev of the field and $\chi(x)$ are local deviations from it. Thus,
 134 Equation 2.13 becomes (dropping constant terms):

$$V(\chi) = h\lambda^2 \chi^2 + h\lambda \chi^3 + \frac{h}{4} \chi^4. \quad (2.15)$$

135 The field $\chi(x)$ corresponds to excitations of the field around the vev, and represents a new
 136 boson called the Higgs boson. Equation 2.15 shows the Higgs boson has mass ($m_h = \sqrt{2h\lambda^2}$)
 137 and is self-interacting.

138 The lepton masses are generated dynamically by their interaction with the Higgs field:

$$\mathcal{L}_{\ell\text{-Higgs}} = -\sqrt{2}m_\ell(\bar{R}_\ell\Phi^\dagger L_\ell + \bar{L}_\ell\Phi R_\ell), \quad (2.16)$$

139 where $m_\ell = f_\ell/\lambda$ is the charged lepton mass. The relation shown in Equation 2.16 is called
 140 the *Yukawa* interaction for leptons. The Yukawa interaction is a general interaction between
 141 a scalar field and a Dirac (fermionic) field, so that there is a corresponding Yukawa term for
 142 quarks.

143 With the addition of this Higgs sector, the combined $\mathcal{L}_{\text{QCD}} + \mathcal{L}_{\text{EW}} + \mathcal{L}_{\text{Higgs}}$ lagrangian
 144 becomes

$$\begin{aligned} \mathcal{L}_{\text{SM}} = & \bar{\psi}_q^i (i\gamma^\mu) (D_\mu)_{ij} \psi_q^j - m_q \bar{\psi}_q^i \psi_{qi} - \frac{1}{4} G_{\mu\nu}^a G_a^{\mu\nu} \\ & + \bar{L}_\ell \gamma^\mu i D_\mu L_\ell + \bar{R}_\ell \gamma^\mu i D_\mu R_\ell - \frac{1}{4} F_{\mu\nu} \cdot F^{\mu\nu} - \frac{1}{4} B_{\mu\nu} B^{\mu\nu} \\ & + |D_\mu \Phi|^2 + \mu^2 |\Phi|^2 - h \Phi^4 \end{aligned} \quad (2.17)$$

145 Using the perturbative expansion of Equation 2.14, combined with Equation 2.8, this be-
 146 comes

$$\begin{aligned} \mathcal{L}_{\text{SM}} = & \bar{\psi}_q^i (i\gamma^\mu) (D_\mu)_{ij} \psi_q^j - f_q \bar{\psi}_q^i \psi_{qi} (\lambda + \chi) - \frac{1}{4} G_{\mu\nu}^a G_a^{\mu\nu} \\ & + -\frac{1}{4} F_{\mu\nu} \cdot F^{\mu\nu} - \frac{1}{4} B_{\mu\nu} B^{\mu\nu} - e \left(\sum_\ell \bar{\psi}_\ell \gamma^\mu \psi_\ell \right) A_\mu \\ & + \sum_\ell i \left(\bar{\psi}_{\nu_\ell} \gamma^\mu \frac{1}{2} (1 - \gamma_5) \partial_\mu \psi_{\nu_\ell} + i \bar{\psi}_\ell \gamma^\mu \partial_\mu \psi_\ell - f_\ell \bar{\psi}_\ell \psi_\ell (\lambda + \chi) \right) \\ & + \frac{g}{2\sqrt{2}} \sum_\ell [\bar{\psi}_\ell \gamma^\mu (1 - \gamma_5) \psi_{\nu_\ell} W_\mu^- + \bar{\psi}_{\nu_\ell} \gamma^\mu (1 - \gamma_5) \psi_\ell W_\mu^+] \\ & + \frac{6}{4 \cos \theta} \sum_\ell [\bar{\psi}_{\nu_\ell} \gamma^\mu (1 - \gamma_5) \psi_{\nu_\ell} - \bar{\psi}_\ell \gamma^\mu (g'_V - \gamma_5) \psi_\ell] Z_\mu \\ & + \frac{h\lambda^4}{4} + \frac{1}{2} (\partial_\mu \chi)^2 - h\lambda^2 \chi^2 - h\chi^2 (\lambda\chi + \frac{1}{4} \chi^2) \\ & + \frac{g^2}{8} (2W_\mu^+ W^{-\mu} + \frac{Z_\mu Z^\mu}{\cos^2 \theta}) (\lambda + \chi)^2, \end{aligned} \quad (2.18)$$

147 where $e = g \sin \theta$, $f_\ell = m_\ell/\lambda$ is the coupling of the leptons to the Higgs field, $f_q = m_q/\lambda$ the
 148 coupling to quarks, and $g'_V = 1 - \sin^2 \theta$. Notice the coupling of fermions to the Higgs field
 149 scales with fermion mass. The last term contains the mass terms for the W^\pm and Z bosons,
 150 given by

$$M_W = \frac{g\lambda}{2} \quad (2.19)$$

151 and

$$M_Z = \frac{M_W}{\cos \theta} \quad (2.20)$$

152 One last remark is that the Higgs field does not couple with the electromagnetic field A_μ ,
 153 which leads to the desired result of the photon remaining massless.

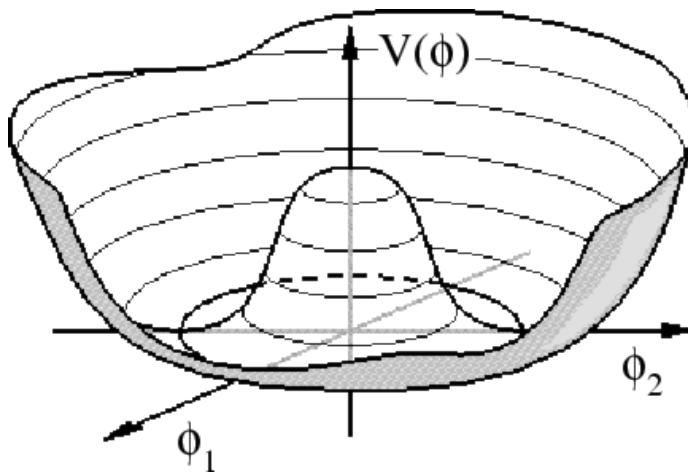


Figure 2.2: The Higgs potential with its non-zero vacuum expectation value.

154 2.2 Two-Higgs-Doublet Models

155 The Higgs sector presented in the previous section has the simplest possible structure that
 156 solves the issue of massless electroweak gauge bosons, with just a single $SU(2)$ doublet.
 157 However, there are many reasons to consider more complex structures.

158 One of them is the so-called *Hierarchy Problem*, the question of why the electroweak
 159 scale (≈ 246 GeV) are so much lower than the Planck scale (10^{19} GeV). Alternatively, it
 160 can be formulated as why is the Higgs mass 125 GeV if the quantum corrections from the
 161 Higgs coupling to heavy fermions are so great. For example, the one-loop diagrams from the
 162 interaction of the Higgs with fermions will give a correction that goes quadratically with the
 163 scale of new physics. If this scale were to be the Planck scale, then the corrections would
 164 be $\Delta m_h^2 \sim 10^{38}$ GeV, more than 30 orders of magnitude higher than the physical Higgs

165 mass. This is fixed only by the *unnatural*, fine-tuned solution where the bare mass of the
 166 Higgs is also on the order of the Planck scale, leading to large cancellations of these radiative
 167 corrections. A more natural way to explain the low value of the Higgs mass is to assume
 168 there is a symmetry that stabilizes the Higgs mass, called Supersymmetry (SUSY).

169 In SUSY, the quantum corrections to the Higgs mass from fermion loops have matching
 170 corrections from scalar superpartners that cancel each other, as shown in Figure 2.3. How-
 171 ever, the simplest SM-compatible supersymmetric theory requires the addition of a second
 172 scalar doublet to the SM Higgs sector, making it part of a larger class of models called two-
 173 Higgs-doublet models (2HDM). There are additional motivations for 2HDMs, as they can be
 174 used to explain the baryon asymmetry of the universe through new sources of CP-violation,
 175 and in axion models that solve the strong CP problem.

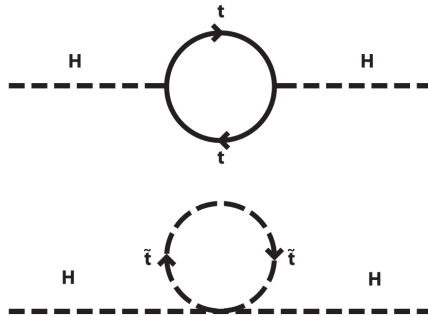


Figure 2.3: One-loop corrections to the Higgs mass from fermions and a supersymmetric scalar.

176 A general 2HDM scalar sector contains 14 parameters, but for a phenomenologically
 177 minded model we can simplify it by requiring it to be CP-conserving and that CP is not
 178 spontaneously broken. Another important note on 2HDMs is that, in general, their Yukawa
 179 terms allow for flavor-changing neutral currents (FCNC) at tree-level which would not be
 180 compatible with experimental observation. However, the FCNC can be naturally suppressed
 181 by imposing discrete symmetries to the lagrangian that remove quartic terms with an odd

182 number of either doublet. With those restrictions in mind, the most general 2HDM potential
 183 we can build, in terms of the doublets Φ_1 and Φ_2 , is

$$\begin{aligned}
 V = & m_{11}^2 \Phi_1^\dagger \Phi_1 + m_{22}^2 \Phi_2^\dagger \Phi_2 - m_{12}^2 (\Phi_1^\dagger \Phi_2 + \Phi_2^\dagger \Phi_1) + \frac{\lambda_1}{2} (\Phi_1^\dagger \Phi_1)^2 + \frac{\lambda_2}{2} (\Phi_2^\dagger \Phi_2)^2 \\
 & + \lambda_3 \Phi_1^\dagger \Phi_1 \Phi_2^\dagger \Phi_2 + \lambda_4 \Phi_1^\dagger \Phi_2 \Phi_2^\dagger \Phi_1 + \frac{\lambda_5}{2} \left[(\Phi_1^\dagger \Phi_2)^2 + (\Phi_2^\dagger \Phi_1)^2 \right].
 \end{aligned}
 \tag{2.21}$$

184 We can minimize V just as we did in Equation 2.14, obtaining

$$\phi'_1 = \frac{v_1}{\sqrt{2}} \begin{pmatrix} 0 \\ 1 \end{pmatrix}, \quad \phi'_2 = \frac{v_2}{\sqrt{2}} \begin{pmatrix} 0 \\ 1 \end{pmatrix},
 \tag{2.22}$$

185 where v_1 and v_2 are the vev's of the two scalar fields. Written as expansions around their
 186 equilibria, the two doublets are

$$\phi_a = \begin{pmatrix} \phi_a^+ \\ (v_a + \rho_a + i\eta_a)/\sqrt{2} \end{pmatrix}, \quad a=1, 2.
 \tag{2.23}$$

187 Since we now have two complex scalar doublets, there are total of eight fields. However,
 188 just as in the SM, three of them are replaced by the W^\pm and Z fields, leaving five Higgs
 189 fields. Using Equation 2.23 in 2.21, three separate mass terms in the 2HDM lagrangian are
 190 obtained

$$\begin{aligned}
 \mathcal{L}_{\phi^\pm} = & m_{12}^2 - (\lambda_4 + \lambda_5)v_1v_2 \begin{pmatrix} \phi_1^- & \phi_2^- \end{pmatrix} \begin{pmatrix} \frac{v_2}{v_1} & -1 \\ -1 & \frac{v_1}{v_2} \end{pmatrix} \begin{pmatrix} \phi_1^+ \\ \phi_2^+ \end{pmatrix}, \\
 \mathcal{L}_\eta = & \frac{m_A^2}{v_1^2 + v_2^2} \begin{pmatrix} \eta_1 & \eta_2 \end{pmatrix} \begin{pmatrix} v_2^2 & -v_1v_2 \\ -v_1v_2 & v_1^2 \end{pmatrix} \begin{pmatrix} \eta_1 \\ \eta_2 \end{pmatrix}, \\
 \mathcal{L}_\rho = & - \begin{pmatrix} \rho_1 & \rho_2 \end{pmatrix} \begin{pmatrix} m_{12}^2 \frac{v_2}{v_1} + \lambda_1 v_1^2 & -m_{12}^2 + \lambda_{345} v_1 v_2 \\ -m_{12}^2 + \lambda_{345} v_1 v_2 & m_{12}^2 \frac{v_1}{v_2} + \lambda_2 v_2^2 \end{pmatrix} \begin{pmatrix} \rho_1 \\ \rho_2 \end{pmatrix},
 \end{aligned}
 \tag{2.24}$$

191 where $\lambda_{345} = \lambda_3 + \lambda_4 + \lambda_5$. The mass matrices for the charged (ϕ^\pm) and pseudoscalars $\eta_{1,2}$ can
 192 be diagonalized by the same angle $\beta \equiv \arctan v_2/v_1$, while the mass matrix for the scalars is
 193 diagonalized by the angle α . Together, α and β will affect the couplings of the Higgs bosons
 194 to vector bosons, fermions and each other, and are thus of paramount importance in the

195 phenomenology of a particular 2HDM. The physical fields for the light CP-even h , heavy
 196 CP-even H and heavy CP-odd A can be written as

$$\begin{aligned}
 h &= \rho_1 \sin \alpha - \rho_2 \cos \alpha, \\
 H &= -\rho_1 \cos \alpha - \rho_2 \sin \alpha, \\
 A &= \eta_1 \sin \beta - \eta_2 \cos \beta,
 \end{aligned}
 \tag{2.25}$$

197 The discrete symmetries of the 2HDM lagrangian in Equation 2.21 cause the fermions
 198 to couple to the Higgs doublets in specific ways and the different 2HDMs are categorized
 199 accordingly. In type-I 2HDMs, all charged fermions couple only to ϕ_2 . In type-II 2HDMs,
 200 *up*-type quarks couple to ϕ_2 , while *down*-type quarks and charged leptons couple to ϕ_1 . The
 201 couplings of *up* and *down*-type quarks and leptons is summarized in Table 2.1.

202 **2.3 The MSSM**

203 As mentioned before, an important motivation for 2HDMs is the possibility of accounting for
 204 naturalness through supersymmetry (SUSY). Supersymmetry states that the SM particles
 205 will have supersymmetric partners (spartners) with same quantum numbers, but with spin
 206 that is offset by one half. Particles and their spartners are contained in supermultiplets,
 207 made up of a chiral scalar field and a fermionic field. Due to their chirality, two Higgs
 208 doublets are required in order for the scalars to couple together in the lagrangian and give
 209 the fermions mass. This is also a requirement to avoid introducing chiral anomalies into the
 210 theory.

211 When the symmetry is exact, supersymmetric particles have the same mass as their SM
 212 counterparts and all terms in the SUSY lagrangian have predetermined couplings such that
 213 the theory has no new adjustable parameter. However, this obviously cannot be the case
 214 since new particles with masses equal to their SM partners would have been discovered by
 215 now. Thus, there must be a mechanism that breaks the symmetry and pushes the SUSY
 216 scale to higher energies, but not so high as to make it yet another unnatural theory. There
 217 is currently no completely satisfactory way on how to break SUSY, so a simpler approach

	type-I	type-II
y_h^u	$\cos \alpha / \sin \beta$	$\cos \alpha / \sin \beta$
y_h^d	$\cos \alpha / \sin \beta$	$-\sin \alpha / \cos \beta$
y_h^ℓ	$\cos \alpha / \sin \beta$	$-\sin \alpha / \cos \beta$
y_h^{VV}	$\sin(\beta - \alpha)$	$\sin(\beta - \alpha)$
y_H^u	$\sin \alpha / \sin \beta$	$\sin \alpha / \sin \beta$
y_H^d	$\sin \alpha / \sin \beta$	$\cos \alpha / \cos \beta$
y_H^ℓ	$\sin \alpha / \sin \beta$	$\cos \alpha / \cos \beta$
y_H^{VV}	$\cos(\alpha - \beta)$	$\cos(\alpha - \beta)$
y_A^u	$\cot \beta$	$\cot \beta$
y_A^d	$-\cot \beta$	$\tan \beta$
y_A^ℓ	$-\cot \beta$	$\tan \beta$
y_A^{VV}	0	0

Table 2.1: Yukawa couplings of leptons, vector bosons and *up* and *down*-type quarks to the neutral Higgs bosons h , H and A for 2HDMs of type-I and type-II.

218 is to explicitly add SUSY-breaking parameters to the lagrangian which, together with a few
 219 other well-motivated assumptions, lead to a minimal realization of SUSY called the Minimal
 220 Supersymmetric Standard Model (MSSM) [18].

221 The MSSM is a particular case of type-II 2HDM. It has the same gauge symmetry as the
 222 SM, i.e. $SU(3)_C \times SU(2)_L \times U(1)_Y$. Fermionic superpartners are identified by the letter “s” in
 223 front of their names, e.g. *stop*, *stau*, etc., and boson superpartners are identified by appending
 224 “ino” to their names. Thus, the gauge bosons superpartners are the bino, the three winos,
 225 the eight gluinos and the five higgsinos. The higgsinos and the electroweak partners mix,
 226 giving physical mass eigenstates in the two charginos ($\chi_{1,2}^\pm$) and four neutralinos ($\chi_{1,2,3,4}^0$).
 227 To ensure lepton and baryon number conservation in the MSSM, a symmetry is introduced
 228 that requires R -parity to be conserved. The R -parity quantum number is defined as

$$R_P = (-1)^{2S+3B+L}, \quad (2.26)$$

229 where S , B and L are the spin, baryon and lepton quantum numbers, respectively. Due to
 230 R -parity conservation, the lightest neutralino will be stable, making it an ideal Dark Matter
 231 candidate.

232 The Higgs sector of the MSSM is very well studied, particularly in the context of the LHC
 233 [22, 23]. Because of the necessary introduction of terms that break SUSY into the theory, the
 234 general formulation of the MSSM has 105 unknown free parameters, in addition to the SM
 235 parameters. However, they can be reduced to just 22 by imposing well motivated constraints,
 236 such as requiring no FCNCs at leading order, and that the SUSY-breaking parameters of
 237 the theory do not introduce new sources of CP-violation. This 22-parameter set formulation
 238 of the MSSM is called the “phenomenological MSSM” (pMSSM) [24], and a description of
 239 its parameters is below:

- 240 • $\tan(\beta)$: which is the ratio of the two Higgs doublet vev’s;
- 241 • m_{H_1} and m_{H_2} : the Higgs mass parameters;
- 242 • M_1, M_2, M_3 : the bino, wino and gluino mass parameters;

- 243 • $m_{\tilde{q}}, m_{\tilde{u}_R}, m_{\tilde{d}_R}, m_{\tilde{l}}, m_{\tilde{e}_R}$: the mass parameters for the first two generations of squarks
244 and sleptons;
- 245 • A_u, A_d, A_e : the trilinear couplings of the first two generations of squarks and sleptons;
- 246 • $m_{\tilde{Q}}, m_{\tilde{t}_R}, m_{\tilde{b}_R}, m_{\tilde{L}}, m_{\tilde{\tau}_R}$: the mass parameters of the third generation;
- 247 • A_t, A_b, A_τ : the trilinear couplings of the third generation;

248 It is also interesting to define two parameters that can be written in terms of the above:
249 the stop mixing parameter $X_t \equiv A_t - \mu \cot \beta$, which gives the amount of mixing between
250 left and right-handed stops when computing the stop mass eigenstates, and the SUSY scale
251 $M_S \equiv \sqrt{m_{\tilde{t}_1, \tilde{t}_2}}$ that represents the scale where supersymmetry breaks, usually taken to be
252 around 1 TeV to avoid imposing excessive fine-tuning into the model. The higgsino mass
253 parameter μ is often used when discussing the MSSM Higgs sector, but it is not a free
254 parameter and has its value fixed during electroweak symmetry breaking. It is worth noting
255 that the discovery of the 125 GeV Higgs is still compatible with a large region of the pMSSM
256 parameter space, as shown in Figure 2.4.

257 Though the number of parameters of the pMSSM is much smaller than that of the general
258 formulation of the MSSM, it is still large enough to make interpreting results in the full range
259 of the parameter space cumbersome. Furthermore, at tree-level the MSSM only depends on
260 two parameters, usually taken to be the mass of the CP-odd Higgs boson (m_A) and $\tan \beta$.
261 For example, the masses of the charged and CP-even Higgs bosons (at tree-level) are

$$\begin{aligned}
 m_{H^\pm} &= m_A^2 + m_W^2, \\
 m_{h,H}^2 &= \frac{1}{2} \left[m_A^2 + m_Z^2 \mp \sqrt{(m_A^2 + m_Z^2)^2 - 4m_A^2 m_Z^2 \cos^2 2\beta} \right],
 \end{aligned}
 \tag{2.27}$$

262 as shown in Figure 2.5. It is therefore convenient to test results against signal hypotheses
263 that are scanned in these leading order terms, while fixing the remaining parameters. This
264 approach leads to the definition of several benchmark scenarios [25].

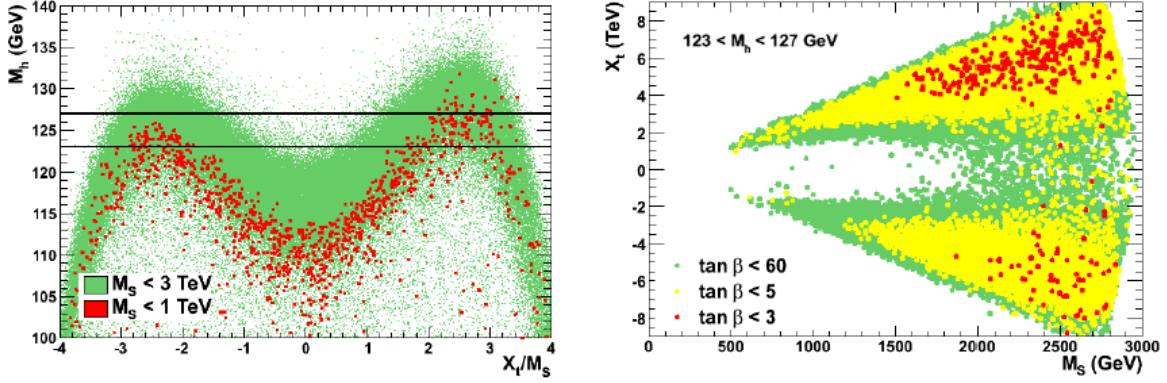


Figure 2.4: The right plot shows the allowed region of the $[X_t, M_S]$ plane of the pMSSM for a range of $\tan \beta$ values, where M_S is the SUSY scale and X_t is the stop mixing parameter. The condition of $X_t/M_S \lesssim 3$ is imposed to avoid a non-viable spectrum of the model. The left plots shows the maximal values of m_h for different X_t/M_S values. Plots from Reference [23].

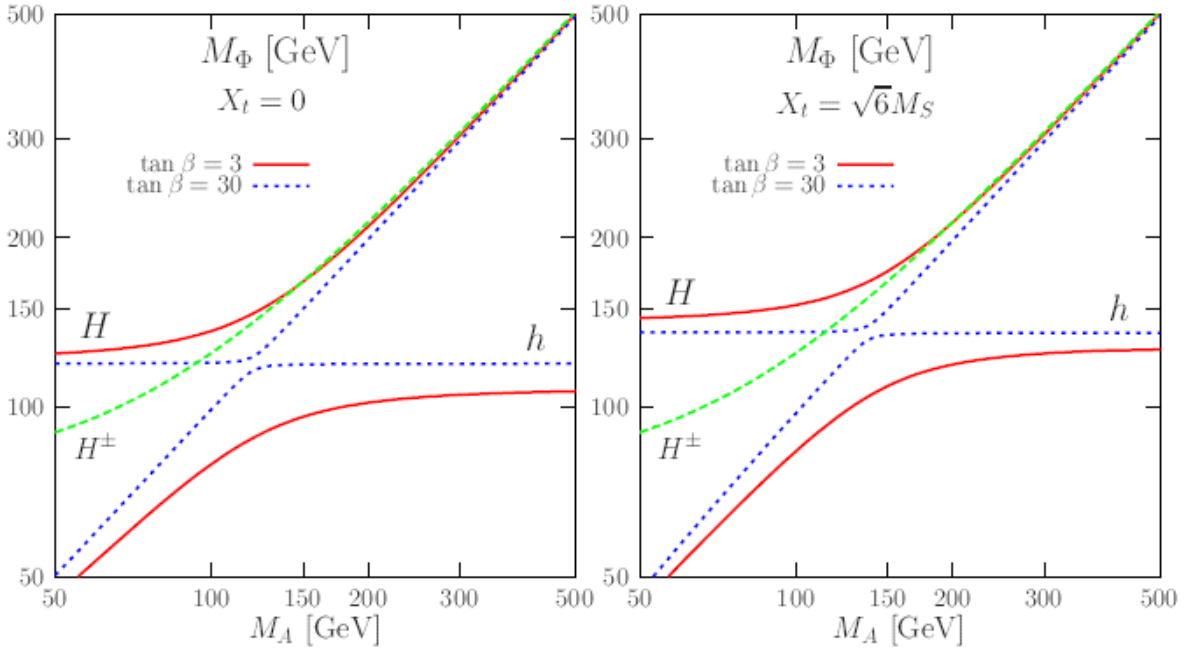
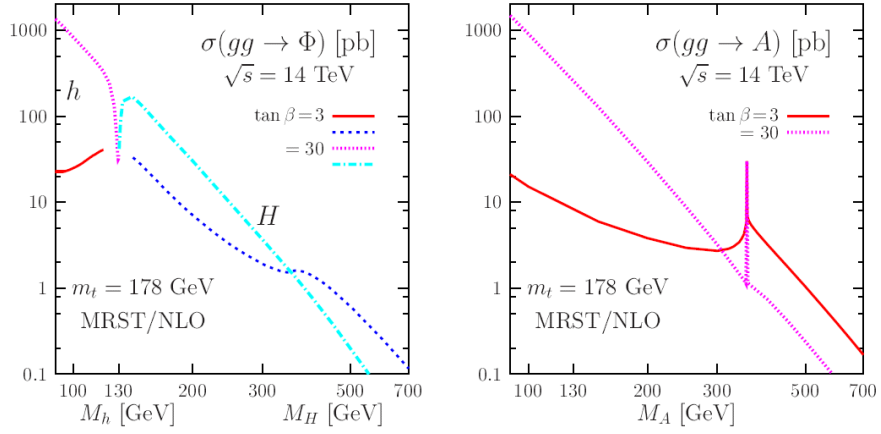


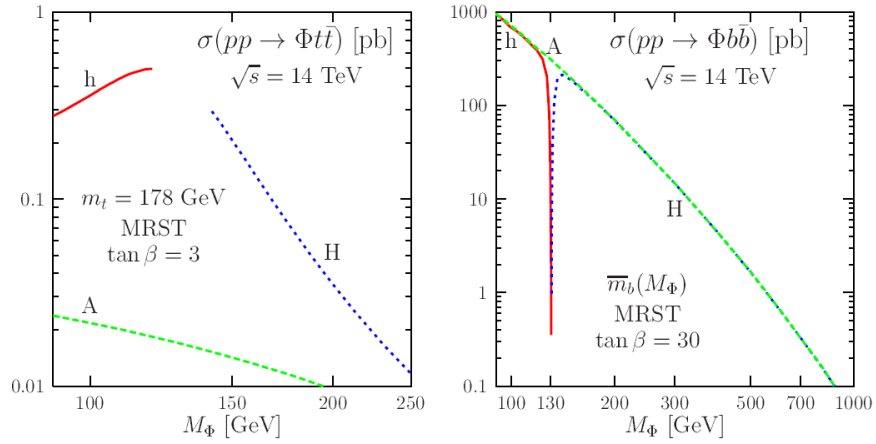
Figure 2.5: Masses of the h , H and H^\pm as a function of the mass of the CP-odd A for stop mixing values $X_t = 0$ (left) and $X_t = \sqrt{6}M_S$ (right). Plots from Reference [22].

265 One such scenario is the m_h^{max} , where the stop mixing parameter X_t is chosen such as to
 266 maximize the mass of the lightest Higgs h , yielding $m_h \sim 135$ GeV for high values of $\tan\beta$
 267 and $M_S \sim 2$ TeV. Though the predicted values of m_h are incompatible with the observation
 268 of the 125 GeV h for the majority of the parameter space, the m_h^{max} scenario nevertheless has
 269 been extensively studied in the past and remains a reference MSSM benchmark. Another
 270 interesting scenario is the m_h^{mod} , which is a modification of the m_h^{max} scenario that gives a
 271 lighter Higgs mass prediction consistent with the observed value at the LHC, while main-
 272 taining a large region of the tree-level parameter space available. The lower m_h prediction
 273 is achieved by reducing the radiative corrections to the Higgs mass from the mixing in the
 274 stop sector. The specific term whose reduction gives the correct m_h prediction is X_t/M_S ,
 275 which can be positive or negative, thus giving two benchmarks called m_h^{mod+} and m_h^{mod-} .

276 Since the MSSM is a type-II 2HDM, its Higgs sector couplings have already been listed in
 277 Table 2.1. Production cross sections for gluon fusion and b -associated production of CP-even
 278 (h, H) and CP-odd (A) Higgs bosons at 14 TeV are shown in Figure 2.6. The MSSM search
 279 presented in this thesis uses data collected at 13 TeV, and production cross sections for that
 280 center of mass energy can be found in Reference [26]. Branching ratios for neutral MSSM
 281 Higgs bosons are shown in Figure 2.7.



(a)



(b)

Figure 2.6: Production cross sections of neutral Higgs bosons from gluon fusion (a) and b -associated production (b) at 14 TeV. Plots from Reference [22].

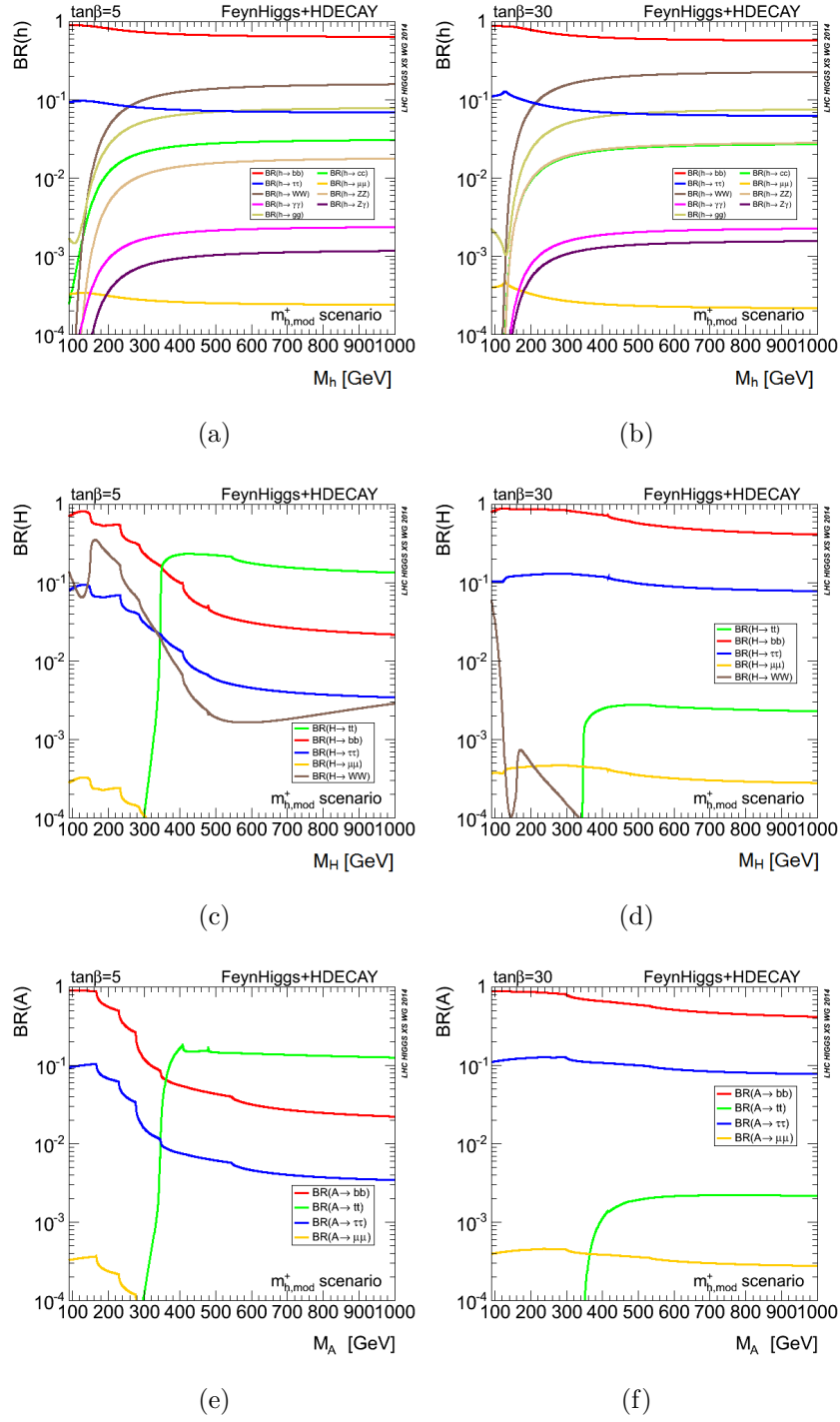


Figure 2.7: Branching ratios of the h , H and A Higgs bosons for $\tan\beta$ values of 5 (left) and 30 (right) in the m_h^{mod+} scenario. Plots from Reference [27].

Chapter 3

APPARATUS

3.1 Overview

The Large Hadron Collider (LHC) is the world's most powerful proton-proton collider [28]. Located at the European Organization for Nuclear Research (CERN) in the outskirts of Geneva, Switzerland, the LHC tunnel is 27 km in circumference and 50 to 175 meters underground. Though the initial design intended for the collision of two 7 GeV proton beams, the current maximum beam energy achieved has been 6.5 GeV. The beams collide at 4 different points in the accelerator ring where the ATLAS, CMS, Alice and LHCb experiments are housed.

3.2 The Accelerator Complex

The LHC beam injection chain is provided by Linac (abbreviation for linear accelerator), Proton Synchrotron Booster (PSB), Proton Synchrotron (PS) and finally Super Proton Synchrotron (SPS). At each accelerator step the beam increases in energy: 50 MeV is achieved during the Linac2 stage, 1.4 GeV at PSB, 25 GeV at PS and finally 450 GeV in the SPS. A schematic overview of the injection chains shown in Figure 3.1. is shown in Figure 3.1.

3.3 LHC

The LHC is divided into 8 alternated straight and arched sectors. The ATLAS experiment is located in the straight section of sector 1, called Point 1, while the CMS experiment is diammetrically opposite in Point 5. Beam injection is done in Points 2 and 8, which also house the ALICE and LHCb experiments, respectively. Points 3 and 7 contain beam collimators, while Point 4 holds two independent Radio Frequency (RF) systems that accelerate each

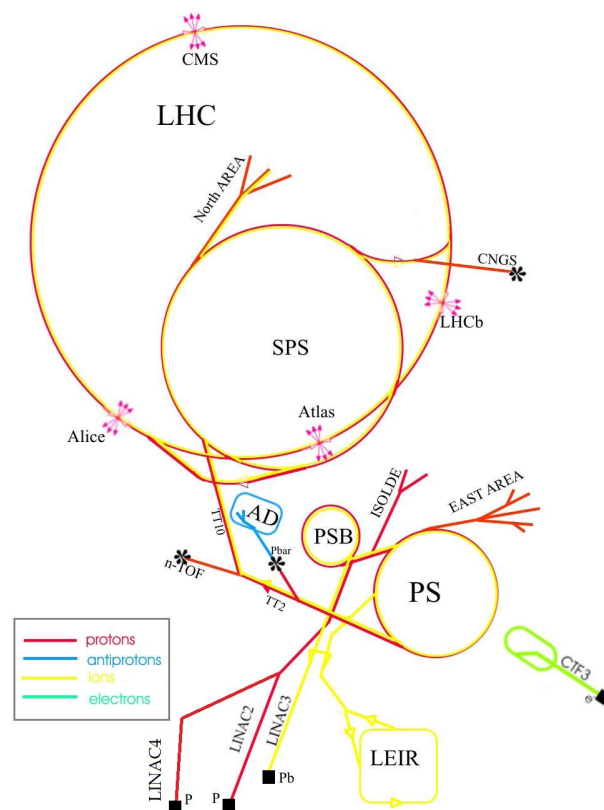


Figure 3.1: A schematic overview of the CERN accelerator complex.

304 beam. Finally, Point 6 holds the beam dump system, a collection of magnets used to deflect
 305 the beam horizontally and vertically out of the LHC ring.

306 The number of events per second dN/dt of a given process is given by

$$\frac{dN}{dt} = \mathcal{L}_{inst}\sigma, \quad (3.1)$$

307 where \mathcal{L}_{inst} is the instantaneous luminosity and σ is the cross section of the physical process.
 308 The total number of events N is given by integrating the above expression in time. For
 309 stable colliding conditions, σ is time-independent such that N is directly proportional to the
 310 time-integrated luminosity L . Thus, we have that the number of events of a process $pp \rightarrow X$
 311 is given by

$$N_X = L\sigma_{pp \rightarrow X}. \quad (3.2)$$

312 The cross section depends on the colliding and produced particles as well as the center-
 313 of-mass energy. The instantaneous luminosity depends only on the beam parameters and is
 314 given by

$$\mathcal{L}_{inst} = \frac{N_b^2 n_b f_{rev} \gamma_r}{4\pi \epsilon_n \beta_*} F \quad (3.3)$$

315 where the terms in the equation above are:

- 316 • the number of bunches in a beam, n_b .
- 317 • the number of protons in a bunch, N_b .
- 318 • the beam revolution frequency, f_{rev} .
- 319 • the relativistic factor, γ_r .
- 320 • the normalized beam emittance (a measure of the beam loss in the transverse plane),
 321 ϵ_n .
- 322 • the beta function at the interaction point, β_* .

323 • the geometrical reduction factor F , due to the beams approaching each other at a slight
 324 angle.

325 As of June 2016, the peak luminosity achieved at the LHC was of $7.9e^{33} \text{ cm}^{-2} \text{ s}^{-1}$, with as
 326 many as 1038 proton bunches per beam.

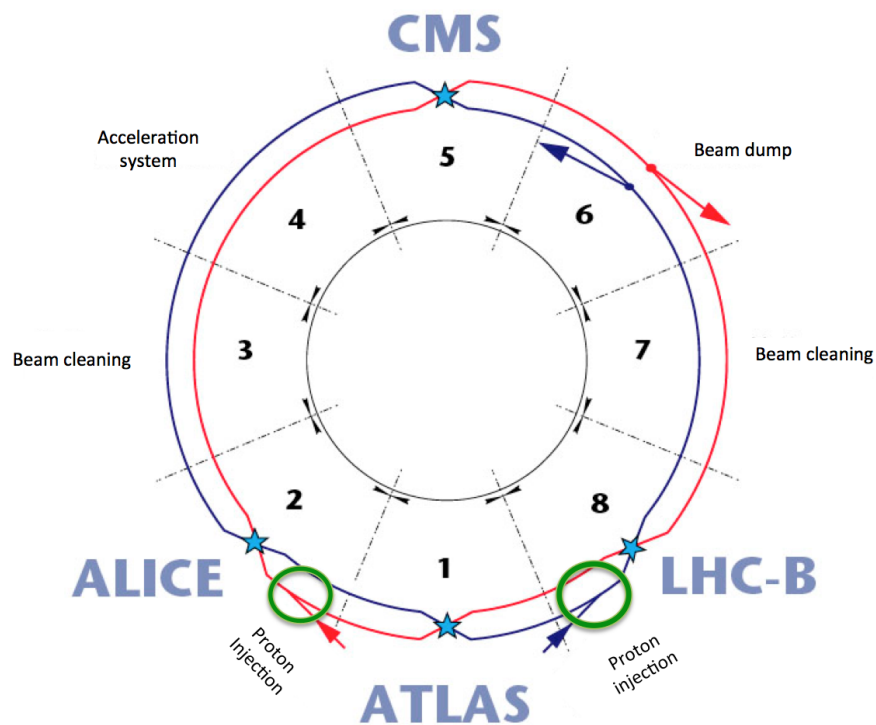


Figure 3.2: The eight sectors of LHC tunnel with the physics experiments depicted.

327 **3.4 ATLAS**

328 The ATLAS detector is a versatile particle detector whose layout is typically broken down into
 329 3 subdetector systems: the Inner Detector (ID), the calorimeter and the Muon Spectrometer
 330 [29]. An overview of the ATLAS detector is shown in Figure 3.3. To facilitate the detector
 331 description and the physical discussion involved, a coordinate system is defined with its origin
 332 at the center of the detector where collisions are expected. The z-axis is defined to be along
 333 the beam, while the xy plane is vertical with respect to the laboratory frame. Directions in
 334 the xy plane are fully determined by the azimuthal angle ϕ , while the polar angle θ is the
 335 angle measured from the beam axis. The latter is often replaced by the pseudorapidity

$$\eta \equiv -\ln(\tan(\theta/2)), \quad (3.4)$$

336 which is an approximation of the rapidity y that is well suited for the high particle energies
 337 present at the LHC. The angular distance between two particles is then

$$\Delta R = \sqrt{\Delta\eta^2 + \Delta\phi^2} \quad (3.5)$$

338 The detector was designed with the aim of searching for the wide range of phenomena
 339 available at the TeV scale. These include not only the (now confirmed) production of the
 340 Standard Model Higgs boson, but also tests of QCD, electroweak, flavour physics and BSM
 341 processes. As such, several minimal benchmarks must be satisfied by ATLAS:

- 342 • Fine granularity to discern between overlapping events.
- 343 • Good track and charge reconstruction.
- 344 • Sufficient vertex reconstruction and resolution to allow for proper identification of
 345 secondary decays, such as those found in b -jets and τ -leptons.
- 346 • Good muon identification and momentum reconstruction.

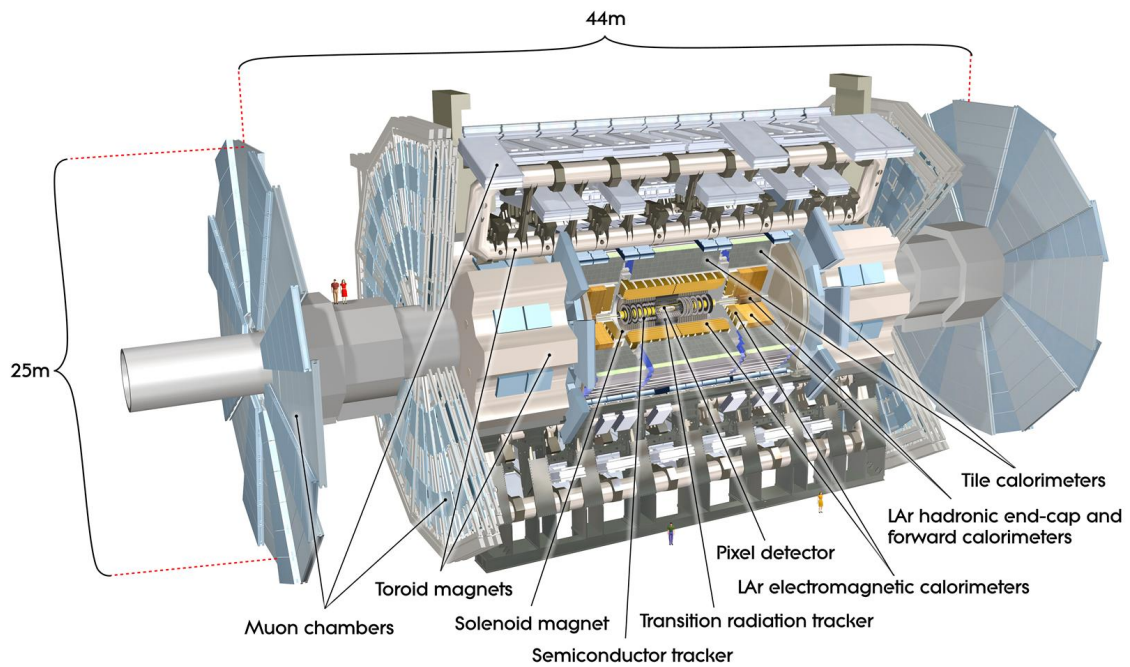


Figure 3.3: The ATLAS detector and its subsystems.

- 347 • Full azimuthal coverage for maximum efficiency, and highest possible pseudorapidity
348 acceptance.
- 349 • Fast and efficiency triggering that can cope with the high event rates while rejecting
350 as much background as possible.

351 3.4.1 The Inner Detector

352 The Inner Detector (ID) is the innermost detector subsystem in ATLAS. It is 6.2 m in
353 length and 2.1 m in diameter, immersed in a 2 T magnetic field from the surrounding central
354 solenoid. The ID is in fact composed of four subdetectors (from nearest to furthest from the
355 beam pipe): the insertable B-layer (IBL), the Pixel detector, the silicon microstrip tracker
356 (SCT) and the transition radiation tracker (TRT). A schematic overview of the ID is shown
357 in Figure 3.4.

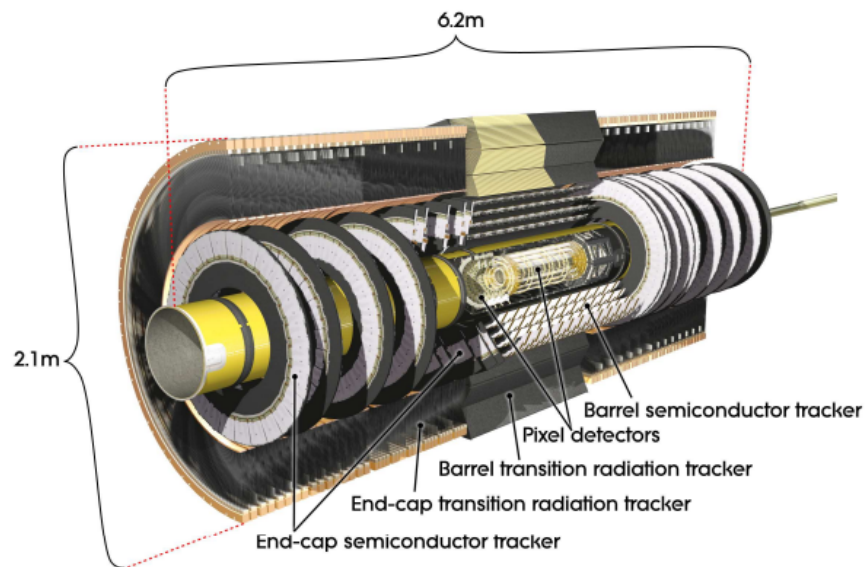


Figure 3.4: Overview of the ATLAS Inner Detector.

358 The IBL was installed during the planned Long Shutdown 1 (LS1) that occurred between
359 Run-1 and Run-2, in 2013-14. This extra detector layer is necessary because the Pixel

360 detector was originally designed for a peak luminosity of $\mathcal{L} = 1 \times 10^{34} \text{cm}^{-2} \text{s}^{-1}$, while the
 361 expected peak luminosity after Run-1 will be closer to $\mathcal{L} = 2 - 3 \times 10^{34} \text{cm}^{-2} \text{s}^{-1}$. Without
 362 the IBL, the inevitable degradation of the Pixel detector would cause ATLAS to longer be
 363 able to meet the tracking and vertexing benchmarks needed for its physics program. The
 364 IBL consists of 14 staves arranged around the beam axis. The staves are flat and arranged
 365 at a 14° tilt with respect to the beam pipe circumference, as seen in Figure 3.5. Each staffe
 366 consists of 20 sensor modules distributed over 64 cm of length and spanning an η range of
 367 2.9. The pixel size in the IBL chipsets is $50 \times 250 \mu\text{m}^2$.

368 Immediately after the IBL is the Pixel detector, which is composed of 3 concentric
 369 cylindrical barrels with 3 disks at each end cap. The number of layers and their arrangement
 370 predicts that each track should have 3 pixel hits. The Pixel has a resolution of $10 \mu\text{m}$ in
 371 $R - \phi$, $115 \mu\text{m}$ in z for the barrel region, and $115 \mu\text{m}$ in R for the end-caps.

372 Surrounding the Pixel is the SCT, composed of 4 coaxial cylindrical layers in the barrel
 373 and 9 disks at each end-cap. Each cylindrical layer has 2 strip layers, one parallel to the
 374 beam axis and another that is offset by 40 mrad. This geometrical arrangement allows for
 375 a 2-dimensional coordinate measurement at each cylinder. A similar setup is found in the
 376 end-cap where one strip is radially aligned while the other is offset again by 40 mrad. The
 377 SCT is accurate to $17 \mu\text{m}$ in the xy plane, $580 \mu\text{m}$ along the z -axis and $580 \mu\text{m}$ in R at the
 378 end-caps.

379 The TRT is the outermost subdetector in the ID. Its 4 mm diameter straw tubes are 144
 380 cm long and arranged parallel to the beam axis over 73 layers in the barrel, and 37 cm long
 381 over 160 straw planes in the end-caps. The TRT straws have an accuracy of $130 \mu\text{m}$ per
 382 straw, but can only make measurements in the xy plane. Though the resolution is lower than
 383 the SCT and Pixel, the TRT is able to make more measurements per track over a longer
 384 length which significantly improves the track momentum measurement.

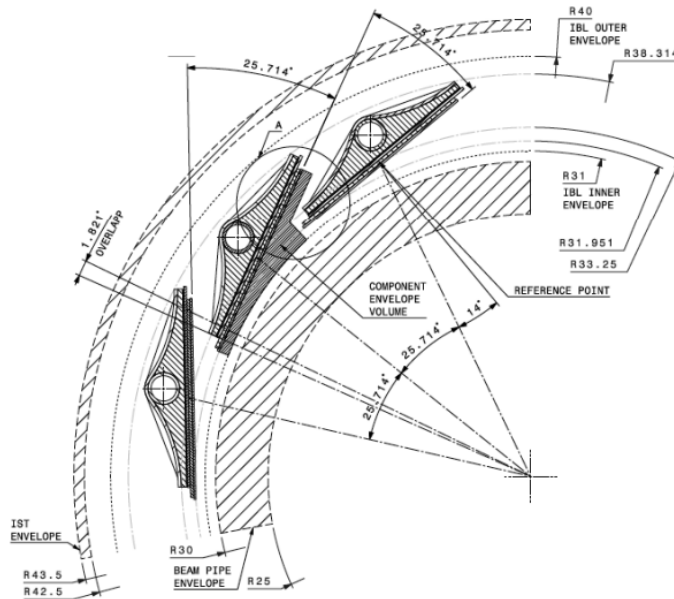


Figure 1. IBL structure in $r-\phi$ plane.

Figure 3.5: IBL structure in the xy plane.

385 3.4.2 The Calorimeter

386 The ATLAS calorimeter system covers the range $|\eta| < 4.9$ and consist of an electromag-
 387 netic calorimeter (EM) just outside the ID and a hadronic calorimeter that envelops the
 388 EM calorimeter. The EM calorimeter has fine granularity and is particularly well suited for
 389 electron and photon reconstruction, while the hadronic calorimeter (HCal) has coarser gran-
 390 ularity that nevertheless is sufficient for reconstructing jet showers. The ATLAS calorimeter
 391 system has approximately 10 interaction lengths (λ), which provides excellent containment
 392 for both electromagnetic and hadronic showers. This will ensure a good missing energy
 393 measurement and reduce background in the muon spectrometer to negligible levels.

394 The EM calorimeter is a lead-liquid Argon detector with barrel ($|\eta| < 1.475$) and end-
 395 cap ($1.375 < |\eta| < 3.2$) components. It has an accordion shape in order to provide complete
 396 ϕ coverage without azimuthal discontinuities, and lead absorber plates that are 1.53 mm

397 (1.7-2.2 mm) thick in the barrel (end-cap). The calorimeter can have two or three layers
 398 depending on the η region, as well as a presampler layer for $|\eta| < 1.8$ (see Table 3.1). The
 399 presampler is a 1.1 cm (0.5 cm) thick active LAr layer used to recover the energy lost by
 400 electrons and photons prior to reaching the calorimeter. The EM calorimeter has a total
 401 thickness of over 22 radiation lengths (X_0) in the barrel and at least 24 radiation lengths in
 402 the end-caps, with an energy resolution $\frac{\sigma_E}{E} = 10.1\%/E \oplus 0.7\%$ (see Figure 3.6).

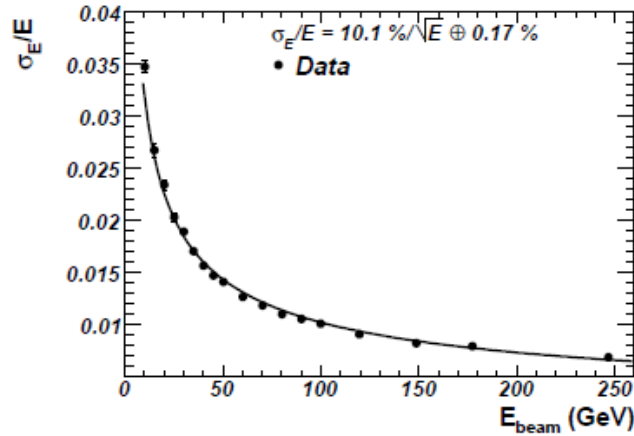


Figure 3.6: Fractional energy resolution of a barrel LAr calorimeter module as a function of beam energy.

403 Similar to the other ATLAS subsystems, the HCal has separate structures for the barrel
 404 and end-caps. The barrel hadronic calorimeter is often called the Tile calorimeter, with a
 405 central barrel for the range $|\eta| < 1.0$ and two extended barrels in the region $0.8 < |\eta| < 1.7$.
 406 It uses scintillating plastic tiles for sampling material and steel as the absorber. Radially,
 407 the tile calorimeter goes from 2.28 m to 4.25 m, and is azimuthally divided in 64 modules.
 408 The barrel is segmented in three layers with interaction lengths of approximately 1.5, 4.1 and
 409 1.8 for a total thickness of 9.7λ at $\eta = 0$. In the end-caps we have the Hadronic End-cap
 410 Calorimeter (HEC). Located directly behind the EM calorimeter, the HEC uses the same LAr
 411 cryostats as the EM calorimeter for the sampling medium. It consists of two independent
 412 coaxial wheels per end-cap, each one built from 32 wedge-like copper plate modules, and

Table 3.1: Parameters of the ATLAS calorimeter.

	Barrel		End-cap	
	Granularity versus $ \eta $			
Presampler	0.025×0.1	$ \eta < 1.52$	0.025×0.1	$1.5 < \eta < 1.8$
Calorimeter 1 st layer	$0.025/8 \times 0.025$	$ \eta < 1.4$	0.050×0.1	$1.375 < \eta < 1.425$
	0.025×0.025	$1.40 < \eta < 1.475$	0.025×0.1	$1.425 < \eta < 1.5$
			$0.025/8 \times 0.1$	$1.5 < \eta < 1.8$
			$0.025/6 \times 0.1$	$1.8 < \eta < 2.0$
			$0.025/4 \times 0.1$	$2.0 < \eta < 2.4$
			0.025×0.1	$2.4 < \eta < 2.5$
Calorimeter 2 nd layer			0.1×0.1	$2.5 < \eta < 3.2$
	0.025×0.025	$ \eta < 1.4$	0.050×0.025	$1.375 < \eta < 1.425$
	0.025×0.025	$1.40 < \eta < 1.475$	0.025×0.025	$1.425 < \eta < 2.5$
Calorimeter 3 rd layer			0.1×0.1	$2.5 < \eta < 3.2$
	0.050×0.025	$ \eta < 1.35$	0.050×0.025	$1.5 < \eta < 2.5$

413 spans the $1.5 < |\eta| < 3.2$ region. The average energy resolution of the HCal is $\frac{\sigma_E}{E} = 50\%/E$

414 Finally, in the end-cap region $3.1 < |\eta| < 4.9$ we have the Forward Calorimeter (FCal),
415 consisting of three modules and 10 interaction lengths of thickness. The first module has
416 copper for the absorption material making it well suited for electromagnetic measurements,
417 while the outer two modules are made of tungsten and serve the role of a hadronic calorimeter.
418 The sensitive medium is again liquid Argon and the energy resolution is $\frac{\sigma_E}{E} = 100\%/E$.

419 3.4.3 The Muon Detector

420 The general layout of the ATLAS Muon Spectrometer (MS) is shown in Figure 3.7. The MS
421 relies on detecting muon tracks passing through its tracking chambers as they are deflected
422 by a strong magnetic field. The field is generated by large air-core superconducting toroid
423 magnets located in the barrel ($|\eta| < 1.4$) and end-caps ($1.6 < |\eta| < 2.7$). The barrel MS
424 is distributed over three cylindrical layers parallel to the beam axis, while the end-caps
425 also have three disk-shaped layers parallel to the xy plane. The precision tracking in the
426 MS is done by Monitored Drift Tubes (MDT's) in the barrel, and Cathode Strip Chambers

427 (CSC's) in the end-caps. The MS also has its own triggering system covering the range
 428 $|\eta| < 2.4$, which is provided by Resistive Plate Chambers (RPC's) in the barrel and Thin
 429 Gap Chambers (TGC's) in the end-caps.

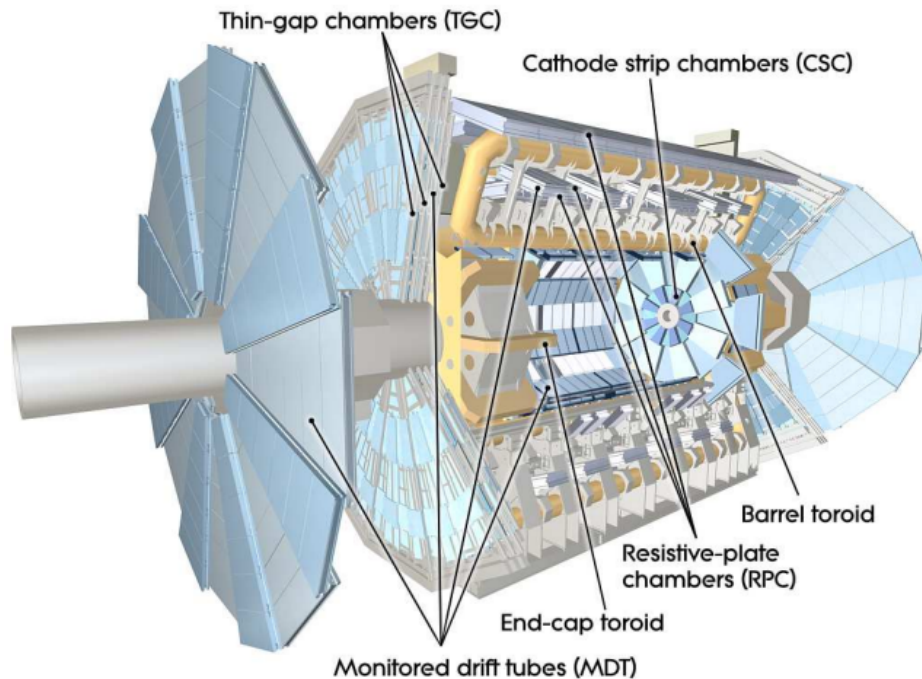


Figure 3.7: Structural layout of the ATLAS muon spectrometer.

430 The MDT's are 30 mm pressurized drift tubes filled with an Ar/CO₂ gas mixture at
 431 a 97/3 ratio and 3 bar. Electrons resulting from gas ionization due to passing muons are
 432 collected in a tungsten-rhenium wire at the center of the tube (Figure 3.8). The MDT's are
 433 assembled inside MDT chambers that are rectangular in the barrel and trapezoidal in the
 434 end-cap, each containing 6-8 tubes. The resolution of a single MDT is approximately 80 μm ,
 435 while a complete MDT chamber has a resolution of 35 μm .

436 It is important to note that the MDT measures the particle's coordinate only in the
 437 bending plane. For a full track measurement in the barrel, the RPC's measurement in the
 438 non-bending plane must be added. The RPC consists of three cylindrical layers, the two

439 innermost chambers select low momentum tracks in the range 6-9 GeV, while the outermost
 440 layer above the MDT selects high momentum particles. Each layer contains two independent
 441 gaseous parallel electrode-plate detectors, thus giving 6 different measurements for a track
 442 that hits all three layers. A coincidence scheme is then used (3-of-4 hits for RPC's 1 and 2,
 443 and 1-of-2 for RPC3) that has high efficiency with strong rejection power of spurious track
 444 signals.

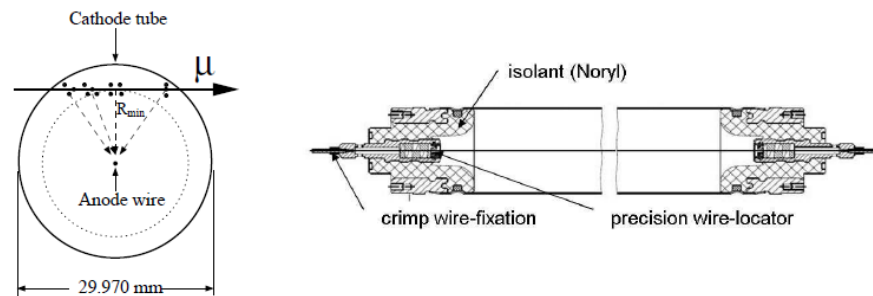


Figure 3.8: Cross-sectional and longitudinal view of a muon drift tube.

445 The CSC's are multiwire proportional chambers with orthogonally aligned cathode seg-
 446 ments. Each end-caps contains two CSC disk systems, each made of eight large and eight
 447 small CSC chambers. The CSC chambers have radially-oriented anode wires and cathode
 448 strips that can be either parallel or perpendicular to the wires (see Figure 3.9). This or-
 449 thogonal orientation allows for both η and ϕ measurements at each of the four CSC planes
 450 in a chamber. The final CSC resolution is $40 \mu\text{m}$ in the bending plane and 5 mm in the
 451 transverse plane.

452 The TGC's provide muon trigger capability in the end-caps as well as a measurement of
 453 the ϕ coordinate to supplement the MDT radial measurement. There are seven TGC layers
 454 accompanying the middle end-cap MDT measurement, and two TGC layers accompanying
 455 the inner MDT layer measurement. The azimuthal coordinate of hits in the outer MDT
 456 layer are obtained through extrapolation from the middle TGC layer, made possible by the
 457 lack of magnetic field between the two outer MDT planes. The TGC's principal of operation

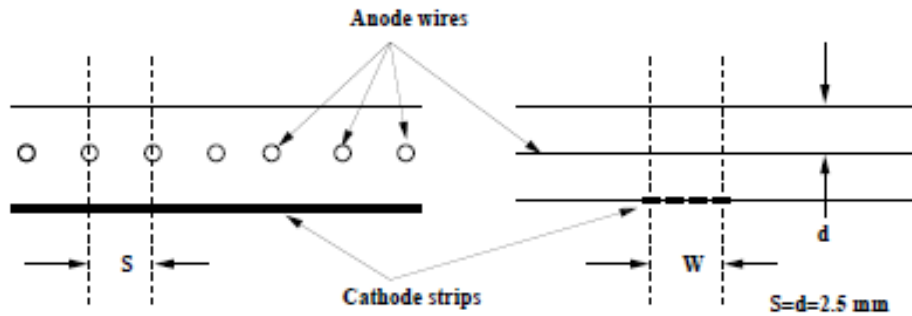


Figure 3.9: Cross-sectional view of a CSC cell.

458 is through a multiwire proportional chamber with two cathode planes and an anode wire
 459 plane kept at 2900 V. The chamber resolution is 2-6 mm in R , 3-7mm in ϕ and 4 ns in time.
 460 A schematic overview of the TGC/MDT layout and the greater ATLAS MS system in the
 461 end-cap region is shown in Figure 3.10.

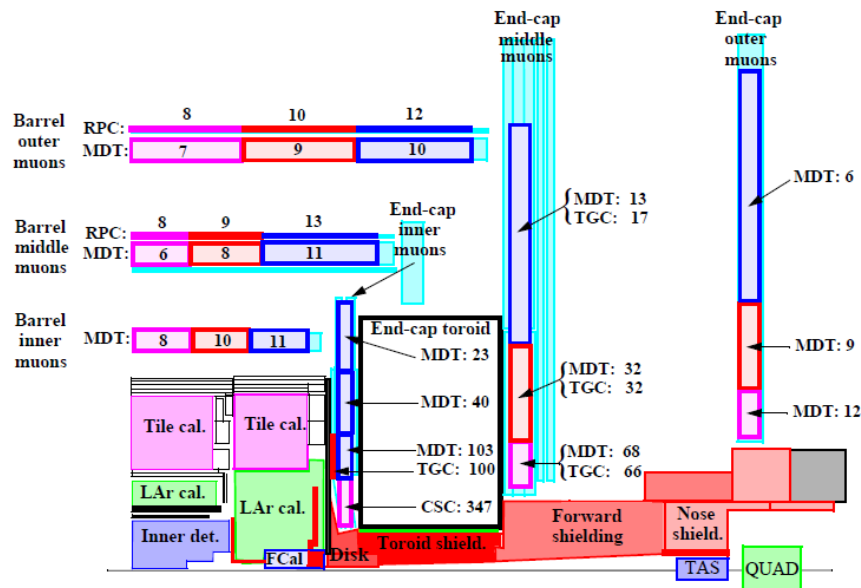


Figure 3.10: Cross-sectional view of the ATLAS muon spectrometer end-cap.

462 3.4.4 *The ATLAS Trigger System*

463 The LHC beam bunches contain upwards of 10^{11} protons colliding 40 million times per
464 second. A typical ATLAS event occupies a few Mb of disk space, so it is not feasible to store
465 every event reconstructed by the ATLAS detector. In addition, many events correspond
466 to well-known processes that are not of interest to the ATLAS physics program. In order
467 to select only events that are potentially interesting and to cope with hardware memory
468 limitations, ATLAS employs a trigger system with three levels: L1, L2 and Event Filter (EF).

469 The L1 trigger chain is the first and lowest trigger level. It searches for events with
470 muons, electrons, τ -leptons, photons and jets with high transverse momentum. Missing
471 energy triggers are also employed. The L1 triggers function by defining Regions-of-Interest
472 (RoI's) where signatures compatible with these objects have been detected, e.g. radial and
473 $\eta - \phi$ coordinates of a high energy cluster in the EM calorimeter.

474 After the event has been flagged as potentially interesting by at least one L1 trigger,
475 the L2 triggers are called. Seeded by the L1 RoI, they use every possible online detector
476 measurement near the RoI to further refine the event selection. The output rate of the L2
477 trigger is approximately 3.5 kHz, and it takes roughly 40 ms to give a binary decision on
478 whether to keep the event. Finally, if the event passes both L1 and L2 triggers, it goes to
479 the EF. This last step is done offline as it has a processing time on the order of 4 seconds,
480 and brings the output rate down to 200 Hz.

481 Chapter 4

482
$$A \rightarrow ZH \rightarrow \ell\ell\tau_{lep}\tau_{had}$$

483 In this chapter we describe the ATLAS search for a heavy CP-odd Higgs boson, A ,
 484 using Run-1 proton-proton collision data at a center-of-mass of 8 TeV and total integrated
 485 luminosity of 20.3 fb^{-1} . The search is done for the $A \rightarrow Zh$ decay mode and m_A range of
 486 $220 - 1000 \text{ GeV}$. The final event signature being searched consists of Z decaying to light
 487 leptons (including intermediate leptonic τ decays), and h decaying to $\tau\tau$, where one tau
 488 decays leptonically (τ_{lep}) and the other decays hadronically (τ_{had}). The $A \rightarrow Zh$ branching
 489 fraction is high for masses below the $t\bar{t}$ production threshold, so this search is particularly
 490 powerful in the $220 < m_A < 350 \text{ GeV}$ region (the lower bound corresponds to the mass
 491 threshold for on-shell decays).

492 **4.1 Samples**

493 *4.1.1 Data Sample*

494 This analysis uses proton-proton collision data recorded by the ATLAS detector during 2012
 495 at a center-of-mass energy of 8 TeV. Only events collected with stable beams and all ATLAS
 496 sub-systems operational are recorded, resulting in 20.3 fb^{-1} with 2.8% uncertainty.

497 *4.1.2 Monte Carlo Simulated Samples*

498 In order to accurately predict the Standard Model background in our signal region, it is
 499 necessary to use simulated events for the various physics processes that can occur in the
 500 proton-proton collisions of the LHC. Monte Carlo simulated samples were generated for
 501 W +jets, Z +jets, $t\bar{t}$, single top, diboson and Z -associated SM Higgs production. The simu-
 502 lation is performed in two steps: the first is the Matrix Element that simulates the parton

503 collision and production, and the second is the simulation of hadronic showering of the quarks
 504 and gluons that were produced.

505 Signal samples for the gluon-fusion production of an A boson decaying to a tau pair are
 506 produced for all three possible tau final states: $A \rightarrow Zh \rightarrow \ell\ell\tau_{lep}\tau_{lep}$, $\ell\ell\tau_{lep}\tau_{had}$, $\ell\ell\tau_{had}\tau_{had}$,
 507 where ℓ can be an electron, muon or tau. Several m_A hypotheses between 220 and 1000 GeV
 508 are considered. The event generation is done with MadGraph5 [30], and the subsequent
 509 parton hadronization is done with Pythia8 [31]. Theoretical cross sections and branching
 510 ratios for 2HDM type-I and II in the SM-like limit ($\sin(\beta - \alpha) \rightarrow 1$) are shown in Tables
 511 4.1 and 4.2. Signal cross sections are computed with SusHi [32], and branching ratios were
 512 obtained using 2HDMC [33]. This limit corresponds to the case where the BSM Higgs bosons
 513 are much heavier than the SM Higgs, such that the lightest Higgs h has SM-like properties
 514 and is said to be *decoupled* from the heavy BSM Higgs sector. The large drop in $A \rightarrow Zh$
 515 branching ratio is due to the decay to $t\bar{t}$ becoming kinematically allowed and, therefore,
 516 dominant.

Table 4.1: Cross sections and branching ratios at different m_A hypotheses for type-I 2HDM.

m_A [GeV]	$\sin(\beta - \alpha)$	$\cos(\beta - \alpha)$	$\sigma(gg \rightarrow A)$ [pb]	$\text{BR}(A \rightarrow Zh)$	$\text{BR}(h \rightarrow \tau\tau)$
Type-I and $\tan(\beta) = 1$					
260	0.999	0.045	6.0135	0.11660	0.06079
340	0.999	0.045	4.4484	0.04540	0.06079
360	0.999	0.045	4.8650	0.00158	0.06079
500	0.999	0.045	1.7543	0.00260	0.06079
1000	0.999	0.045	0.0291	0.01235	0.06079
Type-I and $\tan(\beta) = 10$					
260	0.999	0.045	3.0258	0.92957	0.05978
340	0.999	0.045	2.2424	0.82626	0.05978
360	0.999	0.045	2.4535	0.13629	0.05978
500	0.999	0.045	0.8855	0.20695	0.05978
1000	0.999	0.045	0.0147	0.55573	0.05978

Table 4.2: Cross sections and branching ratios at different m_A hypotheses for type-II 2HDM.

m_A [GeV]	$\sin(\beta - \alpha)$	$\cos(\beta - \alpha)$	$\sigma(gg \rightarrow A)$ [pb]	$\text{BR}(A \rightarrow Zh)$	$\text{BR}(h \rightarrow \tau\tau)$
Type-II and $\tan(\beta) = 1$					
260	0.999	0.045	6.0135	0.11915	0.05714
340	0.999	0.045	4.4484	0.04556	0.05713
360	0.999	0.045	4.8650	0.00158	0.05713
500	0.999	0.045	1.7543	0.00260	0.05713
1000	0.999	0.045	0.0291	0.01235	0.05713
Type-II and $\tan(\beta) = 10$					
260	0.999	0.045	3.0258	0.00363	0.03358
340	0.999	0.045	2.2424	0.01728	0.03358
360	0.999	0.045	2.4535	0.01912	0.03358
500	0.999	0.045	0.8855	0.04951	0.03358
1000	0.999	0.045	0.0147	0.22088	0.03358

517 The event generation for Z +jets processes is done with SHERPA [34]. Top pair and single
518 top production is simulated with POWHEG [35, 36] and AcerMC[37]. Diboson production
519 (ZZ , WZ , WW) is simulated with POWHEG. Triboson (WWW , ZWW , ZZZ) and top-
520 associated Z boson production is done with MadGraph5. We also consider the Z -associated
521 SM Higgs boson production, which is simulated with Pythia8.

522 To simulate the detector response, the events pass through a full simulation of the ATLAS
523 detector done with GEANT4 [38] before being reconstructed with the same ATLAS software
524 used in data events. Due to the high number of bunches during stable beams at the LHC,
525 multiple interactions within the same and nearby bunch crossings can occur. This effect
526 is known as "pileup" and is taken into account by overlaying the simulated samples into
527 minimum-bias events, which are events obtained using a minimal trigger requirement that are
528 a good representation of the background from soft QCD interactions. Finally, a reweighting
529 of average number of interactions per bunch crossing in Monte Carlo (MC) samples is done

530 to match the same distribution in data events.

531 **4.2 Reconstruction**

532 The signal events in this search have electrons, muons and taus in the final state. A good
 533 estimate of the missing transverse energy is necessary for reconstructing the τ -pair mass. In
 534 order to make this object-based selection, it is imperative to have well developed reconstruc-
 535 tion software that translates low-level detector signals, e.g. tracks and calorimeter deposits,
 536 into physical particles.

537 *4.2.1 Electrons*

538 The fundamental requirement for an electron candidate is to have energy deposits in the
 539 EM calorimeter with geometrically compatible charged-particle tracks in the Inner Detector
 540 [39, 40]. Only candidates in pseudorapidity range of $|\eta| < 2.47$ and outside the calorimeter
 541 crack region ($1.37 < |\eta| < 1.52$) are allowed. The crack pseudorapidity region corresponds to
 542 the transition region between the barrel and end-cap calorimeters, and has a higher $e \rightarrow \tau_{had}$
 543 fake rate. All electrons are required to pass “medium” quality identification and have trans-
 544 verse momentum greater than 7 GeV. To reject electrons originating from hadronic decays,
 545 candidates must also be reconstructed with little activity in the surrounding calorimeter area,
 546 i.e. the candidate must be isolated. A lepton is considered isolated if the sum of calorimeter
 547 energy deposits in a cone around the candidate track (and not counting the energy measured
 548 from the track itself) is a small fraction of the lepton transverse momentum. The isolation
 549 criteria for light leptons in this analysis are:

- 550 • $ptcone40/p_T < 0.2$ and $etcone20/p_T < 0.2$ if there are no other leptons within a cone
 551 of $\Delta R = 0.4$.
- 552 • $ptcone20/p_T < 0.2$ and $etcone20/p_T < 0.2$ if there is at least one other lepton within a
 553 cone of $\Delta R = 0.4$.

554 The terms ptcone20 (ptcone40) correspond to the sum of transverse momenta of all tracks
 555 measured in a cone of $\Delta R = 0.2$ (0.4) around the electron track. Analogously, etcone20
 556 is the sum of the measured transverse energy in the calorimeter clusters located in the
 557 $\Delta R = 0.2$ cone surrounding the electron track. The smaller p_T cone used in the case of
 558 overlapping leptons is intended to avoid the neighboring lepton to cause a failure of the
 559 isolation requirement. This is important for higher m_A signal hypotheses where the Z boson
 560 is boosted, causing the leptons from the $Z \rightarrow \ell\ell$ decay to become collimated.

561 4.2.2 Muons

562 Muons candidates are identified by the coincident detection of tracks in the Inner Detector
 563 and the Muon Spectrometer [41]. Muon candidates are considered for pseudorapidities as
 564 high as 2.7 by making use of the tracking provided by the forward muon spectrometer.
 565 Muons are required to have $p_T > 6$ GeV and pass the same isolation requirement as that for
 566 electrons.

567 4.2.3 Jets

568 The term jet refers to the group of collimated particles that are generated from the hadroniza-
 569 tion of energetic gluons and quarks. Jet reconstruction is done through the combination of
 570 calorimeter cell deposits in a process known as clustering. The ATLAS jet reconstruction
 571 is done by first identifying all calorimeter cells with energy deposits at least four times the
 572 background noise. After the initial jet seeds are identified, nearby calorimeter cells with en-
 573 ergy deposits at least twice the noise level are added, along with any cells neighboring them
 574 that have a positive energy measurement. This combination leads to the formation of a 3-
 575 dimensional shower object spread over several calorimeter layers, and is called a topological
 576 cluster, or topo-cluster [42].

577 After the topo-clusters have been determined, the anti- kt algorithm is used to com-
 578 bined them into jets. This is a sequential clustering algorithm that uses the distance
 579 $d_{ti} = \min(1/k_{hard,i}^2, 1/k_{soft,j}^2)\Delta_{ij}^2/R^2$ between energetic (hard) and low-energy (soft) clusters

580 to decide how to do their combination [43]. The cone size parameter used for reconstruction
 581 is $\Delta R = 0.4$. This analysis has no explicit jet selection, but they have an indirect role in our
 582 selection by contributing to the missing transverse energy calculation. Taus can also decay
 583 hadronically with a similar, but narrower, shower cone. Unless explicitly stated otherwise,
 584 this text will use the term jet to refer only to the hadronization showers from quarks and
 585 gluons.

586 4.2.4 *Taus*

587 Hadronically decaying tau candidates are initially seeded from low-level jet objects. If the jet
 588 is sufficiently narrow and has at least one associated track in the inner detector, the object
 589 is considered for hadronic tau reconstruction [44]. All $\tau_{had-vis}$ candidates must have $p_T > 20$
 590 GeV and $|\eta| < 2.47$ (2.5) for 1-track (3-track) τ_{had} . Jets from QCD processes are often
 591 misidentified as hadronic taus, so a multivariate classifier is used to reduce the $jet \rightarrow \tau_{had}$
 592 fake rate. This algorithm is referred to as the τ_{had} -ID, or TauID, and plays a crucial role in
 593 the identification and use of hadronic taus in ATLAS. A detailed description of the TauID
 594 algorithm can be found in Appendix A. A separate BDT-based algorithm is used to reject
 595 $e \rightarrow \tau_{had}$ fakes, called the eVeto. Because of the high efficiency of muon reconstruction, the
 596 fake rate of $\mu \rightarrow \tau_{had}$ can be brought to very small levels by applying a geometric overlap
 597 removal between taus and muons, as described below. Nevertheless, for events where muon
 598 reconstruction fails, rejection is achieved by vetoing tau candidates with large deposits in
 599 the EM calorimeter and low p_T/E_T ratio.

600 4.2.5 *Missing Transverse Energy*

601 Neutrinos are weakly interacting particles that propagate through the ATLAS detector with-
 602 out interacting with its components. Because the total momentum in the xy plane is initially
 603 zero, it is possible to calculate the amount and direction of the missing energy in the trans-
 604 verse plane through momentum conservation. This is called the Missing Transverse Energy,
 605 or E_T^{miss} . The longitudinal missing energy cannot be calculated because the momentum

606 fraction of each colliding parton is unknown. The E_T^{miss} is defined as the opposite of the \vec{p}_T
 607 sum of all reconstructed objects in an event [45], and therefore is often the last step in the
 608 event reconstruction.

609 4.2.6 Object Overlap Removal

610 Often a particle will pass the reconstruction criteria of multiple object types, e.g. an object
 611 reconstructed as both e and τ . Thus, an “Object Overlap Removal” procedure must be
 612 defined to unambiguously reconstruct an event. Object overlap is a geometric consideration
 613 based on whether the angular distance ΔR between the objects is smaller than a certain
 614 threshold. The following priority is used when removing objects:

- 615 • Jets within a $\Delta R = 0.2$ cone of any $\tau_{had-vis}$ or light lepton are excluded.
- 616 • Hadronic taus within a $\Delta R = 0.2$ cone of electrons or muons are excluded, except when
 617 the τ is of at least “loose” identification quality and the overlapping lepton is not. For
 618 the latter case, the light lepton is removed.
- 619 • Electrons within a $\Delta R = 0.2$ cone of muons are excluded, except when the e is of at
 620 least “loose” quality and the μ is not. For the latter case, the μ is excluded.

621 4.2.7 Mass Reconstruction

622 The final discriminant used in this analysis is the reconstructed A boson mass m_A^{rec} . To
 623 obtain m_A^{rec} , one must first reconstruct the mass of the $\tau_{lep}\tau_{had}$ pair. This can be challenging
 624 because tau decays contain neutrinos and, therefore, large E_T^{miss} . To account for this, a
 625 dedicated mass reconstruction algorithm is used, called the Missing Mass Calculator (MMC)

626 [46]. To reconstruct the ditau mass, the MMC must solve the following set of equations:

$$\begin{aligned}
E_{T,x}^{miss} &= p_1^{miss} \sin \theta_1^{miss} \cos \phi_1^{miss} + p_2^{miss} \sin \theta_2^{miss} \cos \phi_2^{miss}, \\
E_{T,y}^{miss} &= p_1^{miss} \sin \theta_1^{miss} \sin \phi_1^{miss} + p_2^{miss} \sin \theta_2^{miss} \sin \phi_2^{miss}, \\
M_{\tau_1}^2 &= (m_1^{miss})^2 + (m_1^{vis})^2 + 2\sqrt{(p_1^{vis})^2 + (m_1^{vis})^2} \sqrt{(p_1^{miss})^2 + (m_1^{miss})^2} - 2p_1^{vis} p_1^{miss} \cos \Delta\theta_{\nu m_1}, \\
M_{\tau_2}^2 &= (m_2^{miss})^2 + (m_2^{vis})^2 + 2\sqrt{(p_2^{vis})^2 + (m_2^{vis})^2} \sqrt{(p_2^{miss})^2 + (m_2^{miss})^2} - 2p_2^{vis} p_2^{miss} \cos \Delta\theta_{\nu m_2},
\end{aligned}
\tag{4.1}$$

627 where $E_{T,x}^{miss}$ and $E_{T,y}^{miss}$ are the components of E_T^{miss} in the transverse plane, $p_{1,2}^{vis}$, $m_{1,2}^{vis}$,
628 $\theta_{1,2}^{vis}$, $\phi_{1,2}^{vis}$ are the (unknown) momenta, invariant masses, polar and azimuthal angles of the
629 visible tau decay products. Variables $p_{1,2}^{miss}$, $m_{1,2}^{miss}$, $\theta_{1,2}^{miss}$, $\phi_{1,2}^{miss}$ are the analogous terms for
630 the invisible products. The tau lepton invariant mass is $M_{\tau_{1,2}} = 1.777 \text{ GeV}/c^2$. The angle
631 between the visible and invisible momentum vectors corresponds to the $\Delta\theta_{\nu m_{1,2}}$ term.

632 For a $\tau_{lep}\tau_{had}$ decay, there are seven unknown variables (due to the constraint that $m_{\tau_{had}}^{miss}$
633 is zero). Since there are only four equation in 4.1, the system is underconstrained. However,
634 not all regions of the unconstrained parameter space are equally likely. This is clear if one
635 looks at ΔR distributions between visible and invisible momenta in simulated hadronic and
636 leptonic tau decays. As Figure 4.1 shows, depending on the tau decay type (1-track, 3-track
637 or leptonic), certain decay topologies are favored and a probability density function can be
638 constructed.

639 The MMC then solves Equations 4.1 by scanning through the kinematically allowed region
640 of the system variables and weighs each solution by its corresponding global decay topology
641 probability, given by:

$$\mathcal{P}_{\text{event}} = \mathcal{P}(\Delta R_1, p_{\tau_1}) \times \mathcal{P}(\Delta R_2, p_{\tau_2}),
\tag{4.2}$$

642 where the probability functions \mathcal{P} depend on the tau decay type and the initial momentum
643 of the parent tau lepton. This scanning procedure will give a distribution of possible values
644 for $m_{\tau\tau}$, and the returned value $m_{\tau\tau}^{MMC}$ estimate is then the maximum of this probability-
645 weighed distribution. For events with leptonic tau decays, the weighing procedure is adjusted

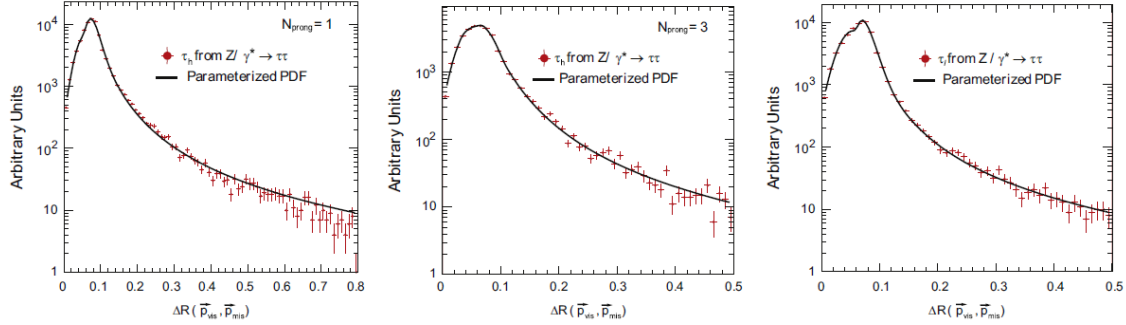


Figure 4.1: Example distributions of the angular distance between visible and invisible momenta of tau decay products for the cases of 1-track (left), 3-track(middle) and leptonic (right) tau decay types. Plots from Reference [46].

646 by incorporating an additional probability, also obtained from simulation, for the invariant
 647 mass of the τ_{lep} neutrinos.

648 Because we know the two pairs in the event must come from a Z and an h boson, we can
 649 achieve a better resolution by subtracting from the 4-object invariant mass the difference of
 650 the reconstructed $\ell\ell$ and $\tau\tau$ pair masses from their known parent particle values:

$$m_A^{rec} = m_{\ell\ell\tau\tau} - (m_{\ell\ell} - m_Z^0) - (m_{\tau\tau}^{MMC} - m_h^0) \quad (4.3)$$

651 The terms in Equation 4.3 are:

- 652 • m_Z^0 is the known mass of the Z boson, 91.2 GeV, and $m_H^0 = 125$ GeV is the mass of
 653 the assumed light Higgs.
- 654 • $m_{\tau\tau}^{MMC}$ is the mass of the tau pair as returned by the MMC.
- 655 • $m_{\ell\ell}$ is the invariant mass of the two light leptons that come from the Z decay.
- 656 • $m_{\ell\ell\tau\tau}$ is the invariant mass of the Z leptons and the two taus, where the latter is
 657 computed with the MMC.

658 **4.3 Event Selection**

659 Events in this search are initially selected by the firing of at least one of the following single-
 660 lepton triggers: `EF_e24vhi_medium1`, `EF_mu24i_tight` or `EF_mu36_tight`. In the case of
 661 the event being triggered only by the high p_T muon trigger, we require the offline transverse
 662 momentum of the highest p_T muon to be greater than 36 GeV. Dilepton triggers were not
 663 included because they did not increase the acceptance significantly.

664 All events must have exactly three light leptons and one hadronic tau. The p_T require-
 665 ments for these objects are:

- 666 • $p_T > 20$ GeV for the hadronic tau.
- 667 • $p_T > 26$ GeV (15 GeV) for the leading (remaining) electron(s).
- 668 • $p_T > 25 - 36$ GeV (10 GeV) for the leading (remaining) muon(s), depending on the
 669 trigger.

670 Since this search has three light leptons in the final state, it is important to distinguish
 671 which come from the $Z \rightarrow \ell\ell$ decay and which is from the leptonic tau decay. If the light
 672 lepton belongs to a pair with opposite sign and same lepton flavor, it is classified as the
 673 former. If more than one such pair is possible, the pair with invariant mass closest to the Z
 674 boson mass (91.2 GeV) is assumed to come from the Z decay. If the invariant mass $m_{\ell\ell}$ of
 675 this lepton pair is outside a Z -mass window of 80 – 100 GeV, the event is discarded. The
 676 following cuts are then applied to complete the $A \rightarrow Zh \rightarrow \ell\ell\tau_{lep}\tau_{had}$ selection:

- 677 • Electrons, muons and the hadronic tau must pass their respective medium-level iden-
 678 tification criteria.
- 679 • The MMC algorithm must succeed in reconstructing the mass of the $\tau_{lep}\tau_{had}$ pair, which
 680 in turn must be in the range $75 < m_{\tau\tau} < 175$ GeV.

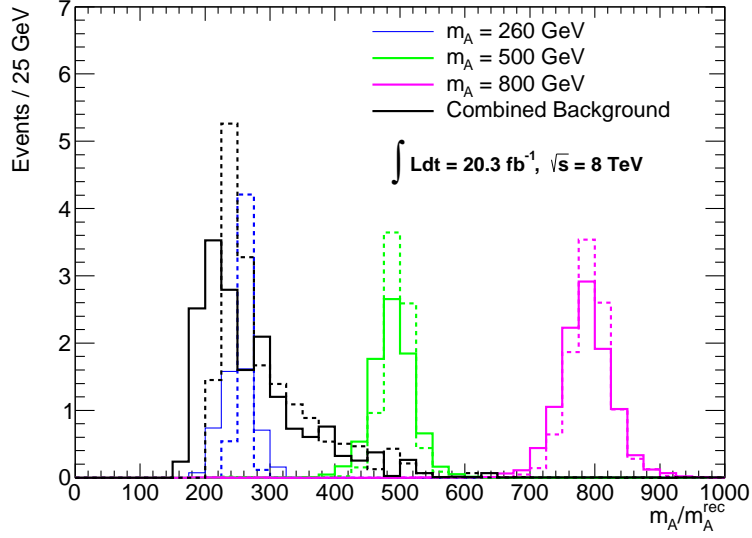


Figure 4.2: A comparison of $m_{\ell\ell\tau\tau}$ (solid) mass and m_A^{rec} (dashed) for 260 GeV, 500 GeV, 800 GeV and combined background. The background prediction shown here is exclusively from simulated events.

681 Figure 4.2 shows distributions for several signal mass hypotheses of $m_{\ell\ell\tau\tau}$ and m_A^{rec} , where
 682 the latter can be seen to have significantly better resolution. Figure 4.3 shows the acceptance
 683 efficiency of the full selection on different signal mass hypotheses.

684 4.4 Background Estimation

685 The most important background processes that can pass our signal region selection are Z +jets,
 686 diboson and a smaller contribution from Z -associated SM Higgs production. In virtually all
 687 simulated events passing our selection the light leptons are found to be matched to a true
 688 lepton. Background events can then be assigned to two different categories:

- 689 • Events with correctly identified τ_{had} , or light leptons misidentified as τ_{had} .
- 690 • Events with QCD jets misidentified as the τ_{had} .

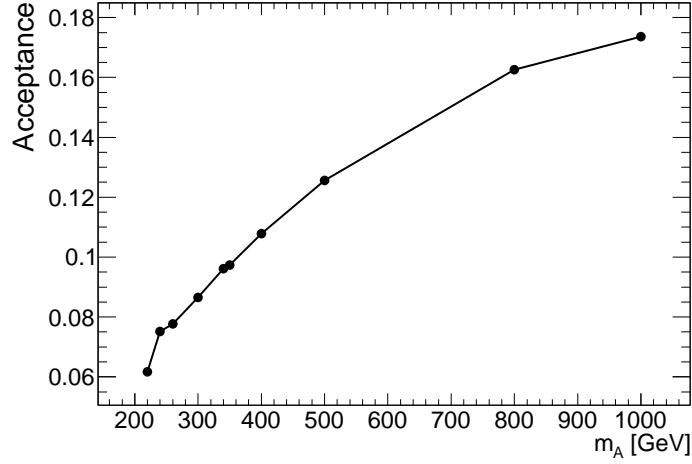


Figure 4.3: The signal acceptance efficiency for the full $\ell\ell\tau_{lep}\tau_{had}$ selection.

691 The background prediction of events in the first category is done entirely through simulated
 692 events, after confirming the reconstructed τ_{had} geometrically overlaps with a truth-level lep-
 693 ton, i.e. that the τ_{had} is truth-matched. However, because the $jet \rightarrow \tau_{had}$ fake rate is not
 694 well modelled in simulation, events in the second category are predicted using a data-driven
 695 template method.

696 The template method consists of obtaining the shape of the background distribution of
 697 the mass discriminant m_A^{rec} , i.e. the "background template", from a control region henceforth
 698 referred to as the template region. The template region has the same selection as the signal
 699 region, except either the Higgs lepton and the τ_{had} have same-charge sign (SS), the τ_{had} fails
 700 medium identification, or both. The normalization of the background template in the signal
 701 region is done using a scale factor measured in the Higgs mass sidebands (h -sidebands), where
 702 $m_{\tau\tau} < 75$ GeV or $m_{\tau\tau} > 175$ GeV. The scale factor is defined as the ratio of opposite-sign
 703 (OS), passing medium τ_{had} ID events in the h -sideband region to the yield of template region
 704 events also in the h -sidebands. Since the objective is to estimate the fake- τ_{had} background,
 705 simulated events where the τ_{had} is truth-matched are subtracted from data at all levels in
 706 this procedure.

Template control region event yields						
Sample	Region B		Region C		Region D	
	truth-matched	other	truth-matched	other	truth-matched	other
	$ll\tau\tau$		$ll\tau\tau$		$ll\tau\tau$	
AZh (260 GeV)	0.0029 ± 0.0008	0.0030 ± 0.0008	0.1130 ± 0.0051	0.0265 ± 0.0023	0.0025 ± 0.0007	0.0247 ± 0.0021
AZh (400 GeV)	0.0038 ± 0.0009	0.0050 ± 0.0010	0.1344 ± 0.0057	0.0303 ± 0.0023	0.0042 ± 0.0010	0.0229 ± 0.0020
SM Higgs Zh	0.00 ± 0.00	0.01 ± 0.00	0.21 ± 0.01	0.02 ± 0.01	0.01 ± 0.00	0.02 ± 0.00
WW	0.00 ± 0.00	0.00 ± 0.00	0.00 ± 0.00	0.00 ± 0.00	0.00 ± 0.00	0.00 ± 0.00
WZ	0.00 ± 0.00	0.75 ± 0.19	0.00 ± 0.00	23.88 ± 1.07	0.00 ± 0.00	16.92 ± 0.89
ZZ	0.03 ± 0.01	0.23 ± 0.02	2.90 ± 0.11	3.09 ± 0.09	0.10 ± 0.02	2.97 ± 0.08
Triboson	0.00 ± 0.00	0.00 ± 0.00	0.01 ± 0.00	0.03 ± 0.01	0.00 ± 0.00	0.02 ± 0.00
Top	0.00 ± 0.00	0.42 ± 0.42	0.00 ± 0.00	0.81 ± 0.64	0.00 ± 0.00	0.88 ± 0.51
Top+Z	0.01 ± 0.01	0.03 ± 0.02	0.02 ± 0.01	0.48 ± 0.07	0.00 ± 0.00	0.27 ± 0.05
Z+Jets	0.00 ± 0.00	1.96 ± 1.21	0.00 ± 0.00	27.39 ± 5.55	0.00 ± 0.00	26.86 ± 5.35
Drell-Yan	0.00 ± 0.00	0.00 ± 0.00	0.00 ± 0.00	0.60 ± 0.30	0.00 ± 0.00	0.15 ± 0.14
Data	9		78		74	

Sample	Total		Signal Region	
	truth-matched	other	truth-matched	other
	$ll\tau\tau$		$ll\tau\tau$	
AZh (260 GeV)	0.118 ± 0.005	0.054 ± 0.003	0.478 ± 0.011	0.009 ± 0.001
AZh (400 GeV)	0.142 ± 0.006	0.058 ± 0.003	0.662 ± 0.012	0.015 ± 0.002
SM Higgs Zh	0.22 ± 0.01	0.05 ± 0.00	0.85 ± 0.02	0.02 ± 0.00
WW	0.00 ± 0.00	0.00 ± 0.00	0.00 ± 0.00	0.00 ± 0.00
WZ	0.00 ± 0.00	41.55 ± 1.40	0.00 ± 0.00	2.15 ± 0.32
ZZ	3.04 ± 0.11	6.29 ± 0.12	6.97 ± 0.17	0.30 ± 0.03
Triboson	0.01 ± 0.00	0.05 ± 0.01	0.08 ± 0.01	0.00 ± 0.00
Top	0.00 ± 0.00	2.11 ± 0.92	0.00 ± 0.00	0.00 ± 0.00
Top+Z	0.02 ± 0.01	0.78 ± 0.09	0.02 ± 0.01	0.07 ± 0.02
Z+Jets	0.00 ± 0.00	56.21 ± 7.80	0.00 ± 0.00	1.10 ± 0.66
Drell-Yan	0.00 ± 0.00	0.75 ± 0.33	0.00 ± 0.00	0.00 ± 0.00
Data	161		18	

Table 4.3: Number of events passing the $\tau_{lep}\tau_{had}$ channel selection in the template control region. For a better overview, the events are also split in regions B ($\tau_{lep}\tau_{had}$ is SS, τ_{had} passes TauID), C ($\tau_{lep}\tau_{had}$ is OS, τ_{had} fails TauID) and D ($\tau_{lep}\tau_{had}$ is SS, τ_{had} fails TauID). The signal region is also shown for comparison. Signal numbers assume $\sigma(gg \rightarrow A) \times BR(A \rightarrow Zh \rightarrow ll\tau\tau) = 1$ fb.

Higgs sidebands control region event yields						
Sample	Region B		Region C		Region D	
	truth-matched	other	truth-matched	other	truth-matched	other
	$ll\tau\tau$		$ll\tau\tau$		$ll\tau\tau$	
AZh (260 GeV)	0.00027 ± 0.00027	0.0006 ± 0.0002	0.0092 ± 0.0015	0.0174 ± 0.0017	0.0000 ± 0.0000	0.0164 ± 0.0017
AZh (400 GeV)	0.00039 ± 0.00027	0.0012 ± 0.0005	0.0079 ± 0.0014	0.0225 ± 0.0021	0.0005 ± 0.0003	0.0239 ± 0.0021
SM Higgs Zh	0.00 ± 0.00	0.00 ± 0.00	0.01 ± 0.00	0.01 ± 0.00	0.00 ± 0.00	0.02 ± 0.00
WW	0.00 ± 0.00	0.00 ± 0.00	0.00 ± 0.00	0.00 ± 0.00	0.00 ± 0.00	0.00 ± 0.00
WZ	0.00 ± 0.00	0.70 ± 0.18	0.00 ± 0.00	18.36 ± 0.93	0.00 ± 0.00	14.28 ± 0.82
ZZ	0.10 ± 0.10	0.19 ± 0.02	0.64 ± 0.32	3.12 ± 0.09	0.00 ± 0.00	3.06 ± 0.08
Triboson	0.00 ± 0.00	0.00 ± 0.00	0.02 ± 0.00	0.02 ± 0.01	0.00 ± 0.00	0.02 ± 0.01
Top	0.00 ± 0.00	0.00 ± 0.00	0.00 ± 0.00	0.96 ± 0.73	0.00 ± 0.00	0.49 ± 0.35
Top+Z	0.00 ± 0.00	0.02 ± 0.02	0.00 ± 0.00	0.38 ± 0.06	0.00 ± 0.00	0.27 ± 0.05
Z+Jets	0.00 ± 0.00	2.86 ± 1.39	0.00 ± 0.00	50.39 ± 7.11	0.00 ± 0.00	58.28 ± 9.55
Drell-Yan	0.00 ± 0.00	0.00 ± 0.00	0.00 ± 0.00	0.47 ± 0.24	0.00 ± 0.00	0.68 ± 0.37
Data	7		102		85	

Sample	Total		Region A	
	truth-matched	other	truth-matched	other
	$ll\tau\tau$		$ll\tau\tau$	
AZh (260 GeV)	0.0095 ± 0.0015	0.0344 ± 0.0024	0.0387 ± 0.0029	0.0010 ± 0.0004
AZh (400 GeV)	0.0088 ± 0.0014	0.0476 ± 0.0030	0.0273 ± 0.0025	0.0025 ± 0.0007
SM Higgs Zh	0.01 ± 0.00	0.03 ± 0.00	0.06 ± 0.01	0.00 ± 0.00
WW	0.00 ± 0.00	0.00 ± 0.00	0.00 ± 0.00	0.00 ± 0.00
WZ	0.00 ± 0.00	33.34 ± 1.25	0.00 ± 0.00	1.88 ± 0.30
ZZ	0.99 ± 0.06	6.37 ± 0.12	2.22 ± 0.09	0.20 ± 0.02
Triboson	0.02 ± 0.00	0.04 ± 0.01	0.12 ± 0.01	0.01 ± 0.00
Top	0.00 ± 0.00	1.45 ± 0.81	0.00 ± 0.00	0.00 ± 0.00
Top+Z	0.00 ± 0.00	0.67 ± 0.08	0.05 ± 0.02	0.03 ± 0.01
Z+Jets	0.00 ± 0.00	111.53 ± 11.99	0.00 ± 0.00	1.02 ± 0.72
Drell-Yan	0.00 ± 0.00	1.15 ± 0.44	0.00 ± 0.00	0.00 ± 0.00
Data	194		14	

Table 4.4: Number of events passing the $\tau_{lep}\tau_{had}$ channel selection in the Higgs sidebands control region. For a better overview, the events are also split in regions B ($\tau_{lep}\tau_{had}$ is SS, τ_{had} passes TauID), C ($\tau_{lep}\tau_{had}$ is OS, τ_{had} fails TauID) and D ($\tau_{lep}\tau_{had}$ is SS, τ_{had} fails TauID). Region A is defined such that all the requirements of the signal region are satisfied apart from the Higgs mass window constrain. Signal numbers assume $\sigma(gg \rightarrow A) \times BR(A \rightarrow Zh \rightarrow ll\tau\tau) = 1$ fb.

707 Effectively, the template region is defined by the separate or simultaneous failure to meet
 708 two selection criteria of the signal region: the τ_{had} medium identification, and the OS charge
 709 requirement of the $\tau_{lep}\tau_{had}$ system. Thus, the template region can be split into three regions
 710 (B, C and D) that have same selection as the signal region (A) except:

- 711 • Region B has $\tau_{lep}\tau_{had}$ being same-sign charge.
- 712 • Region C has the τ_{had} fail medium ID.
- 713 • Region D has $\tau_{lep}\tau_{had}$ being same-sign charge and τ_{had} fails medium ID.

714 Table 4.3 shows event yields across the 4 regions, while Table 4.4 shows the corresponding
 715 numbers in the h -mass sidebands.

716 4.4.1 *Template Method Systematics*

717 There are two potential sources of systematic error in the template method: if the background
 718 shape in the template region models poorly the corresponding shape in the signal region,
 719 and similarly if the normalization factor calculated in the h -sidebands is not an accurate
 720 measure of the same normalizing scale in the h -mass window. To investigate shape-related
 721 systematics, the template control region is altered in various ways and the shape of the
 722 nominal template is compared to that from the alternately defined regions. The alternate
 723 regions used are:

- 724 • R1: only same-sign events are included
- 725 • R2: only opposite-sign events are included
- 726 • R3: The tau passes loose ID
- 727 • R4: Light lepton from Higgs decay passes loose ID
- 728 • R5: Both τ_{had} and Higgs lepton pass loose ID

729 In addition, a Z -sidebands region is defined where the cut on the mass of the Z leptons is
 730 inverted ($m_{\ell\ell} < 80$ GeV or $m_{\ell\ell} > 100$ GeV). The main fake- τ_{had} background is from Z +jets
 731 processes so this control region is less motivated than the h -sidebands region. However,
 732 there are still some Z +jets events that fall outside the Z -mass window cut and therefore
 733 the Z -sidebands control region can be used as a secondary cross-check on both the shape
 734 and normalization factor used in the template method. As shown in Figure 4.4, no strong
 735 systematic difference is observed between the shapes of the m_A^{rec} distributions in region (A)
 736 and template, for methods using either the h -sidebands or Z -sidebands. Therefore, no shape
 737 systematics in the background template is used. As can be seen in Figure 4.5, the back-
 738 ground template in the Z -sidebands has a different shape to that of the h -sidebands and
 739 nominal template regions. This, coupled to the lower event population in the Z -sidebands,
 740 are additional motivations for using the h -sidebands to compute the normalization factor.

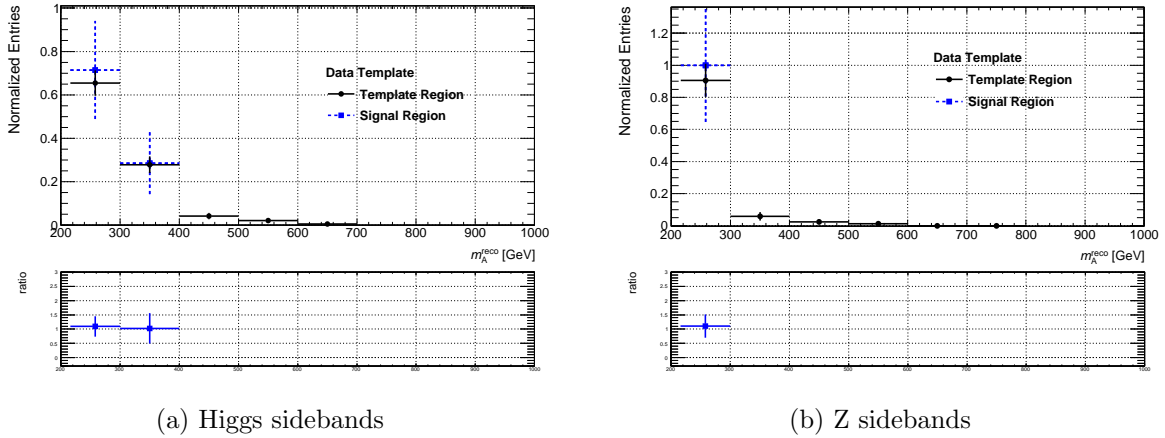


Figure 4.4: The shape of the reconstructed A boson mass, m_A^{rec} , for events passing in the Higgs sidebands region (a) and the Z sidebands region (b) compared to Region A of Z sidebands and Higgs sidebands respectively. The truth-matched $ll\tau\tau$ events have been subtracted in both cases.

741 Regions R1-R5 are also used to estimate systematic uncertainties on the normalization
 742 factor. Table 4.5 contains the normalization factors of each region and their corresponding

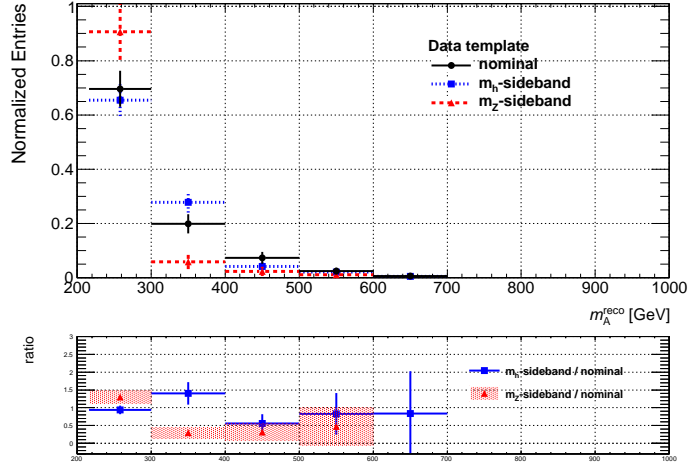


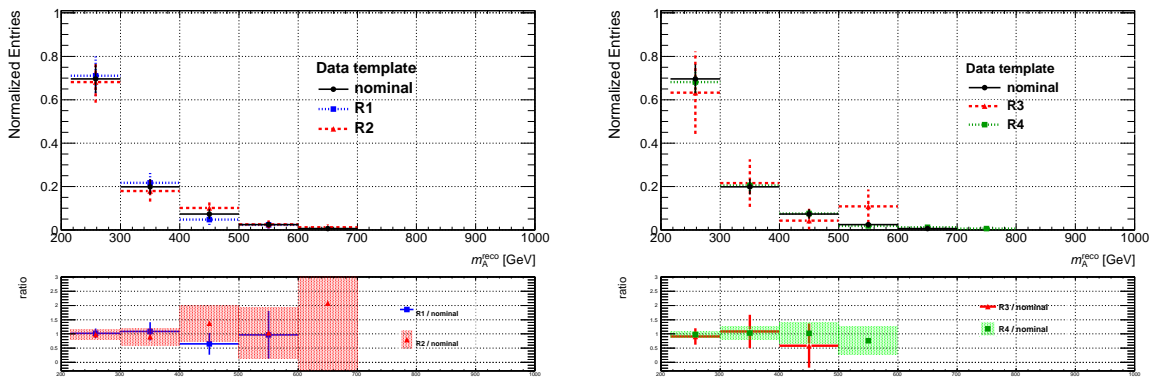
Figure 4.5: The shape of the reconstructed A boson mass, m_A^{rec} , for events passing in the Z sidebands region, the Higgs sidebands region and the template region for the full selection. The truth-matched $ll\tau\tau$ events have been subtracted in both cases.

743 predicted fake- τ_{had} event yields in the signal region. The uncertainty in the normalization
 744 factor is mainly due to the limited number of events in region A of the h -sidebands. This
 745 leads to a large uncertainty in the predicted yield, shown second in the quoted errors of
 746 Table 4.5. The first error quoted corresponds to the statistical variance expected for each
 747 predicted value and depends only on the number of events in the template region.

748 The variations in the normalization factor can be used to estimate a systematic uncer-
 749 tainty. Assuming a gaussian distribution around a central value, the normalization factor
 750 variance corresponds to approximately 1.5 events in the fake- τ_{had} events prediction. The
 751 final prediction of the nominal template method is then:

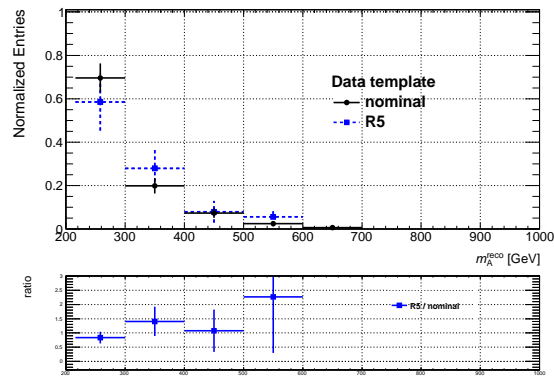
$$N_{fakes} = 9.44 \pm 0.76 \pm 3.13 \pm 1.5 = 9.4 \pm 3.5, \quad (4.4)$$

752 where the errors are, in order of appearance, due to: the statistical uncertainty of the
 753 template, the limited number of events in the h -sidebands used to calculate the normalization
 754 factor, and the variance of the prediction. Thus, the final fake- τ_{had} background prediction
 755 has a 37% uncertainty which is, by a large margin, the largest systematic uncertainty of this



(a) R1 and R2

(b) R3 and R4



(c) R5

Figure 4.6: The default template shape compared to the shape that is obtained if the R1 – R5 control regions are used instead. For more details see in the text.

Sample	Higgs sidebands		Z sidebands	
	Norm. factor	Predicted N_{fakes}	Norm. factor	Predicted N_{fakes}
Nominal	$5.73 \pm 2.01) \times 10^{-2}$	$9.15 \pm 0.73 \pm 3.2$	$(6.50 \pm 3.50) \times 10^{-2}$	$10.39 \pm 0.83 \pm 5.6$
R1	$(1.20 \pm 0.43) \times 10^{-1}$	$9.99 \pm 1.10 \pm 3.6$	$(1.04 \pm 0.57) \times 10^{-1}$	$8.65 \pm 0.95 \pm 4.7$
R2	$(1.09 \pm 0.39) \times 10^{-1}$	$8.38 \pm 0.97 \pm 3.0$	$(1.73 \pm 0.96) \times 10^{-1}$	$13.27 \pm 1.53 \pm 7.4$
R3	$(5.92 \pm 2.46) \times 10^{-1}$	$10.81 \pm 2.59 \pm 4.5$	1.39 ± 1.01	$25.37 \pm 6.07 \pm 18.5$
R4	$(3.39 \pm 1.12) \times 10^{-2}$	$10.68 \pm 0.60 \pm 3.5$	$(2.47 \pm 1.32) \times 10^{-2}$	$7.79 \pm 0.44 \pm 4.1$
R5	$(3.67 \pm 1.30) \times 10^{-1}$	$12.91 \pm 3.21 \pm 4.6$	$(4.74 \pm 2.19) \times 10^{-1}$	$16.64 \pm 2.85 \pm 7.7$

Table 4.5: Normalization factors and predicted event yields for the nominal and alternate definitions of the template region. Regions R4 and R5 have loose Higgs lepton in the control regions (but passing Medium ID in signal region). This study was conducted using a different generator for the diboson background, so there is a slight shift compared to quoted values in the text. The uncertainties quoted here are due to the data statistics and the finite number of generated MC. The uncertainty of the predicted yield that stems from the calculation of the normalization factor is shown second.

756 analysis.

757 Higgs and Z mass distributions are shown in Figure 4.7, after the full selection but each
758 without its respective mass window cut. Kinematic distributions for the optimized selection
759 in the signal region can be found in Figures 4.8. The uncertainty error band includes both
760 systematic and statistical uncertainties. The background prediction is in excellent agreement
761 with observed data.

762 4.5 Systematic Uncertainties

763 This section describes only systematic uncertainties pertinent to the use of simulated samples,
764 as those related to the data-driven background prediction of the template method are found
765 in the previous section. Because the uncertainty in the template method is high (37%), the
766 smaller uncertainties described here have a small impact in the final result. A summary of
767 the final uncertainties on simulated background, simulated signal and fake- τ_{had} background

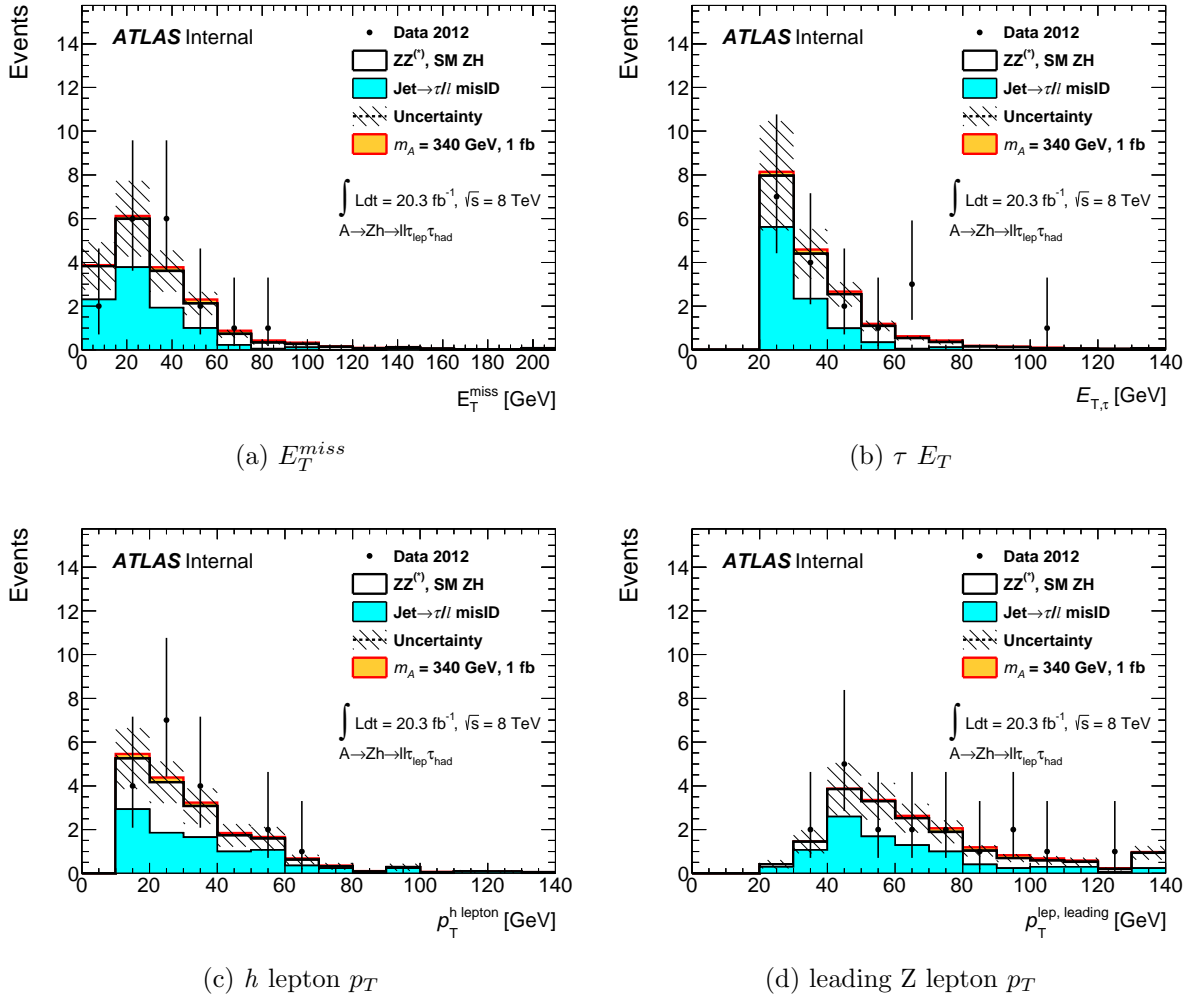


Figure 4.8: Comparisons of the distributions of kinematic variables for the full background prediction, observed data and a $m_A = 340 \text{ GeV}$ signal sample in the signal region.

779 *4.5.2 Detector-related uncertainties*

780 The simulated detector response and software performance in Monte Carlo generated events
781 has several systematic uncertainties. They can be related to:

- 782 • The reconstruction, identification and electron-veto efficiency of hadronic taus (τ_{had} -
783 ID).
- 784 • The reconstruction of the energy of the τ_{had} , referred to as the τ_{had} energy scale (TES).
- 785 • The efficiencies of the lepton triggers used, as well as the subsequent reconstruction,
786 isolation, identification and energy scale of simulated electrons and muons (Trig_Mu,
787 Mu_EFF, Mu_ES, Trig_El, El_EFF, El_ES).
- 788 • The reconstruction of jet energies and resolution (JES, JER).
- 789 • Pile-up uncertainties due to the reweighting of MC samples to match the average
790 interaction per bunch crossing ($\langle\mu\rangle$) profile of data events (PU).
- 791 • The E_T^{miss} calculation for simulated events (MET). Since the E_T^{miss} calculation is de-
792 pendent on all other physical objects, their respective uncertainties all impact the E_T^{miss}
793 uncertainty.

794 The dominant detector-related uncertainties are related to the TES and TauID, being as high
795 as 6%. Similar to all other uncertainties associated to simulated samples, they are dwarfed
796 by the overall 37% uncertainty in the fake- τ_{had} data-driven background prediction.

797 *4.5.3 Signal modelling uncertainties*

798 The kinematics of events generated with Monte Carlo do not match perfectly with those of
799 events in data. This mismodelling in the simulation can lead to a different acceptance of our

Sample	LUMI		EL_EFF		EL_ES		JER		JES		MET		Mu_EFF	
	up %	dn %	up %	dn %	up %	dn %	up %	dn %	up %	dn %	up %	dn %	up %	dn %
220	2.8	-2.8	1.3	-1.3	-1.1	-1.2	0.4	0.4	0.5	-0.7	0.1	-0.1	1.1	-1.1
240	2.8	-2.8	1.3	-1.3	0.5	-0.5	-0.1	0.1	-0.4	-0.4	-0.2	-0.5	1.1	-1.1
260	2.8	-2.8	1.3	-1.3	0.5	0.6	-0.04	-0.04	-0.4	-0.5	-0.4	-0.3	1.1	-1.1
300	2.8	-2.8	1.4	-1.4	0.2	0.5	0.03	0.02	-0.2	-0.6	0.1	0.1	1.1	-1.1
340	2.8	-2.8	1.4	-1.3	0.7	0.4	-0.1	-0.1	0.2	0.3	0.1	0.1	1.1	-1.1
350	2.8	-2.8	1.4	-1.4	-0.1	-0.3	-0.2	-0.2	0.3	0.1	0.1	0.1	1.1	-1.1
400	2.8	-2.8	1.4	-1.4	0.3	0.2	-0.2	-0.2	-0.1	0.3	0.1	0.2	1.1	-1.1
500	2.8	-2.8	1.5	-1.5	0.1	0.1	-0.2	-0.2	-0.1	-0.1	0.1	0.1	1.1	-1.1
800	2.8	-2.8	1.5	-1.5	-0.2	0.3	-0.1	-0.1	0.3	0.4	-0.1	-0.1	1.1	-1.1
1000	2.8	-2.8	1.6	-1.6	0.2	0.2	-0.1	-0.1	0.7	0.7	0.1	0.4	1.2	-1.1
MC Background	2.8	-2.8	1.5	-1.5	4.8	8.9	-2.6	-2.6	-4.9	0.3	2.0	-0.4	1.1	-1.1
Sample	Mu_ES		PU		TES		TRIG_EI		TRIG_Mu		τ_{had} -ID			
	up %	dn %	up %	dn %	up %	dn %	up %	dn %	up %	dn %	up %	dn %	up %	dn %
220	-0.4	0.1	3.9	-4.4	1.3	-1.0	0.1	-0.1	0.5	-0.5	3.3	-3.3		
240	0.2	0.1	3.7	-4.1	0.3	-0.7	0.1	-0.1	0.5	-0.5	3.3	-3.3		
260	-0.5	0.1	4.0	-4.5	0.8	-1.0	0.1	-0.1	0.5	-0.5	3.3	-3.3		
300	0.1	-0.2	3.8	-4.3	0.6	-0.8	0.1	-0.1	0.5	-0.5	3.3	-3.3		
340	-0.1	0.1	4.0	-4.5	0.9	-1.0	0.1	-0.1	0.5	-0.5	3.3	-3.3		
350	0.1	0.2	4.0	-4.5	0.6	-0.6	0.1	-0.1	0.5	-0.5	3.3	-3.3		
400	-0.1	0.1	4.0	-4.5	0.6	-0.5	0.1	-0.1	0.5	-0.5	3.3	-3.3		
500	0.1	0.1	4.1	-4.5	0.5	-0.7	0.1	-0.1	0.5	-0.5	3.3	-3.3		
800	0.1	0.1	3.8	-4.3	0.5	-0.2	0.1	-0.1	0.5	-0.5	3.3	-3.3		
1000	-0.3	-0.1	3.9	-4.4	0.2	-0.2	0.1	-0.1	0.5	-0.5	3.3	-3.3		
MC Background	1.5	-0.4	-1.0	1.0	6.0	-2.6	0.1	-0.1	0.5	-0.5	3.2	-3.2		

Table 4.6: Table showing the up and down detector systematic fluctuations of the $\tau_{lep}\tau_{had}$ MC signal and background samples after full selection, along with the corresponding statistical uncertainty

800 signal events, and is thus accounted for as an uncertainty on the normalization of our signal
 801 samples.

802 To gauge the impact of the ISR uncertainty, a variation of $\pm 20\%$ around the nominal
 803 value is done and its impact assessed. The effect of doubling and halving the factoriza-
 804 tion/renormalization factor is investigated using Madgraph5. The uncertainty on the nomi-
 805 nal PDF is estimated by checking the effect of replacing it with two others: MSTW20081o68c1
 806 [50] and NNPDF21_1o_as_0119_100 [51]. The effect of using MSTW20081o68c1 as PDF is
 807 shown in Table 4.12, and similarly in Table 4.11 for NNPDF21_1o_as_0119_100. Tables 4.7
 808 and 4.8 show the uncertainties due to changes in the factorization/renormalization scale.
 809 The second column is the nominal signal acceptance, while the third column is the acceptance
 810 after variation. The fourth column is the the ratio between the acceptance after variation
 811 and the nominal acceptance. The numbers in the last column are the difference between
 812 the nominal acceptance and acceptance after a $\pm 1\sigma$ variation of the combined statistical
 813 uncertainty of the two acceptances. Tables 4.9 and 4.10 show the uncertainty in the $\tau_{lep}\tau_{had}$
 814 channel arising from variations of ISR. The final total uncertainties due to ISR, Fac./Renorm.
 815 and choice of PDFs are 2.4%.

sample name	nominal acceptance	fac/renorm up acceptance	ratio	# of sigma diff
220 GeV	0.26510	0.2631	0.9925	0.3706
260 GeV	0.32160	0.3196	0.9938	0.3500
340 GeV	0.34465	0.3500	1.0155	0.9169
500 GeV	0.40955	0.4053	0.9896	0.7064
1000 GeV	0.52285	0.5229	1.0001	0.0082

Table 4.7: Factorization/Renormalization shift up uncertainty on acceptance of lephad chan-
 nel

sample name	nominal acceptance	fac/reform down acceptance	ratio	# of sigma diff
220 GeV	0.26510	0.2607	0.9834	0.8169
260 GeV	0.32160	0.3291	1.0233	1.3058
340 GeV	0.34465	0.3463	1.0048	0.2833
500 GeV	0.40955	0.3974	0.9703	2.0239
1000 GeV	0.52285	0.5291	1.0120	1.0221

Table 4.8: Factorization/Renormalization shift down uncertainty on acceptance of lephad channel

sample name	nominal acceptance	ISR up acceptance	ratio	# of sigma diff
220 GeV	0.26510	0.26185	0.98774	0.73777
260 GeV	0.32160	0.32050	0.99658	0.23561
340 GeV	0.34465	0.34890	1.01233	0.89297
500 GeV	0.40955	0.40075	0.97851	1.79262
1000 GeV	0.52285	0.51330	0.98173	1.91134

Table 4.9: ISR shift up uncertainty on acceptance of lephad channel

sample name	nominal acceptance	ISR down acceptance	ratio	# of sigma diff
220 GeV	0.26510	0.2577	0.9721	1.6842
260 GeV	0.32160	0.3269	1.0163	1.1216
340 GeV	0.34465	0.3429	0.9948	0.3790
500 GeV	0.40955	0.4033	0.9846	1.2827
1000 GeV	0.52285	0.5158	0.9864	1.4211

Table 4.10: ISR shift down uncertainty on acceptance of lephad channel

sample name	nominal acceptance	change PDF	ratio	# of sigma diff
220 GeV	0.26510	0.2607	0.9834	0.8169
260 GeV	0.32160	0.3095	0.9624	2.1297
340 GeV	0.34465	0.3407	0.9885	0.6799
500 GeV	0.40955	0.4026	0.9830	1.1561
1000 GeV	0.52285	0.5144	0.9838	1.3807

Table 4.11: acceptance uncertainties on NNPDF21_lo_as.0119_100 PDF of lephad channel

sample name	nominal acceptance	change PDF	ratio	# of sigma diff
220 GeV	0.26510	0.2670	1.0072	0.3509
260 GeV	0.32160	0.3177	0.9879	0.6832
340 GeV	0.34465	0.3400	0.9865	0.8006
500 GeV	0.40955	0.3988	0.9738	1.7900
1000 GeV	0.52285	0.5116	0.9785	1.8381

Table 4.12: acceptance uncertainties on MSTW2008lo68cl PDF of lephad channel

$\tau_{lep}\tau_{had}$ channel systematics		
Sample	Systematic	Uncertainty (%)
MC background	SM h tautau BR	0.60
MC background	luminosity	2.80
MC background	tau ID	0.40
MC background	PDF gg	0.50
MC background	pdf Higgs qq	0.40
MC background	PDF qq	3.30
MC background	QCD scale gg	1.70
MC background	QCD scale qq	3.30
MC background	QCD scale Vh	0.30
Total (for Background)		5.79
Fake background	Data driven norm.	37.70
Signal	electron efficiency	1.40
Signal	electron energy scale	0.50
Signal	ATLAS ggAZh Acc ISR	0.50
Signal	ATLAS ggAZh Acc PDF	2.30
Signal	ATLAS ggAZh Acc Scale	0.20
Signal	JER	0.30
Signal	JES	0.60
Signal	luminosity	2.80
Signal	muon trigger	0.50
Signal	muon efficiency	1.10
Signal	muon scale	0.20
Signal	pile-up	4.30
Signal	tau ID	3.30
Signal	tau energy scale	0.80
Total (for Signal)		6.90

Table 4.13: Overview of the $\tau_{lep}\tau_{had}$ channel systematic uncertainties as implemented in the fit model.

816 **4.6 Results**

817 The parameter of interest in the search is the signal strength μ , given by the ratio of the
 818 fitted signal production cross section times branching ratio to its counterpart value predicted
 819 by the 2HDM signal assumption. Thus, the case $\mu = 0$ corresponds to signal events being
 820 absent, while $\mu = 1$ suggests a signal presence that is compatible with the assumption under
 821 study. The statistical compatibility of the result with different μ assumptions is done via
 822 a binned likelihood function from the product of Poisson probability terms, as explained in
 823 Appendix B.

824 Table 4.14 shows the final event numbers after unblinding of the signal region. The final
 825 distribution of m_A^{rec} , after applying our complete background prediction methodology and
 826 including all statistical and systematic uncertainties, is shown in Figure 4.9. The observed
 827 data is in good agreement with the predicted background and no statistically significant
 828 excess is observed. Thus, upper limits on the signal production cross section times branching
 829 ratio are derived at 95% confidence level (see Figure 4.10) using the modified frequentist
 830 approach (CL_S), as described in Appendix B. Regions of the parameter space that have signal
 831 predictions incompatible with these limits are shown in Figure 4.11 for both type-I and type-
 832 II 2HDM. The interpretation assumes the heavy Higgs masses are degenerate, and that the
 833 mixed mass term in the 2HDM lagrangian is given by $m_{12}^2 = m_A^2 \tan \beta / (1 + \tan^2 \beta)$ (see
 834 Equation 2.21).

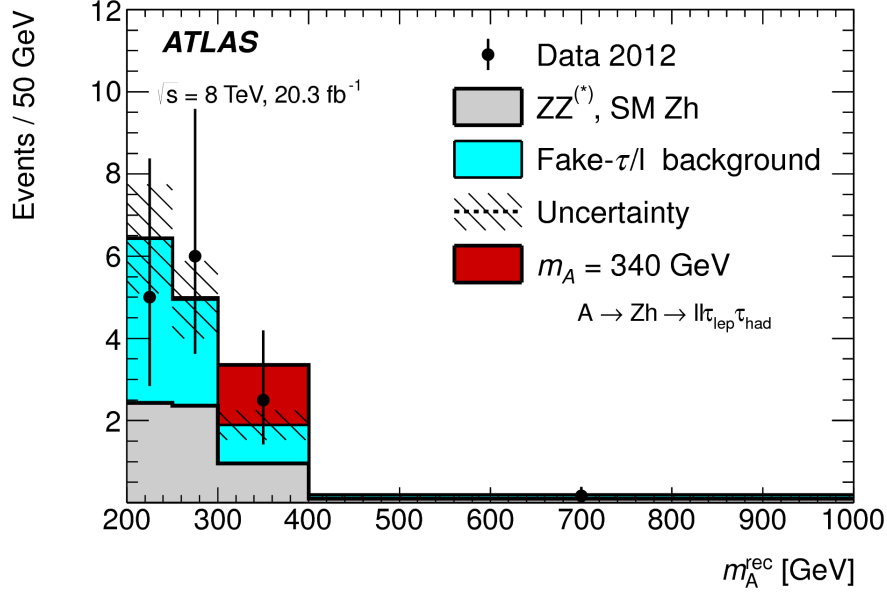


Figure 4.9: The reconstructed A boson mass, m_A^{rec} , for the full $\tau_{lep}\tau_{had}$ selection. The truth-matched background from simulation is shown stacked on the data-normalized template. The signal point shown here corresponds to $\sigma(gg \rightarrow A) \times BR(A \rightarrow Zh \rightarrow ll\tau\tau) = 1 \text{ fb}^{-1}$. For more details see the text.

Sample	$ll\tau_{lep}\tau_{had}$
ZZ	$6.97 \pm 0.17 \pm 0.40$
SM Zh	$0.85 \pm 0.02 \pm 0.09$
Others	$0.10 \pm 0.01 \pm 0.01$
Data-driven	$9.44 \pm 0.76 \pm 3.54$
Sum	$17.4 \pm 0.8 \pm 3.6$
Data	18
Signal	5.4 ± 0.4

Table 4.14: Final event yields of the $A \rightarrow Zh \rightarrow ll\tau_{lep}\tau_{had}$ search. The signal is given for a mass of 300 GeV, and assuming a cross section times branching ratio of 10 fb^{-1} .

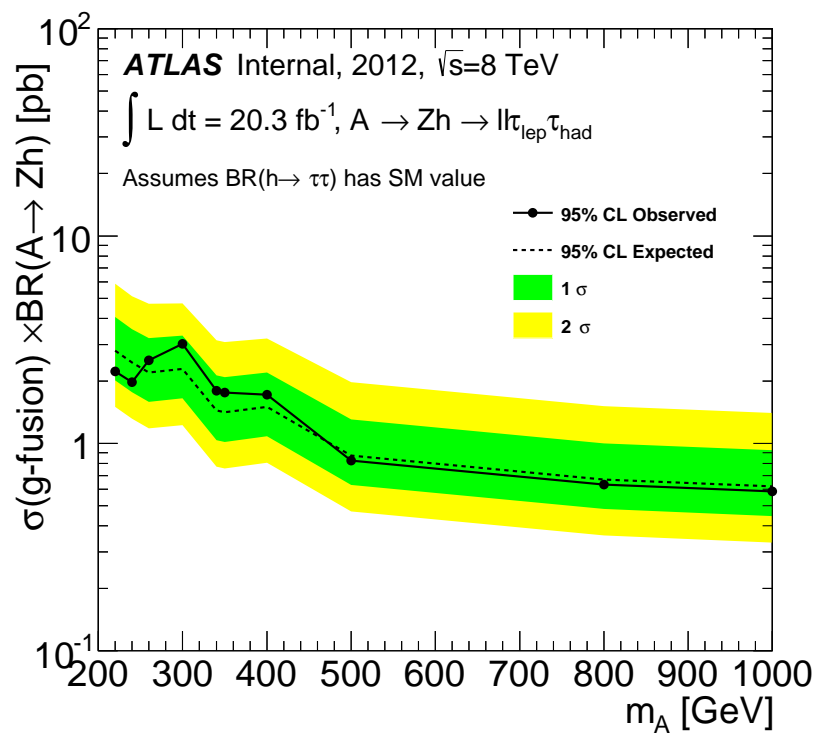


Figure 4.10: Expected and observed 95% CL upper limits of $\sigma(\text{gluon-fusion}) \times BR(A \rightarrow Zh \rightarrow ll\tau_{lep}\tau_{had})$ as a function of m_A .

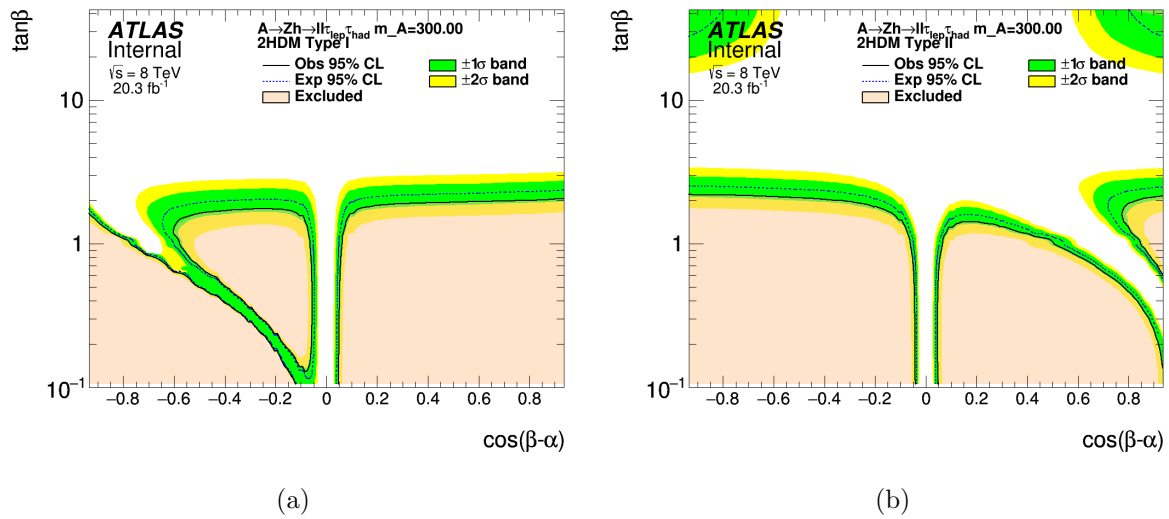


Figure 4.11: Excluded parameter space of type-I (a) and type-II (b) 2HDM derived from $A \rightarrow Zh \rightarrow \tau_{lep}\tau_{had}$ search result.

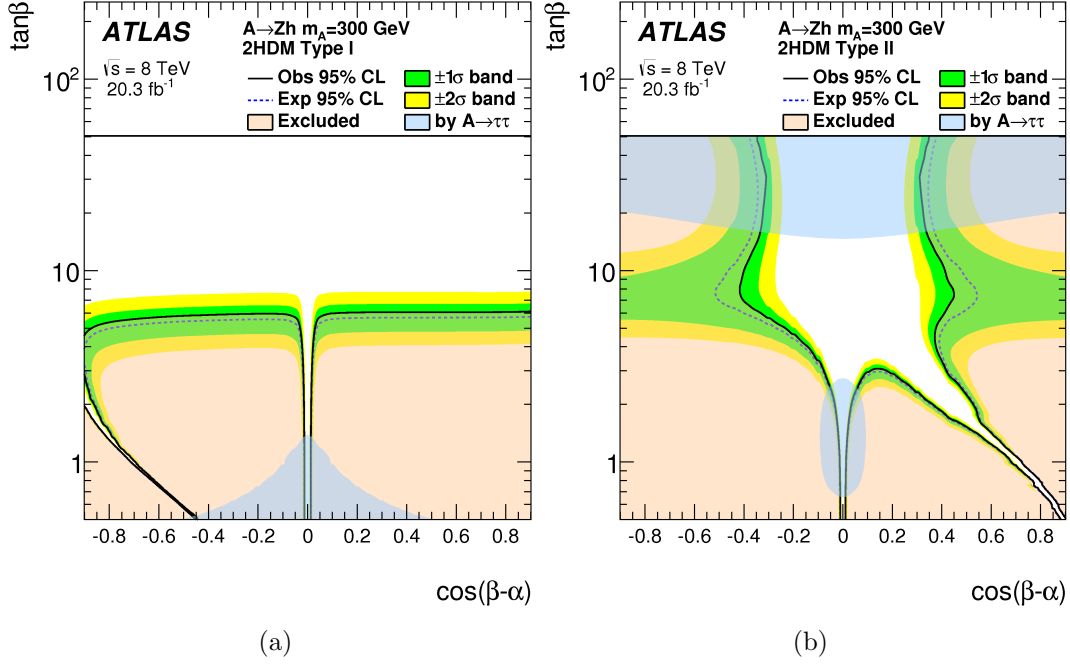


Figure 4.12: Exclusions in the $\cos(\beta - \alpha) - \tan \beta$ plane of the combined $(\ell\ell\tau\tau, \nu\nu\tau\tau, bb\tau\tau)$ $A \rightarrow Zh$ search for type-I and type-II 2HDM. The blue shaded area is the exclusion provided by the Run-1 $A \rightarrow \tau\tau$ search result. Plots from Reference [52].

835 This marks the first time the $A \rightarrow Zh \rightarrow \ell\tau\tau$ search is done in ATLAS. The result was
 836 published combined with four other decay channels: $\ell\ell\tau_{lep}\tau_{lep}$, $\ell\ell\tau_{had}\tau_{had}$, $\nu\nu\tau\tau$, $bb\tau\tau$ [52].
 837 The combined analysis also did not find significant deviations from the SM prediction. The
 838 combined results are interpreted for general types of 2HDM, leading to large exclusions of
 839 the allowed parameter space, as shown in Figure 4.12.

Chapter 5

NEUTRAL MSSM $A/H \rightarrow \tau_{lep}\tau_{had}$

In this chapter we describe the search for heavy MSSM-compatible A, H neutral Higgs bosons compatible decaying to a tau pair using LHC proton-proton collision data at a center-of-mass energy of 13 TeV and 3.2 fb⁻¹ integrated luminosity collected with the ATLAS detector. The search is done in the $\tau_{lep}\tau_{had}$ final state, where one tau decays leptonically and the other hadronically. As discussed in Chapter 2, the MSSM Higgs couplings to down-type fermions is enhanced, especially for high values of $\tan\beta$. Thus, decays to $b\bar{b}$ and $\tau\tau$ dominate, where the former is disfavored by the large QCD background at the LHC. Another consequence is that the b -associated production mode is enhanced, so that a gain in sensitivity can be obtained by categorizing the signal region according to the presence or absence of b -tagged jets. Here we present the search for $A/H \rightarrow \tau\tau$ in the b -veto category of the $\tau_{lep}\tau_{had}$ final state.

5.1 Samples

5.1.1 Data Sample

This analysis uses proton-proton collision data recorded by the ATLAS detector during 2015 (Run-2) at a center-of-mass energy of 13 TeV. Since this channel relies on vetoing events with b -tagged jets, data where the IBL was turned off is not included. This leads to a total integrated luminosity of 3.2 fb⁻¹.

5.1.2 Monte Carlo Simulated Samples

Monte Carlo simulated samples were generated for W +jets, Z +jets, $t\bar{t}$, single top and diboson production. The W +jets and Z +jets events were generated using POWHEG [53] and

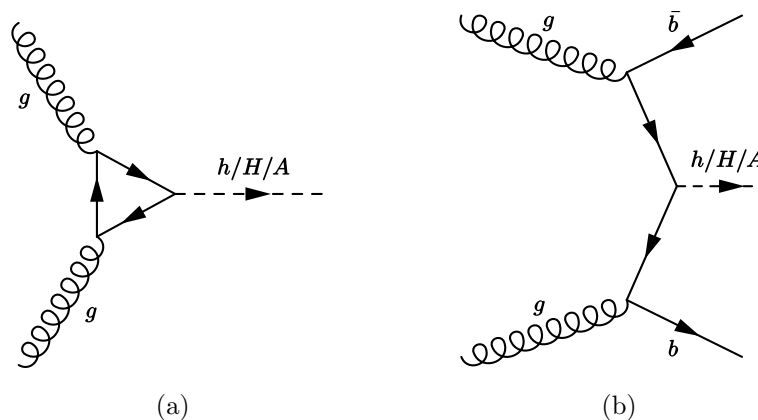


Figure 5.1: Lowest order Feynman diagrams for gluon fusion (a) and b -associated production (b) of a neutral MSSM Higgs boson.

862 showered with Pythia8 [54]. Separate high-mass vector-boson samples are generated for off-
 863 shell decays. POWHEG is also used for $t\bar{t}$ and single top samples, but with parton showering
 864 done with Pythia6 [55]. Diboson samples were both generated and showered using SHERPA
 865 [34].

866 As mentioned before, signal events can originate from two different processes: gluon-
 867 fusion and b -associated production (as shown in Figure 5.1). For b -associated production, the
 868 event generation is done with MadGraph5_aMC@NLO 2.1.2 [56, 57] for Higgs masses rang-
 869 ing from 200 to 1200 GeV. Samples from gluon-fusion production were simulated using
 870 POWHEG. Both signal types had their parton showering and hadronisation simulated with
 871 Pythia 8.2 [54]. A significant fraction of b -associated production events have negative MC
 872 weights so that we need a large number of events for this process. To this end, the faster
 873 simulation framework ALTFast-II has been used [58]. The simulated detector response of
 874 all generated samples is done with GEANT4 [38], except for bbH signal samples since they
 875 use the faster simulation provided by ALTFast-II.

876 **5.2 Reconstruction**

877 The signal events in this search have electrons, muons and taus in the final state. We also
 878 make use of b -tagging to veto events with b -tagged jets, and rely on missing transverse energy
 879 to refine our signal region selection and define control regions. Similarly to the $A \rightarrow Zh$
 880 analysis, it is crucial to have well developed reconstruction software to identify low-level
 881 detector signals with physical particles.

882 *5.2.1 Electrons*

883 Electron candidates originate from energy deposits in the EM calorimeter that have charged-
 884 particle tracks in the Inner Detector compatible with them. A likelihood-based identifica-
 885 tion algorithm is used to reject misidentified jets or events from photon conversion [59].
 886 Three quality levels are defined and candidates passing the “loose” criteria are consid-
 887 ered for overlap removal. We also require the candidate to have $E_T > 30$ GeV (where
 888 $E_T \equiv E_{cluster} / \cosh(\eta_{track})$) and to be in the $|\eta| < 2.47$ region. A “gradient” isolation criteria
 889 is required where the surrounding cone (defined by $\Delta R < 0.2$) must have 1-10% of the elec-
 890 tron energy. This threshold varies in electron transverse momentum, being 90 (99)% efficient
 891 at $p_T = 25$ (60) GeV.

892 *5.2.2 Muons*

893 Muon candidates are reconstructed from tracks in the muon spectrometer. All candidates
 894 must have $p_T > 30$ GeV and $|\eta| < 2.5$. Muons in ATLAS are reconstructed from several
 895 different algorithms [60]. Similarly to electrons, they are required to be isolated with the
 896 same “gradient” criteria and pass a “loose” quality requirement.

897 *5.2.3 Jets*

898 For Run-2, jets are again reconstructed using the anti- kt algorithm and cone size $R = 0.4$
 899 [43]. For better pileup suppression the Jet Vertex Tagger (JVT) algorithm is used [61]. The

900 JVT is a multivariate classifier that uses jet energy, tracking and vertexing information of
 901 the reconstructed jet to assign a score that reflects the probability the object is not due to
 902 pileup. Specifically, we require a JVT score greater than 0.64 for jets with $p_T < 50$ and
 903 $|\eta| < 2.4$.

904 5.2.4 *b-tagging*

905 Jets flagged as originating from b -hadrons are called b -tagged jets. We require them to pass
 906 all quality criteria that are applied to regular jets, and the MV2c20 algorithm is used for
 907 identifying b -tagged jets [62]. This algorithm is tuned to be 70% efficient in selecting b -
 908 originated jets from a $t\bar{t}$ sample, and has mis-identification rates of 10%, 4% and 0.2% when
 909 applied on c -jets, τ -jets and light-quark or gluon initiated jets, respectively.

910 5.2.5 *Taus*

911 Taus that decay hadronically are nearly always characterized by one or three tracks, corre-
 912 sponding to the number of charged pions in the hadronic decay. Tau decays also produce
 913 neutrinos and neutral pions so tau candidates are characterized by a small-angle shower in
 914 the calorimeter and few tracks. All jets with $p_T > 10$ GeV are initially considered to be τ_{had}
 915 candidates. The tau candidates must then have either have one or three tracks, have a visible
 916 transverse momentum greater than 20 GeV, pseudo-rapidity less than 2.5, and be outside
 917 the calorimeter transition region. Hadronic taus with one or three tracks are also called
 918 1-prong or 3-prong taus, respectively. The TauID classifier used in Run-1 has been updated
 919 in Run-2 to cope with the different pileup profile, as well as improve rejection through the
 920 use of new kinematic variables. The specific updates to the Run-2 TauID algorithm can be
 921 found in Appendix A. Three quality criteria are defined for hadronic taus and the “medium”
 922 working point is chosen for the final analysis. However, for object overlap removal only the
 923 leading tau is used, regardless of TauID quality, as long as it has $p_T > 10$ GeV and $|\eta| < 2.5$.
 924 Electrons are also often mis-identified as hadronically decaying taus. To reduce the e -to- τ
 925 fake rate, taus that geometrically overlap with loosely identified electrons are discarded. The

926 quality threshold on the electron candidates is such that a 95 % efficiency for reconstructing
 927 hadronic taus is obtained in a $Z \rightarrow \tau\tau$ sample. The tau candidates must also be either 1 or
 928 3-prong, i.e. have one or three tracks, have a visible transverse momentum greater than 20
 929 GeV, pseudo-rapidity less than 2.5 and be outside the calorimeter transition region.

930 *5.2.6 Missing Transverse Energy*

931 Similar to the $A \rightarrow Zh$ analysis, the E_T^{miss} is defined as the opposite of the \vec{p}_T sum of all
 932 reconstructed objects in an event [63]. This analysis uses the Track-based Soft Term (TST)
 933 algorithm [64], which uses ID tracks from the primary vertex to create a “soft term” that
 934 improves the resolution and performance of the E_T^{miss} calculation over a wide range pileup
 935 scenarios.

936 *5.2.7 Object Overlap Removal*

937 The following priority is used when removing multiple objects that overlap:

- 938 • Jets within a $\Delta R = 0.2$ cone of the hadronically-decaying τ with highest transverse
 939 momentum are excluded.
- 940 • Jets within a $\Delta R = 0.4$ cone of electrons or muons are excluded.
- 941 • τ_{had} 's within a $\Delta R = 0.2$ cone of electrons or muons are excluded.
- 942 • Electrons within a $\Delta R = 0.2$ cone of muons are excluded.

943 For overlap removal purposes, a lower p_T requirement of 15 GeV for electrons and 7 GeV for
 944 muons is imposed.

945 **5.3 Event Selection**

946 This section contains a description of the selection criteria used in the $H/A \rightarrow \tau_{lep}\tau_{had}$ b -veto
 947 analysis. The $\tau_{lep}\tau_{had}$ b -veto channel must have one light lepton and one hadronic tau in the

948 final state, both passing “medium” identification requirements, and no b -tagged jets. The
 949 transverse momentum of the light lepton (tau) must be greater than 30 (25) GeV. Events are
 950 also required to have a vertex with at least four associated tracks. An $|\eta| < 2.3$ cut is applied
 951 to the τ_{had} for two reasons, the first being that the high η region has only a small fraction of
 952 signal events. The second reason is that there is a significant amount of misidentified $Z \rightarrow ee$
 953 events that is hard to estimate due to the fact that the e -to- τ fake rate in this region is very
 954 poorly modeled in simulation. Finally, the electron and tau must have opposite-sign charges.
 955 Events where the τ_{lep} decays to an electron are said to belong to the electron channel ($e\tau_{had}$),
 956 and events where τ_{lep} decays to a muon make up muon channel ($\mu\tau_{had}$). The discriminant
 957 variable used in this analysis is the total transverse mass (m_T^{tot}), for which a description can
 958 be found at the end of this section.

959 5.3.1 $e\tau_{had}$

960 Due to their higher efficiencies and lower systematic errors, single electron or single muon trig-
 961 gers are used over hadronic tau triggers. Specifically, the triggers `e24_lhmedium_L1EM20VH`,
 962 `e60_lhmedium` and `e120_lhloose` are used (in data events the `e24_lhmedium_L1EM20VH`
 963 trigger is replaced by the `e24_lhmedium_L1EM18VH` trigger). The electron must be trigger-
 964 matched, i.e. overlap with the object that triggered the event. All electrons must pass
 965 “medium” likelihood identification, and events with two or more “loose” electrons or muons
 966 are vetoed in order to reject $Z/\gamma^* \rightarrow \ell\ell$ production (“dilepton veto”). In spite of the selection
 967 cuts above, there is still a significant fraction of $Z \rightarrow ee$ events misidentified in our signal
 968 region, so a Z -mass veto is applied to the reconstructed visible mass of the $\tau_{lep}\tau_{had}$ system
 969 ($m_{\tau\tau}^{vis} < 80$ GeV or $m_{\tau\tau}^{vis} > 110$). A more detailed description of the treatment of $e \rightarrow \tau_{had}$
 970 background events is found in Section 5.4.2.

971 5.3.2 $\mu\tau_{had}$

972 A $\mu\tau_{had}$ event must pass at least one of the `mu20_iloose_L1MU15` and `mu50` triggers. The
 973 same dilepton veto as in the $e\tau_{had}$ channel must be satisfied, and trigger-matching of the

974 muon is again required. The muon must pass the “medium” quality identification require-
 975 ment. Again, the muon and tau must have opposite-sign charges.

976 5.3.3 Selection Optimization

977 The cuts above are sufficient for selecting our signal events, but they do not yet take ad-
 978 vantage of the kinematic differences between signal and background processes. The two cuts
 979 below significantly improve the sensitivity of this channel:

- 980 • $\Delta\phi(\tau, \ell) > 2.4$.
- 981 • $m_T(\ell, E_T^{miss}) < 40$ GeV, where $m_T(\ell, E_T^{miss}) \equiv \sqrt{2p_{T,\ell}E_T^{miss}(1 - \cos \Delta\phi(\ell, E_T^{miss}))}$.

982 The $\Delta\phi(\tau, \ell) > 2.4$ cut is because the τ 's from the Higgs boson decay in an approximately
 983 back-to-back topology. The second cut on the transverse mass exploits the fact that m_T
 984 peaks near the W boson mass (80 GeV) for W +jets background events. Signal events
 985 however have low transverse mass because $\cos \Delta\phi(\ell, E_T^{miss})$ tends to be low. This occurs
 986 because leptonically-decaying taus have two neutrinos and hadronically-decaying taus have
 987 one, causing the reconstructed E_T^{miss} to be approximately collinear to the light lepton. This
 988 behavior can be seen in Figure 5.2. Event yields at different stages of the selection cutflow
 989 can be found in Tables 5.1-5.4.

990 5.3.4 Total Transverse Mass

991 The reconstruction of the tau pair mass is essential to obtain a good separation between signal
 992 and background events. However, because of the presence of neutrinos from the tau decays,
 993 mass reconstruction can be difficult. The final discriminant chosen is the total transverse
 994 mass m_T^{tot} , defined as:

$$m_T^{tot} \equiv \sqrt{m_T^2(E_T^{miss}, \tau_1) + m_T^2(E_T^{miss}, \tau_2) + m_T^2(\tau_1, \tau_2)} \quad (5.1)$$

995 where $m_T(a, b)$ is defined as:

$$m_T(a, b) \equiv \sqrt{2p_T(a)p_T(b)(1 - \cos \Delta\phi(a, b))} \quad (5.2)$$

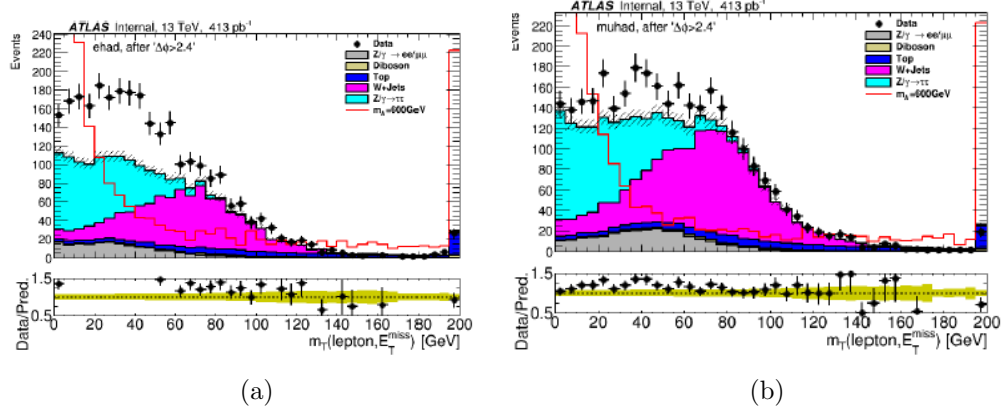


Figure 5.2: Distribution of the transverse mass $m_T(\ell, E_T^{miss})$ for the (a) $e\tau_{had}$ and (b) $\mu\tau_{had}$ channels.

Table 5.1: Electron channel cutflow. The predictions correspond to a luminosity of 3.2 fb^{-1} . The errors are due solely to the finite number of simulated events.

Cut: Backgrounds	Top			$Z \rightarrow \tau\tau + \text{jets}$		
	Events	jet $\rightarrow \tau_{had}$ (%)	$e \rightarrow \tau_{had}$ (%)	Events	jet $\rightarrow \tau_{had}$ (%)	$e \rightarrow \tau_{had}$ (%)
pre-selection	3316.2 ± 11.2	27.7	2.8	7102.3 ± 54.5	0.9	0.0
$\Delta\phi(\tau, \ell) > 2.4$	1354.4 ± 7.1	22.0	2.6	5516.2 ± 47.8	0.7	0.0
$m_T(\ell, E_T^{miss})$	221.0 ± 2.9	33.4	3.2	4286.2 ± 42.2	0.7	0.0
b -veto	51.9 ± 1.4	36.1	2.0	4216.5 ± 41.7	0.7	0.0
Cut: Backgrounds	$W + \text{jets}$			Diboson		
	Events	jet $\rightarrow \tau_{had}$ (%)	$e \rightarrow \tau_{had}$ (%)	Events	jet $\rightarrow \tau_{had}$ (%)	$e \rightarrow \tau_{had}$ (%)
pre-selection	12258.0 ± 146.4	99.4	0.0	524.4 ± 5.6	22.0	3.6
$\Delta\phi(\tau, \ell) > 2.4$	6340.7 ± 105.5	99.3	0.0	261.1 ± 3.6	15.8	3.9
$m_T(\ell, E_T^{miss})$	1142.8 ± 44.8	99.5	0.0	53.3 ± 1.8	20.3	8.5
b -veto	1116.3 ± 44.0	100.0	0.0	51.2 ± 1.7	19.1	8.6
Cut: Backgrounds	$Z \rightarrow \ell\ell + \text{jets}$					
	Events	jet $\rightarrow \tau_{had}$ (%)	$e \rightarrow \tau_{had}$ (%)			
pre-selection	1796 ± 29	30.9	69.0			
$\Delta\phi(\tau, \ell) > 2.4$	1377 ± 26	21.2	78.7			
$m_T(\ell, E_T^{miss})$	920 ± 21	17.7	82.3			
b -veto	907 ± 21	17.6	82.4			

Table 5.2: Electron channel cutflow for signal samples. The predictions correspond to a luminosity of 3.2 fb^{-1} and a cross section of 1 pb^{-1} . The errors are due solely to the finite number of simulated events.

Cut: Signal $e\tau_{had}$		ggH200	ggH300	ggH400	ggH500	
pre-selection		52.8 ± 1.4	105.0 ± 2.0	144.5 ± 2.4	166.8 ± 2.6	
$\Delta\phi(\tau, \ell) > 2.4$		45.4 ± 1.3	96.2 ± 1.9	137.7 ± 2.4	160.1 ± 2.5	
$m_T(\ell, E_T^{miss})$		31.2 ± 1.1	60.5 ± 1.5	89.8 ± 1.9	103.2 ± 2.0	
b -veto		30.7 ± 1.1	58.9 ± 1.5	87.0 ± 1.9	99.8 ± 2.0	
Cut: Signal $e\tau_{had}$		ggH600	ggH700	ggH800	ggH1000	ggH1200
pre-selection	181.0 ± 3.0	182.5 ± 3.0	187.9 ± 3.0	177.5 ± 2.9	167.9 ± 2.8	
$\Delta\phi(\tau, \ell) > 2.4$	173.8 ± 2.9	176.9 ± 2.9	182.3 ± 3.0	172.1 ± 2.9	163.7 ± 2.8	
$m_T(\ell, E_T^{miss})$	108.8 ± 2.3	112.2 ± 2.3	113.9 ± 2.4	101.7 ± 2.2	95.3 ± 2.1	
b -veto	105.2 ± 2.3	108.5 ± 2.3	109.0 ± 2.3	97.4 ± 2.1	90.7 ± 2.1	
Cut: Signal $e\tau_{had}$		bbH200	bbH300	bbH400	bbH500	
pre-selection		53.0 ± 1.6	106.0 ± 2.3	139.2 ± 2.3	157.3 ± 2.8	
$\Delta\phi(\tau, \ell) > 2.4$		48.0 ± 1.5	99.2 ± 2.2	131.5 ± 2.2	149.4 ± 2.7	
$m_T(\ell, E_T^{miss})$		33.1 ± 1.2	65.7 ± 1.8	81.9 ± 1.8	92.2 ± 2.1	
b -veto		25.5 ± 1.1	46.0 ± 1.5	53.6 ± 1.4	61.4 ± 1.7	
Cut: Signal $e\tau_{had}$		bbH600	bbH700	bbH800	bbH1000	bbH1200
pre-selection	169.6 ± 3.5	170.3 ± 3.3	168.8 ± 3.2	164.6 ± 2.8	151.7 ± 3.0	
$\Delta\phi(\tau, \ell) > 2.4$	163.0 ± 3.4	164.1 ± 3.2	163.1 ± 3.2	159.4 ± 2.7	148.1 ± 3.0	
$m_T(\ell, E_T^{miss})$	102.4 ± 2.7	100.2 ± 2.5	97.2 ± 2.4	89.6 ± 2.0	81.9 ± 2.2	
b -veto	65.1 ± 2.1	59.9 ± 2.0	57.4 ± 1.9	53.5 ± 1.6	48.0 ± 1.7	

996 A few other mass reconstruction techniques were investigated but found to have lower sig-
 997 nal/background separation power. The total transverse mass has higher discriminating power
 998 because multi-jet background events (i.e. events from QCD processes) have low E_T^{miss} values
 999 and, therefore, low m_T^{tot} .

1000 **5.4 Background Estimation**

1001 Events from several background processes can pass our signal selection. Similarly to the
 1002 $A \rightarrow Zh$ analysis of Chapter 4, it is useful to divide them into categories based on whether the
 1003 lepton or τ_{had} have or have not been correctly identified (“true” or “fake”). The background

Table 5.3: Muon channel cutflow. The predictions correspond to a luminosity of 3.2 fb^{-1} . The errors are due solely to the finite number of simulated events.

Cut: Backgrounds	Top			$Z \rightarrow \tau\tau$ +jets		
	Events	jet $\rightarrow \tau_{had}$ (%)	$e \rightarrow \tau_{had}$ (%)	Events	jet $\rightarrow \tau_{had}$ (%)	$e \rightarrow \tau_{had}$ (%)
pre-selection	3914.7 ± 11.7	28.6	2.6	8599.8 ± 58.5	0.9	0.0
$\Delta\phi(\tau, \ell) > 2.4$	1559.5 ± 7.4	24.2	2.4	6859.5 ± 52.1	0.7	0.0
$m_T(\ell, E_T^{miss})$	258.9 ± 3.0	34.4	3.0	5145.7 ± 45.2	0.8	0.0
b -veto	61.3 ± 1.4	39.3	2.6	5072.5 ± 44.7	0.7	0.0
Cut: Backgrounds	W +jets			Diboson		
	Events	jet $\rightarrow \tau_{had}$ (%)	$e \rightarrow \tau_{had}$ (%)	Events	jet $\rightarrow \tau_{had}$ (%)	$e \rightarrow \tau_{had}$ (%)
pre-selection	17590 ± 190	99.6	0.0	615.9 ± 5.7	24.1	3.6
$\Delta\phi(\tau, \ell) > 2.4$	9937 ± 140	99.5	0.0	314.0 ± 3.9	19.7	3.8
$m_T(\ell, E_T^{miss})$	1538 ± 55	99.5	0.0	61.9 ± 1.8	18.0	7.0
b -veto	1504 ± 54	99.5	0.0	60.1 ± 1.8	17.5	7.0
Cut: Backgrounds	$Z \rightarrow \ell\ell$ +jets					
	Events	jet $\rightarrow \tau_{had}$ (%)	$e \rightarrow \tau_{had}$ (%)			
pre-selection	2465 ± 32	19.6	80.4			
$\Delta\phi(\tau, \ell) > 2.4$	2050 ± 29	13.6	86.3			
$m_T(\ell, E_T^{miss})$	931 ± 19	8.7	91.3			
b -veto	920 ± 19	8.8	91.2			

1004 categories, and the processes that populate them, are:

- 1005 • Backgrounds with true hadronic tau and true light lepton, composed of $Z \rightarrow \tau_{lep}\tau_{had}$
- 1006 events and top events such as $t\bar{t} \rightarrow W^+W^-b\bar{b} \rightarrow \tau_{had}\ell\nu\bar{b}b$.
- 1007 • Backgrounds with true light lepton and a light lepton faking the τ_{had} , which consist
- 1008 mostly of $Z \rightarrow \ell\ell$ events
- 1009 • Backgrounds with true lepton and jet misidentified as a hadronic tau, composed mainly
- 1010 by W +jets events where the W decays leptonically, as well as a smaller contribution
- 1011 of Z/γ^* +jets events.
- 1012 • Backgrounds where both lepton and tau are misidentified, dominated by multi-jet

Table 5.4: Muon channel cutflow for signal samples. The predictions correspond to a luminosity of 3.2 fb^{-1} and a cross section of 1 pb^{-1} . The errors are due solely to the finite number of simulated events.

Cut: Signal $\mu\tau_{had}$	ggH200	ggH300	ggH400	ggH500	
pre-selection	68.5 ± 1.6	112.3 ± 2.0	135.9 ± 2.2	158.7 ± 2.4	
$\Delta\phi(\tau, \ell) > 2.4$	59.6 ± 1.5	102.4 ± 1.9	129.0 ± 2.2	152.0 ± 2.4	
$m_T(\ell, E_T^{miss})$	39.9 ± 1.2	64.7 ± 1.5	83.0 ± 1.8	96.1 ± 1.9	
<i>b</i> -veto	39.2 ± 1.2	62.9 ± 1.5	80.7 ± 1.7	93.0 ± 1.8	
Cut: Signal $\mu\tau_{had}$	ggH600	ggH700	ggH800	ggH1000	ggH1200
pre-selection	169.0 ± 2.8	178.3 ± 2.8	184.0 ± 2.9	179.2 ± 2.8	178.4 ± 2.8
$\Delta\phi(\tau, \ell) > 2.4$	163.0 ± 2.7	172.7 ± 2.8	178.5 ± 2.8	172.7 ± 2.8	173.4 ± 2.8
$m_T(\ell, E_T^{miss})$	101.9 ± 2.2	107.0 ± 2.2	110.5 ± 2.2	105.3 ± 2.2	101.0 ± 2.1
<i>b</i> -veto	98.3 ± 2.1	102.5 ± 2.1	105.9 ± 2.2	100.6 ± 2.1	96.0 ± 2.0
Cut: Signal $\mu\tau_{had}$	bbH200	bbH300	bbH400	bbH500	
pre-selection	65.4 ± 1.7	109.7 ± 2.2	132.6 ± 2.1	146.0 ± 2.6	
$\Delta\phi(\tau, \ell) > 2.4$	58.9 ± 1.6	101.2 ± 2.1	124.6 ± 2.1	137.7 ± 2.5	
$m_T(\ell, E_T^{miss})$	39.1 ± 1.3	65.4 ± 1.7	79.0 ± 1.6	82.5 ± 2.0	
<i>b</i> -veto	28.7 ± 1.1	45.6 ± 1.4	51.1 ± 1.3	53.0 ± 1.6	
Cut: Signal $\mu\tau_{had}$	bbH600	bbH700	bbH800	bbH1000	bbH1200
pre-selection	159.9 ± 3.2	170.4 ± 3.0	172.9 ± 3.0	171.7 ± 2.6	166.6 ± 3.0
$\Delta\phi(\tau, \ell) > 2.4$	152.1 ± 3.1	163.5 ± 3.0	166.2 ± 3.0	166.0 ± 2.6	162.3 ± 2.9
$m_T(\ell, E_T^{miss})$	93.8 ± 2.4	99.6 ± 2.3	97.8 ± 2.3	96.3 ± 1.9	89.9 ± 2.1
<i>b</i> -veto	57.9 ± 1.9	62.2 ± 1.8	58.7 ± 1.8	57.4 ± 1.5	55.2 ± 1.6

1013 processes.

1014 This section will describe the background estimation in each of the categories above.

1015 5.4.1 Background with true hadronic tau and lepton

1016 Monte Carlo simulated events are used whenever the reconstructed lepton and hadronic tau
 1017 are truth-matched to true-level leptons in the simulated event. As in the $A \rightarrow Zh$ search,
 1018 this includes events with a reconstructed τ_{had} truth-matched to a light lepton. Data-driven
 1019 calibration and scale factors are used to account for differences between simulated objects
 1020 and those found in data. Examples of these are the Tau Energy Scale (TES), which brings

1021 the simulated reconstructed tau energy closer to the actual detector response for hadronic
 1022 taus, and the TauID scale factor that corrects for efficiency differences of the TauID quality
 1023 requirement when applied to MC and data.

1024 5.4.2 Background with true lepton and lepton faking hadronic tau

1025 Events with electrons being misidentified as taus come mostly from $Z/\gamma^* \rightarrow ee$ and are
 1026 known to have their MC predicted yields different from what is observed in data. This
 1027 is particularly the case for the forward region ($|\eta| > 2$), as can be seen in Figure 5.3(b).
 1028 For these reasons we implement a Z -mass veto in the $e\tau_{had}$ channel and veto high- η taus
 1029 ($|\eta| < 2.3$) in both channels. The vetoed region corresponds to $80 < m_{\ell,\tau}^{vis} < 110$, and we
 1030 observe a 10-fold reduction in this background from this cut. For 3-prong events, the e -to-
 1031 τ_{had} fake rate is smaller so the vetoed region is reduced to $90 < m_{\ell,\tau}^{vis} < 100$ to reduce impact
 1032 on signal acceptance.

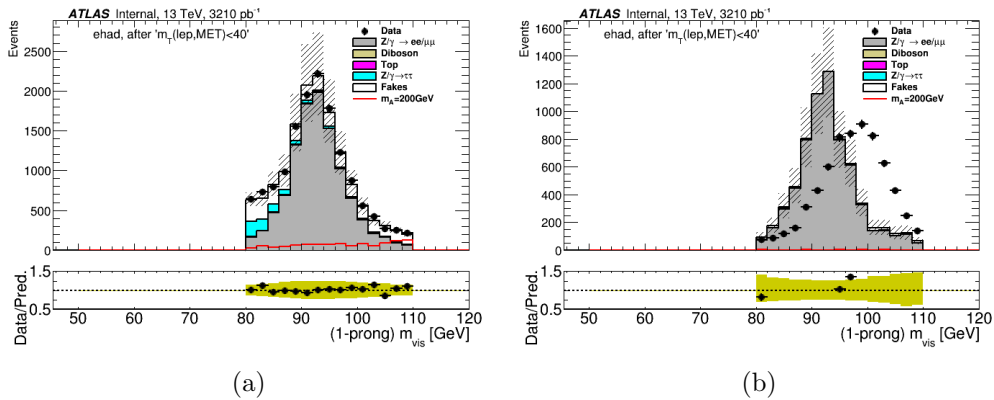


Figure 5.3: Visible mass distributions in the $e\tau_{had}$ channel for events with (a) $\eta < 2$ and (b) $|\eta| > 2.3$, after applying the η_{τ} -dependent scale factor .

1033 To correct for the mismodelling of the remaining background in this category, a scale
 1034 factor from the Z -mass control region is derived as a function of leading τ_{had} η . This control
 1035 region is defined by inverting the Z -mass cut, with the remainder of the signal region selec-

1036 tion kept the same. Events with misidentified leptons and/or taus are estimated using the
 1037 “combined fake-factor method” that is described in Section 5.4.5. Backgrounds with true
 1038 leptons and taus are taken from simulation with both statistical and systematic uncertainties
 1039 taken into consideration. The final 1-prong and 3-prong scale factors are shown in Figure
 1040 5.4. For 1-prong events, a conservative 20% uncertainty is used that represents the fraction
 1041 of subtracted simulated events in the Z -mass control region. For 3-prong, no evidence of
 1042 η -dependence is observed so a universal 1.15 ± 0.50 scale factor is used.

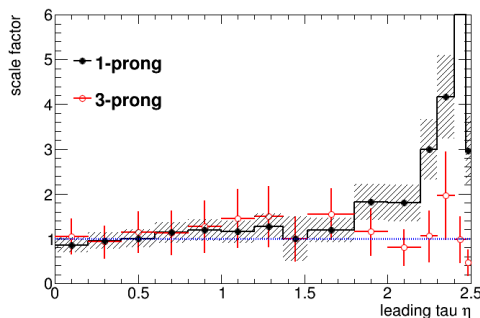


Figure 5.4: Scale factors for misidentified e -to- τ_{had} events.

1043 We can test the scale factors above by comparing distributions for variables other than
 1044 η_τ in the Z -mass control region, and confirming that the prediction matches the observed
 1045 data. Distributions of $m_T(\ell, \tau_{had})$ and m_T^{tot} for 1-prong and 3-prong are shown in Figures 5.5
 1046 and 5.6, and indicate the scale factors are successful in correcting the $e \rightarrow \tau_{had}$ fake rate in
 1047 MC events.

1048 5.4.3 Background with true lepton and jet misidentified as tau

1049 This background category is dominated by W +jets events where the W decays leptonically
 1050 and the jet is misidentified as a τ_{had} . Because the jet-to- τ_{had} fake rate is not well simulated
 1051 in MC, a data-driven fake factor method is used.

1052 The fake factor method consists of predicting the number of events with misidentified ob-

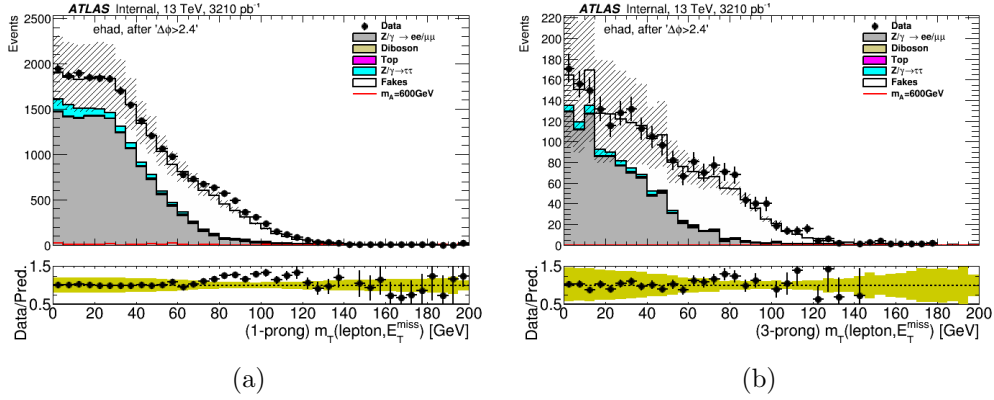


Figure 5.5: Distributions of $m_T(\ell, \tau_{had})$ for events with one-prong (a) and three-prong (b) τ_{had} before the $m_T(\ell, E_T^{miss})$ cut requirement.

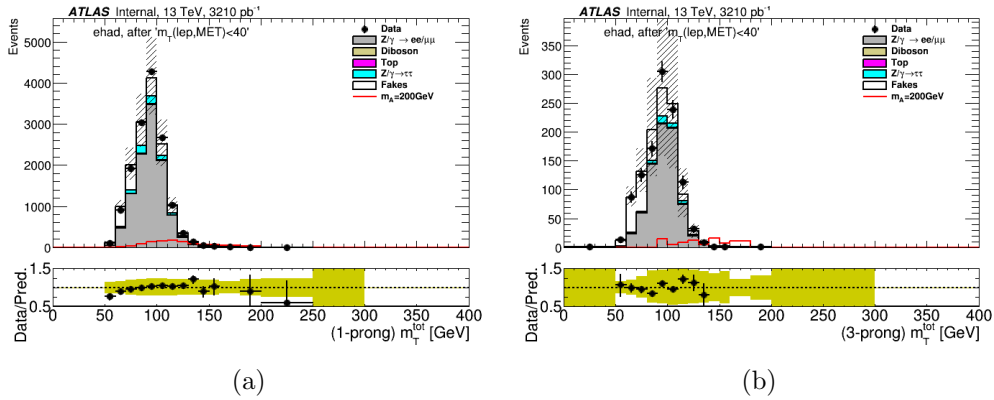


Figure 5.6: Distributions of the total transverse mass for events with one-prong (a) and three-prong (b) τ_{had} .

jects passing our selection by applying multiplicative factors to events that were successfully rejected by the identification criteria but otherwise pass the full signal region selection. They are defined as the ratio of the number of τ_{had} objects passing a given selection cut divided by the number failing the same cut in a control region that is almost exclusively populated by the objects whose misidentification rate we want to quantify. Fake factors are usually parameterized as a function of one or more kinematic variables that affect the efficiency of the selection cut used.

To compute W +jets fake factors, a W +jets control region is used where the $m_T(\ell, E_T^{miss}) < 40$ GeV cut is replaced by a high $m_T(\ell, E_T^{miss})$ requirement. In this control region, fake factors are computed using the ratio of events passing medium TauID divided by events failing medium TauID. They are computed as a function of the hadronic tau transverse momentum and number of tracks:

$$FF(W + jets) = \frac{N(\text{pass medium tau ID})}{N(\text{fail medium TauID and BDT} > 0.35)} \quad (5.3)$$

The full selection used to define the W +jets control region is:

- Exactly one light lepton passing the same identification criteria as the signal region.
- Events must pass the same dilepton veto used in the signal region.
- At least one τ_{had} candidate. For events failing the τ_{had} identification requirement, a τ_{had} -ID BDT score greater than 0.35 on the τ_{had} ID is required.
- $\Delta\phi(\tau, \ell) > 2.4$
- $m_T(\ell, E_T^{miss}) > 60$ GeV for the $\mu\tau_{had}$ channel.
- $m_T(\ell, E_T^{miss}) > 70$ GeV for the $e\tau_{had}$ channel.

The cut on the TauID BDT score causes the fractions of gluon-initiated and quark-initiated jets to match that in the signal region more closely. The cut on the transverse mass is tighter

1075 in the $e\tau_{had}$ channel to reject multi-jet background contamination and increase W +jets purity.
 1076 Since the fake factors are to be used for backgrounds with jets faking τ_{had} , events with
 1077 correctly identified τ_{had} or light leptons faking the τ_{had} are subtracted from the W +jets
 1078 control region.

1079 The distributions of several physically interesting variables is shown in Figures 5.7-5.9.
 1080 The excess in data events observed at low $m_T(\ell, E_T^{miss})$ is mostly due to multi-jet contamina-
 1081 tion. The distributions show disagreements both in normalization and shape between data
 1082 and simulation, which is why a data-driven fake factor method is necessary.

1083 The final W +jets fake factors are shown in Figure 5.10, compared to “fake factors”
 1084 computed in the low- m_T signal region. We do not expect very good agreement between
 1085 the fake factors of the opposing $m_T(\ell, E_T^{miss})$ regions due to the higher fraction of multi-jet
 1086 background at lower transverse mass. However, we see they are nevertheless in reasonable
 1087 agreement given the high uncertainty in their calculation (described below). The fake rate is
 1088 also dependent on the E_T^{miss} distribution in the event such that there is a poor modelling of
 1089 $\Delta\phi(\tau_{had}, E_T^{miss})$ and $\Delta\phi(\ell, E_T^{miss})$, as can be seen in Figure 5.11. Thus, an extra correction
 1090 is derived using $\Delta\phi(\tau_{had}, E_T^{miss})$ -dependent scale factors (shown in Figure 5.12). These are
 1091 calculated and applied separately for the $e\tau_{had}$ and $\mu\tau_{had}$ channels. Because the 1-track and
 1092 3-track scale factors show some variation in the $e\tau_{had}$ channel, the correction in that channel
 1093 uses separate 1-track and 3-track scale factors. An uncertainty of 15% is added to these scale
 1094 factors due to the subtraction of MC events with true objects in their calculation. Finally,
 1095 Figure 5.13 shows that the corrected fake factors are performing well by confirming that the
 1096 total transverse mass distribution observed in data agrees with that from the fake factor
 1097 prediction in the W +jets control region.

1098 *Systematic uncertainties in the W +jets fake factors*

1099 The error bars shown in Figure 5.10 contain both systematic and statistical uncertainties.
 1100 There are several sources of systematic errors in the W +jets background prediction:

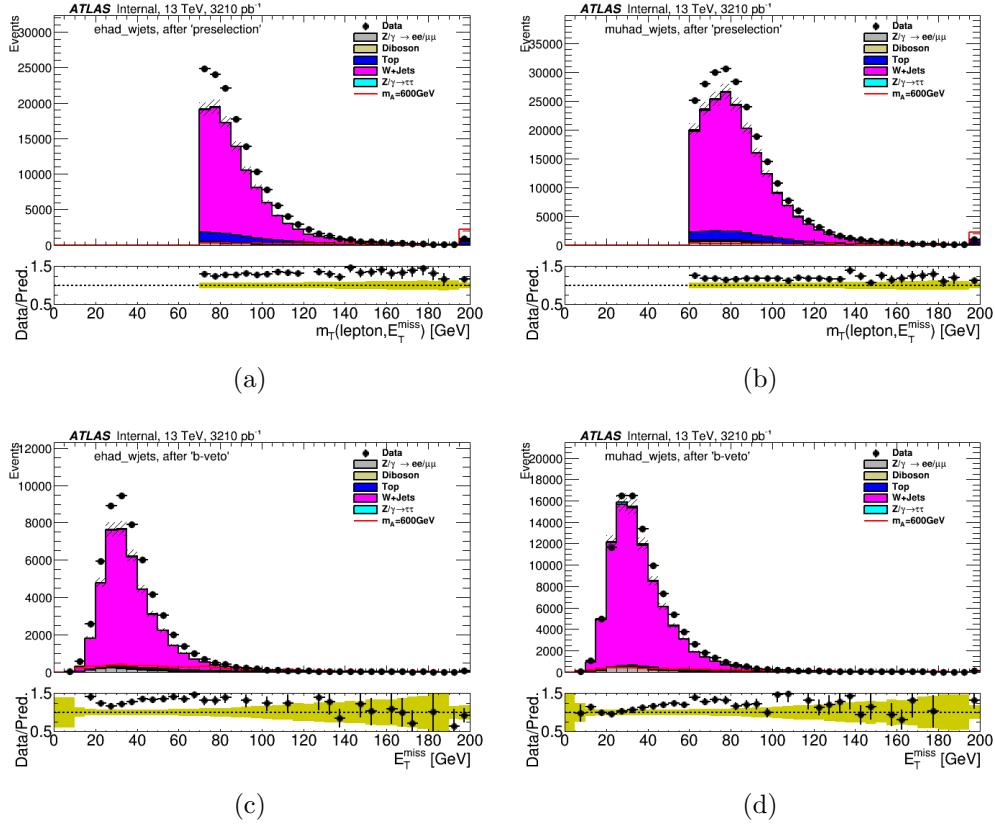


Figure 5.7: The $M_T(\ell, E_T^{miss})$ of the W +jets control region after preselection in the (a) electron and (b) muon channel, respectively. The E_T^{miss} distributions after the full W +jets control region selection is shown in (c) and (d). Only MC samples are shown for the prediction and no multi-jet estimation is included. The signal plotted here is $m_\phi = 600$ GeV, gluon-fusion produced with a cross section times branching ratio of 100 pb (far beyond the excluded region of the MSSM, which is below 0.1 pb.)

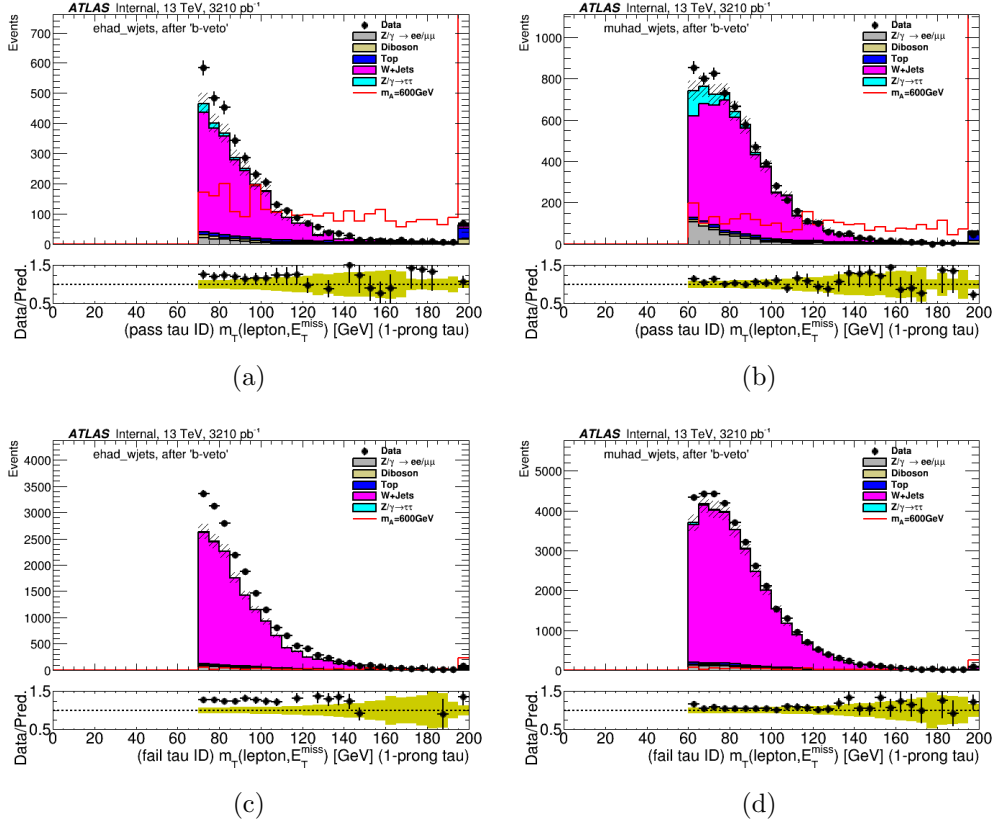


Figure 5.8: Distributions of $m_T(\ell, E_T^{miss})$ for events (a,b) passing and (c,d) failing the τ_{had} identification requirement in the W +jets control region and 1-prong τ_{had} . Only MC samples are shown for the prediction, no multi-jet estimation is included. The signal plotted here is $m_\phi = 600$ GeV, gluon-fusion produced with a cross section times branching ratio of 100 pb.

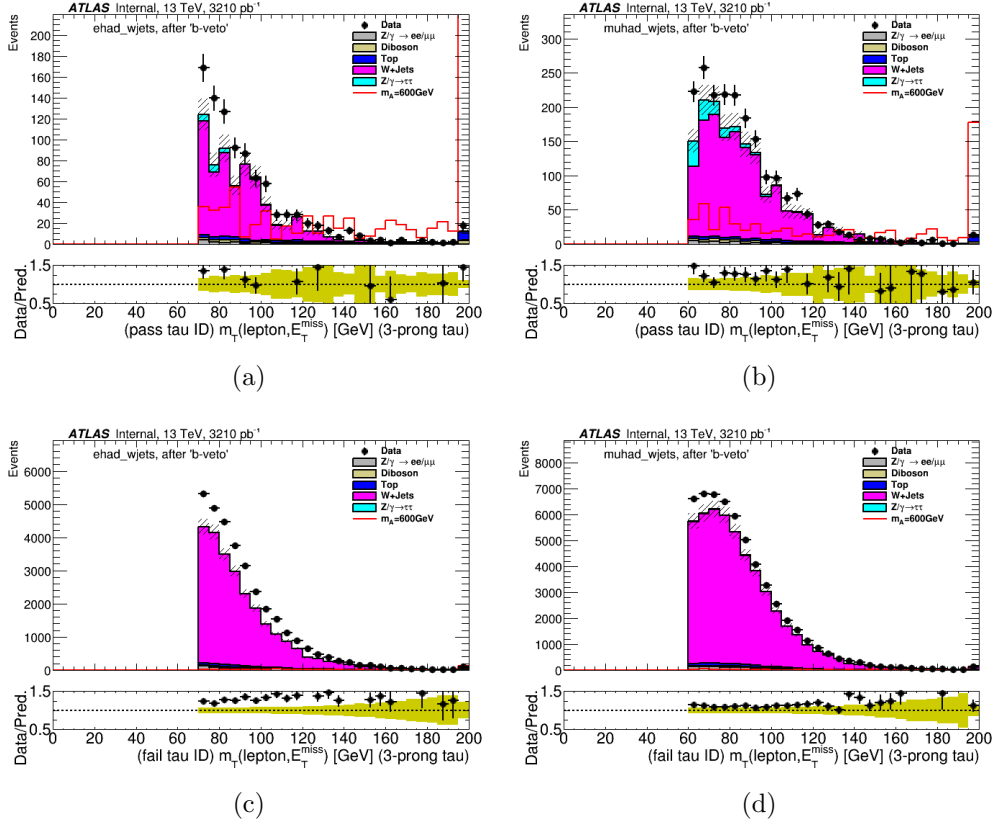


Figure 5.9: Distributions of $m_T(\ell, E_T^{miss})$ for events (a,b) passing and (c,d) failing the τ_{had} identification requirement in the W +jets control region and 3-prong τ_{had} . Only MC samples are shown for the prediction. No multi-jet estimation is included. The signal plotted here is $m_\phi = 600$ GeV, gluon-fusion produced with a cross section times branching ratio of 100 pb.

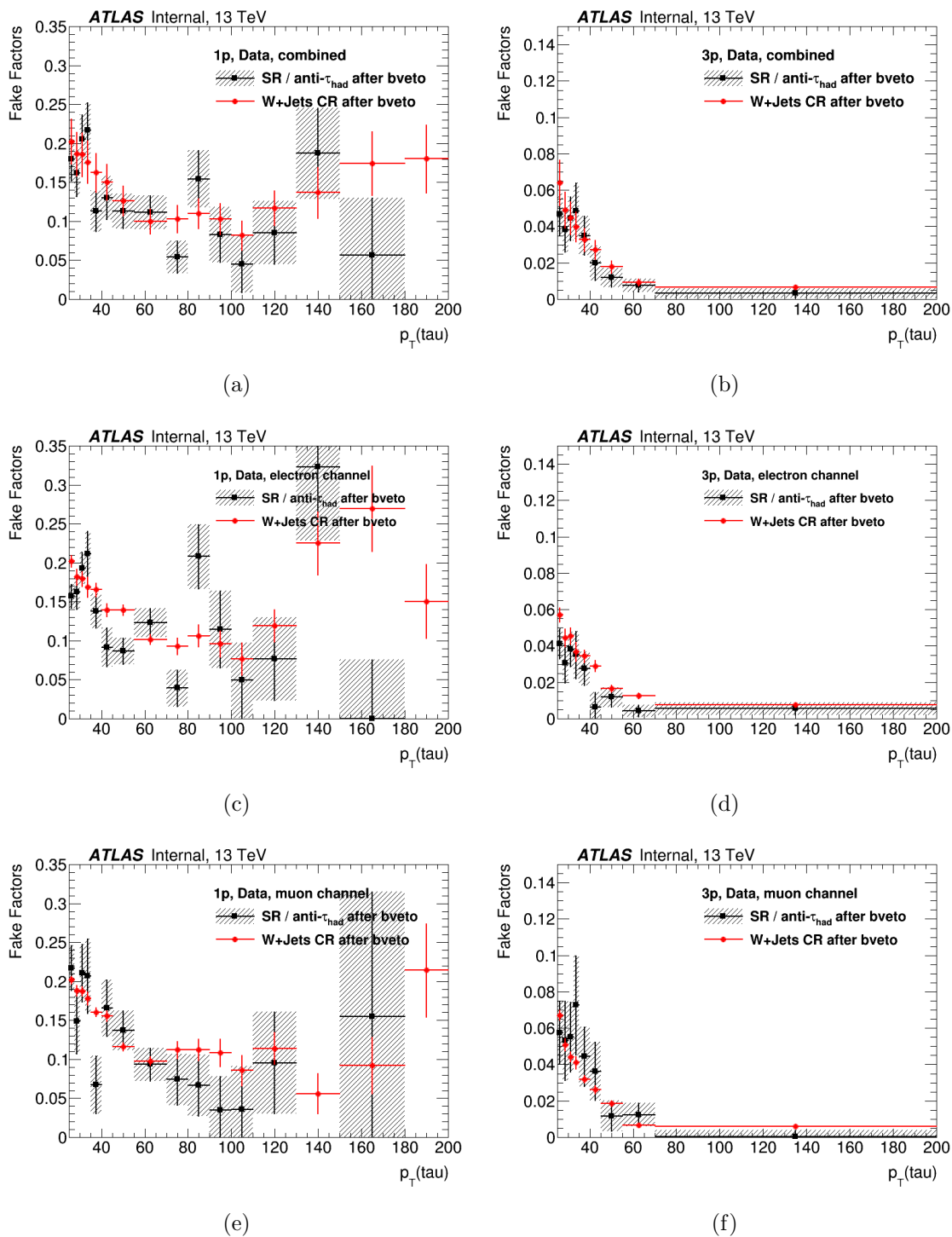


Figure 5.10: Fake factors from the W +jets control region (with b-veto) as a function of $p_T(\tau_{had})$ calculated in data for (a) 1-prong and (b) 3-prong τ_{had} candidates shown with red circular markers. The ratio of the signal region over the anti- τ_{had} region after subtracting the true backgrounds from simulations is shown for comparison. In (c,d) and (e,f) the same plots for the electron and the muon channel, respectively are shown.

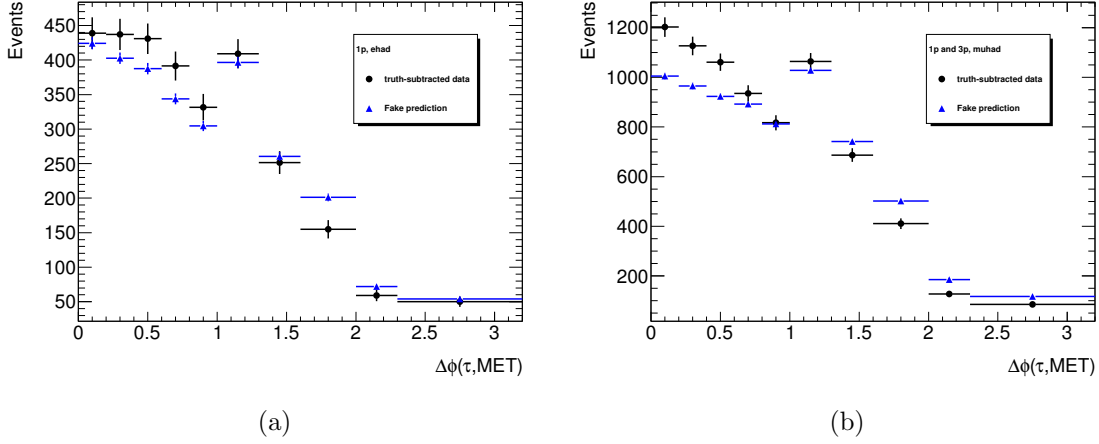


Figure 5.11: Some distributions in the W +jets control region of $\Delta\phi(\tau, E_T^{miss})$ for truth-subtracted data passing τ identification and the prediction of τ fakes from the anti- τ region.

- 1101 • The kinematic differences of the high $m_T(\ell, E_T^{miss})$ (> 60 GeV) W +jets events and
 1102 signal region events ($m_T(\ell, E_T^{miss}) < 40$ GeV) can lead to incorrect assumptions about
 1103 the W +jets misidentification rates in signal region.
- 1104 • Contamination in the W +jets control region from other backgrounds with different
 1105 τ_{had} identification efficiencies will impact the fake factor calculation.
- 1106 • Events failing τ_{had} identification have a different jet composition than events passing
 1107 τ_{had} identification.

1108 The impact of these potential sources of error have been investigated. The three error
 1109 sources above can be correlated. For example, the $m_T(\ell, E_T^{miss})$ cut directly affects the
 1110 amount background contamination. Therefore, effects that are small or overshadowed by
 1111 statistical uncertainties are not propagated to the final uncertainty. Regardless, the high-
 1112 to-low $m_T(\ell, E_T^{miss})$ systematic completely dominates the W +jets fake factor systematic
 1113 uncertainty, so that the choice of which other errors to include has little impact on the final
 1114 systematic.

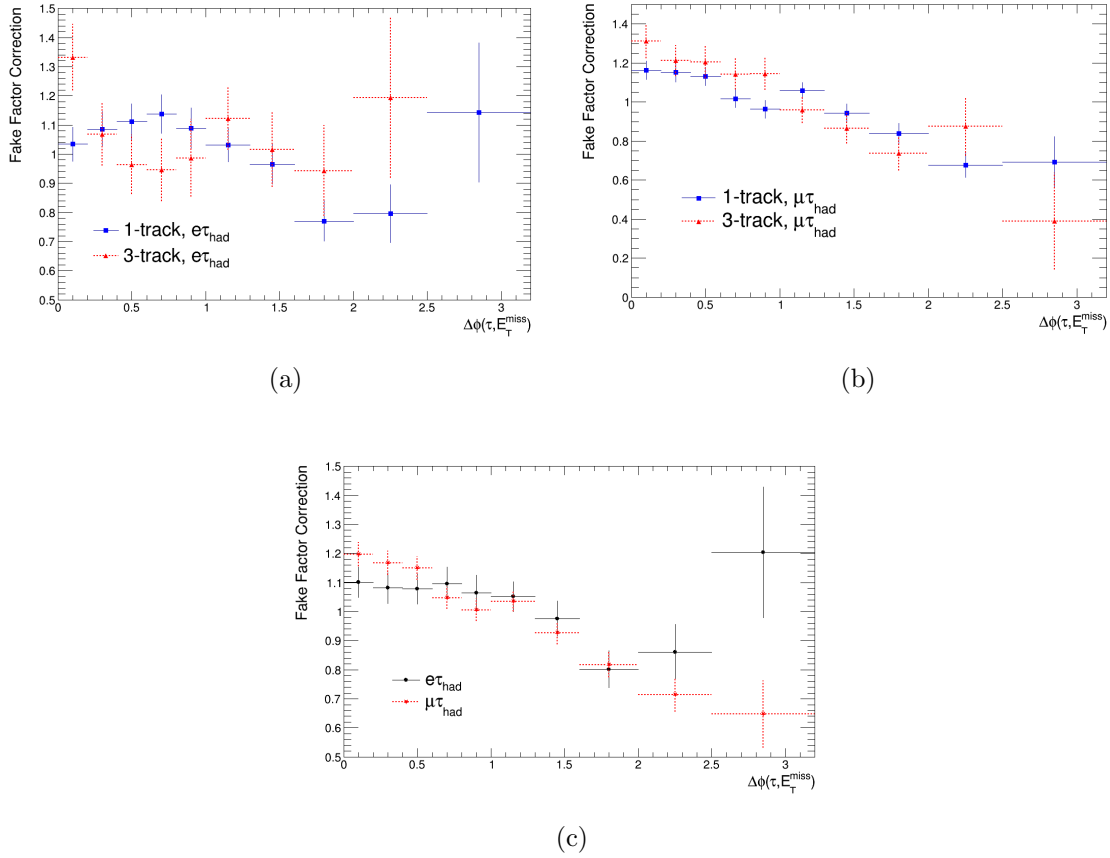


Figure 5.12: Correction scale factors that are applied to the W +jets fake factors as a function of $\Delta\phi(\tau, E_T^{miss})$. The scale factors are shown for the (a) $e\tau_{had}$, (b) $\mu\tau_{had}$ channels and (c) combined channels. ,

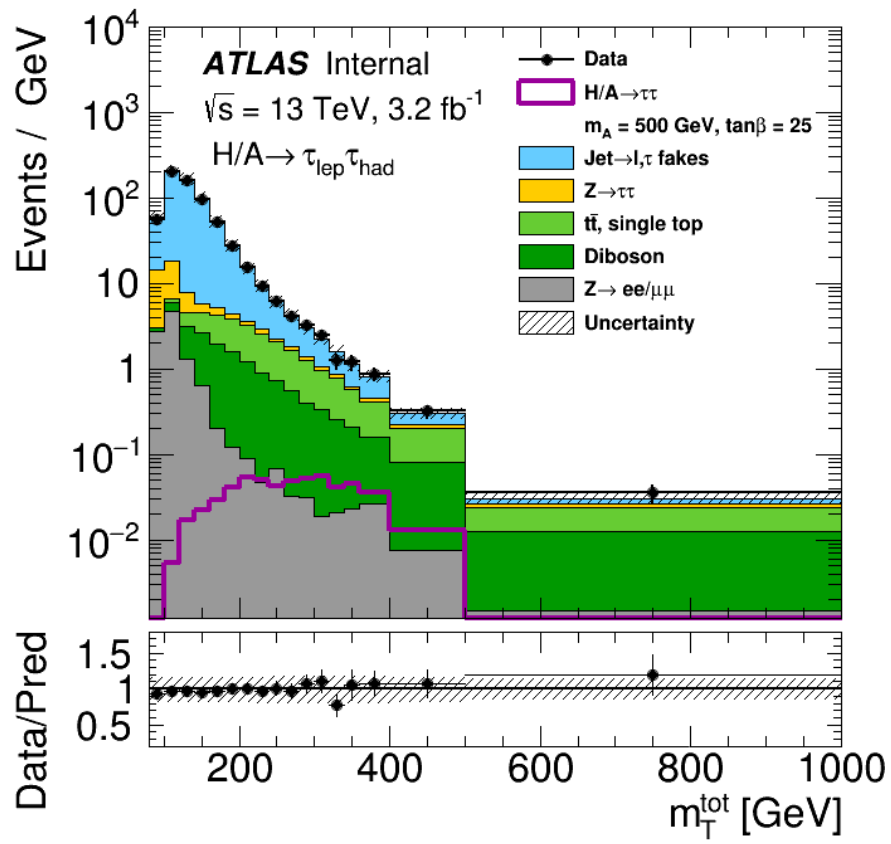


Figure 5.13: Distribution of the total transverse mass in the high $m_T(\ell, E_T^{\text{miss}})$ region for the inclusive $e\tau_{\text{had}} + \mu\tau_{\text{had}}$ channels.

1. Fake rate differences between high and low m_T regions

To be able to distinguish this error source from others such as multi-jet contamination, this systematic is calculated using simulated W +jets MC events. Fake factors computed using Equation 5.3 in the W +jets control region are compared to those in the low- $m_T(\ell, E_T^{miss})$ region. Because of the limited number of simulated W +jets events, the comparison can be done in only three p_T regions. The relative differences between the two sets of fake factors are shown in Table 5.5. For both prongs, a 20% systematic error is assigned from this effect which is the largest source of systematic error in the W +jets fake factor estimation.

Table 5.5: Relative difference between W +jets fake factors computed in the high and low $m_T(\ell, E_T^{miss})$ regions for 1-prong and 3-prong separately

p_T bin [GeV]	1-prong	3-prong
25 – 30	$30\% \pm 5\%$	$15\% \pm 9\%$
30 – 45	$16\% \pm 5\%$	$30\% \pm 9\%$
45 – 200	$21\% \pm 5\%$	$23\% \pm 12\%$

2. Impurity of the W +jets control region

The W +jets control region has some contamination from processes with true leptons and hadronic taus, and from events with electrons faking the τ_{had} . These are subtracted from the W +jets control region according to their simulated predictions in that region. Thus, a 10% uncertainty in the subtraction of simulated events compatible with the systematic uncertainty associated with using such simulated events (as shown in section 5.5) is added to the MC subtraction.

The effect of multi-jet contamination is more difficult to estimate. As will be explained in Section 5.4.4, we cannot use simulated events to model multi-jet processes. This contamination is then estimated from the excess of data compared to the combined MC prediction in the W +jets control region, found to be at most 10% for the fail-TauID region of the $e\tau_{had}$ channel. We then calculate what the impact on the fake factor would be if the entire W +jets

1135 control region had a 10% multi-jet contamination. By scaling the impact of the observed
 1136 differences between the W +jets and multi-jet fake factors (shown below) with this impurity
 1137 fraction, a systematic uncertainty of approximately 3% (1%) is found for 1-prong (3-prong)
 1138 events.

Table 5.6: W +jets b-veto control region composition for 1-prong τ_{had} .

channel	$e\tau_{had}$				$\mu\tau_{had}$			
tau ID	pass		fail		pass		fail	
	inclusive	true τ_{had}	inclusive	true τ_{had}	inclusive	true τ_{had}	inclusive	true τ_{had}
$Z \rightarrow \tau\tau$	99 ± 5	94 ± 5	40 ± 3	31 ± 2	384 ± 15	379 ± 16	150 ± 7	121 ± 6
$Z \rightarrow \ell\ell$	90 ± 5	34 ± 3	416 ± 16	24 ± 2	449 ± 19	166 ± 8	868 ± 28	42 ± 3
Diboson	113 ± 4	97 ± 4	150 ± 5	28 ± 1	149 ± 5	120 ± 4	244 ± 8	34 ± 1
Top	166 ± 6	134 ± 5	40 ± 1	6 ± 0	210 ± 7	156 ± 5	67 ± 2	8 ± 0
W +jets	2262 ± 80	17 ± 3	14338 ± 436	7 ± 2	4979 ± 168	32 ± 5	31395 ± 941	27 ± 5
Data	3312		19579		6535		35741	

1139 3. Anti- τ_{had} jet composition

1140 Events passing the “medium” criteria of the TauID have a minimum BDT score that varies
 1141 in $\tau_{had} p_T$, and is on the order of 0.7 for 1-prong and 0.8 for 3-prong. Events failing τ_{had} -ID
 1142 can have BDT scores as low as 0, and events with very low BDT score have a higher fraction
 1143 of gluon-initiated jets faking the τ_{had} . Because gluon-initiated jets have a different fake rate

Table 5.7: W +jets b-veto control region composition for 3-prong τ_{had} .

channel	$e\tau_{had}$				$\mu\tau_{had}$			
tau ID	pass		fail		pass		fail	
	inclusive	true τ_{had}	inclusive	true τ_{had}	inclusive	true τ_{had}	inclusive	true τ_{had}
$Z \rightarrow \tau\tau$	27 ± 2	27 ± 2	27 ± 2	16 ± 1	122 ± 6	121 ± 6	123 ± 6	78 ± 4
$Z \rightarrow \ell\ell$	12 ± 2	2 ± 1	640 ± 24	21 ± 2	28 ± 2	1 ± 0	1066 ± 33	8 ± 1
Diboson	31 ± 1	26 ± 1	240 ± 10	19 ± 5	43 ± 2	33 ± 1	399 ± 13	32 ± 1
Top	45 ± 2	37 ± 2	12 ± 0	1 ± 0	58 ± 2	43 ± 2	23 ± 1	1 ± 0
W +jets	542 ± 26	3 ± 1	23501 ± 734	35 ± 5	1357 ± 57	8 ± 2	47336 ± 1368	56 ± 7
Data	937		32192		1997		55798	

1144 compared to quark-initiated jets, a minimum BDT score of 0.35 is chosen so that the jet
 1145 composition in the anti- τ_{had} region more closely resembles the one found in the signal region.
 1146 An estimate of how much impact the jet composition can have in the W +jets fake factors
 1147 is obtained by varying the lower BDT score cut. Changing the cut to 0.45 and recomputing
 1148 the data-driven W +jets prediction indicates that this systematic error is approximately 5%
 1149 for the $e\tau_{had}$ channel and 1% for the $\mu\tau_{had}$ channel.

1150 5.4.4 Background with misidentified lepton and tau

1151 The majority of events with misidentified lepton and tau are from multi-jet background.
 1152 The good light lepton identification in ATLAS ensures a low jet-to- ℓ fake rate, causing the
 1153 acceptance efficiency of multi-jet events in our signal region is very low. However, because
 1154 the LHC is a proton-proton collider, the production rate of multi-jet events is extremely high,
 1155 which causes multi-jet processes to still have an important contribution to the background
 1156 in our signal region. It is not computationally feasible to generate enough MC events to
 1157 reproduce these two opposing effects, so a data-driven estimation of multi-jet is required.
 1158 Furthermore, as mentioned before, the jet-to- τ_{had} fake rate and the shower properties of τ_{had}
 1159 fakes are not always modelled well. For these reasons, a data-driven estimate of the multi-jet
 1160 background is necessary.

1161 The estimation method chosen for multi-jet background is similar to that for W +jets,
 1162 using $p_{T,\tau_{had}}$ and prong-dependent fake factors calculated in a multi-jet control region using
 1163 the TauID identification ratio (as shown in Equation 5.3). The multi-jet control region
 1164 is obtained by inverting the isolation requirement of the light lepton (i.e. by defining an
 1165 anti-isolated control region). The main sources of systematic uncertainties are:

- 1166 • The uncertainties on the MC subtraction of events with true objects. This is conserva-
 1167 tively estimated by varying the number of subtracted events by 50% and checking the
 1168 impact on the fake factors. Due to the very low presence of events with true leptons
 1169 in the anti-isolated control region, this systematic is negligible.

- Biases in the τ_{had} ID efficiency from the anti-isolation requirement. This is estimated by comparing the fake factors in the multi-jet control region with those in the isolated region. To ensure orthogonality with the signal region, the lepton and τ_{had} are required to have same signed charge. The differences between the two sets of fake factors is used as a systematic uncertainty.
- A $\Delta\phi$ correction similar to that applied for W +jets is used and a constant 15% uncertainty is applied to the scale factors (again due to the subtraction of simulated events).

The final multi-jet fake factors are shown in Figure 5.14.

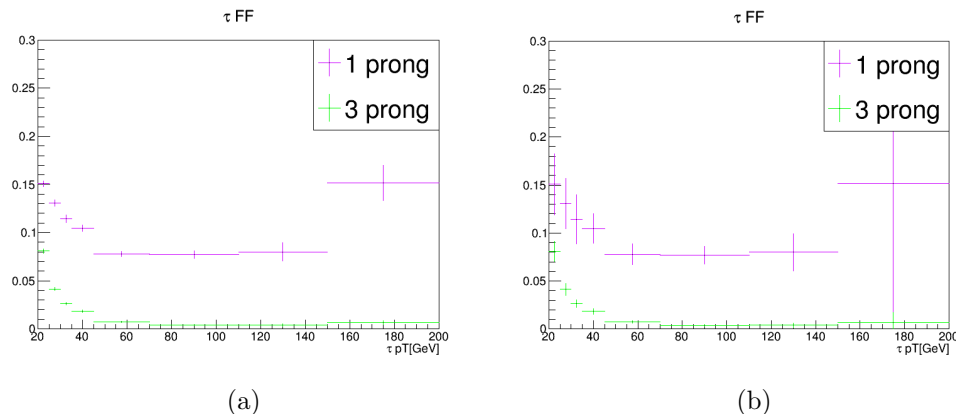


Figure 5.14: Fake factors for jets from multi-jet events misidentified as τ_{had} . Fake factors are shown as a function of p_T , for 1-prong and 3-prong τ , with (left) statistical uncertainty only and (right) all statistical and systematic uncertainties with the exception of the uncertainty on the denominator definition (evaluated by varying the jet BDT cut).

1179 5.4.5 Combined Fake-Factor Method

1180 The W +jets and multi-jet fake factors are defined as the pass/fail identification ratio of the
 1181 medium TauID working point. Therefore, they must be multiplied with events that pass all
 1182 selection requirements apart from the medium TauID cut. The category made up of such

1183 events will be referred to as the anti- τ_{had} region. Because the W +jets and QCD fake factors
 1184 are to be applied to data events in the anti- τ_{had} region, for which truth-level information is
 1185 obviously unavailable, an immediate concern is how to separate which events corresponds
 1186 to W +jets background and which correspond to multi-jet. Since the anti- τ_{had} region has
 1187 a large number of events, a nearly perfect approximation is to, instead of separating the
 1188 to-be-weighted events by their processes, combine the fake factors according to the relative
 1189 fraction of each background into a “combined fake factor”. The new combined fake factor is
 1190 defined below:

$$FF(\text{comb}) = FF(W + \text{jets}) \times r_W + FF(\text{QCD}) \times r_{\text{QCD}}, \quad (5.4)$$

1191 where r_{QCD} is the multi-jet fraction of data events in the anti- τ_{had} region after subtraction
 1192 of events with true objects and $r_W \equiv 1 - r_{\text{QCD}}$.

1193 *Predicting the multi-jet fraction*

1194 In terms of their object signatures, the main difference between multi-jet and W +jets is that
 1195 in the former the light lepton is a misidentified jet whilst the latter is a true object from the
 1196 W decay. To predict the jet-to- ℓ misidentification rate in the anti- τ_{had} region, a lepton fake
 1197 factor method is defined using the lepton isolation efficiency, as shown below:

$$FF = \frac{N(\text{pass “gradient” lepton isolation})}{N(\text{fail “gradient” lepton isolation})} \quad (5.5)$$

1198 They are calculated in a “fake-lepton control region” defined with the following selection:

- 1199 • Same single lepton triggers as signal region.
- 1200 • Exactly one lepton. No isolation is required since this is the criteria to define the fake
 1201 factors.
- 1202 • At least one jet.
- 1203 • No events with at least one τ_{had} passing “loose” identification.

- 1204 • $M_T(\ell, E_T^{miss}) < 30$ GeV.

1205 The event selection is designed to minimize the contamination of true leptons without dra-
 1206 matically reducing the number of multi-jet events. The cuts on the transverse mass and
 1207 number of jets are efficient both in rejecting W +jets events and bringing the selection closer
 1208 to the signal region selection. The number of jets per event and distributions of the trans-
 1209 verse mass can be found in Figures 5.15-5.16. The sample composition of the lepton fake
 1210 factor control region is shown in Table 5.8.

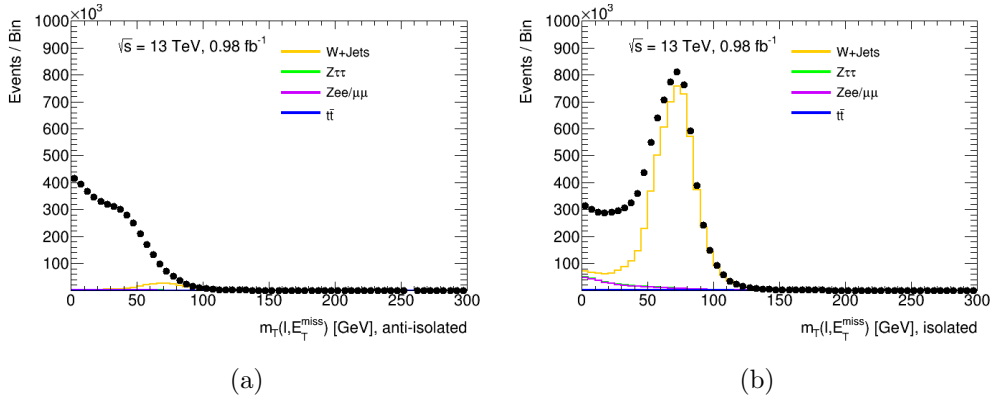


Figure 5.15: The transverse mass of the lepton and missing transverse momentum in the fake lepton region for e and μ channels combined, (a) with the anti-isolation applied and (b) with the isolation requirement applied, but without the cuts on jet multiplicity and transverse mass applied.

1211 The lepton fake factors are parameterized as a function of lepton η , shown in Figure
 1212 5.17. For the $\mu\tau_{had}$ channel, there are two sets of fake factors used for events with lepton
 1213 transverse momentum above or below 55 GeV. The multi-jet fraction in the anti- τ_{had} region
 1214 is obtained by applying these fake factors to data events in the anti-isolated anti- τ_{had} region.
 1215 The multi-jet fraction of the anti- τ_{had} region (r_{QCD} term of Equation 5.4) is then given by:

$$r_{QCD} = \frac{N_{QCD}}{N_{data} - N_{true MC}} \quad (5.6)$$

1216 where N_{QCD} is the number of multi-jet events estimated with the lepton fake factors, N_{data}

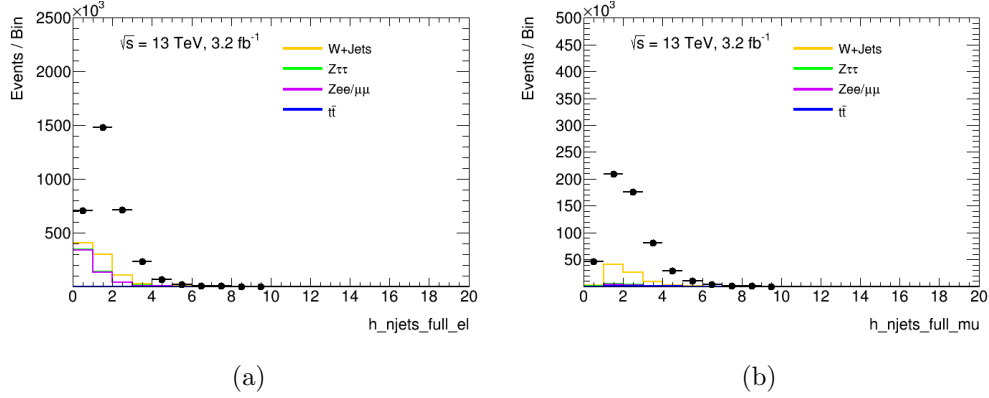


Figure 5.16: The number of jets in the fake lepton region for the $e\tau_{had}$ (a) and $\mu\tau_{had}$ (b) channels with no requirement on the lepton isolation.

Table 5.8: Events in the fake lepton region. The numbers correspond to an integrated luminosity of 3.2 fb^{-1} . The quoted uncertainties are due to the finite number of generated events in the simulated samples.

Backgrounds	μ -channel b -veto	e -channel b -veto
W +jets	67700 ± 900	244500 ± 1700
$Z \rightarrow \tau\tau$ +jets	4340 ± 110	10700 ± 180
Top	1366 ± 27	3020 ± 40
$Z \rightarrow \ell\ell$ +jets	5130 ± 120	174700 ± 700
Total non-multi-jet background	78500 ± 900	433000 ± 1900
Data	507760	2511210
ggH, $m_A = 350 \text{ GeV}$, 1pb	8.3 ± 0.6	15.9 ± 0.8
ggH, $m_A = 1500 \text{ GeV}$, 1pb	5.9 ± 0.5	8.4 ± 0.6

1217 the number of events observed in data, and $N_{\text{true MC}}$ the number of simulated events with
 1218 truth-matched leptons and taus.

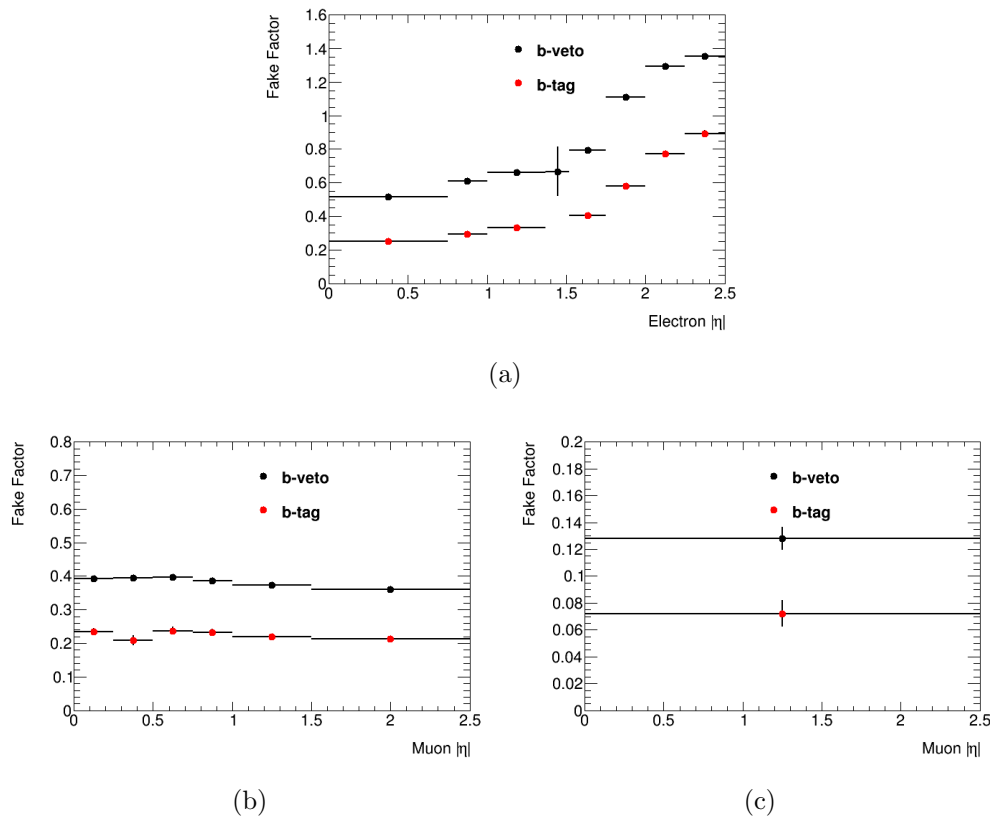


Figure 5.17: Fake factors from the fake lepton control region as a function of lepton η for (a) electrons, (b) muons with $p_T < 55$ GeV and (c) muons with $p_T > 55$ GeV.

1219 The r_{QCD} fraction is parameterized as a function of $\tau_{\text{had}} p_T$, as shown in Figure 5.18. The
 1220 uncertainties considered in the r_{QCD} parameterization include:

- 1221 • Statistical uncertainty on the lepton fake factor, corresponding to less than 1%.
- 1222 • Systematic uncertainty from true lepton contamination of the lepton fake factor control
 1223 region, corresponding to approximately 9% and 12% in the $e\tau_{\text{had}}$ and $\mu\tau_{\text{had}}$ channels,
 1224 respectively.

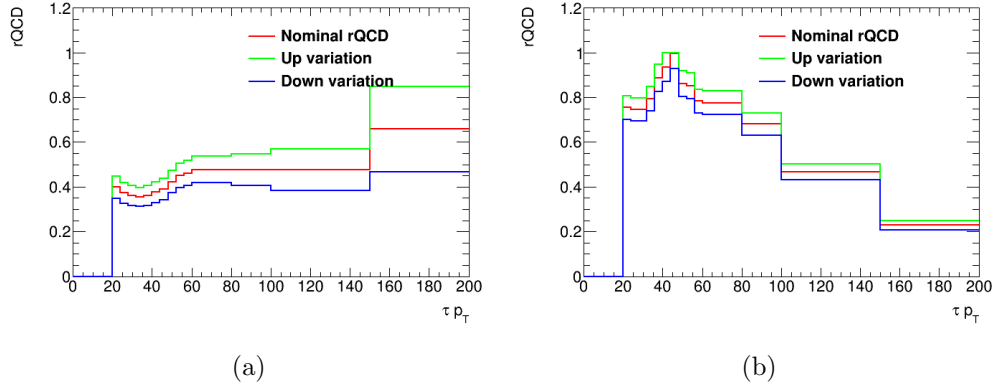


Figure 5.18: The trend of r_{QCD} as a function of τp_T at the end of the event selection, along with the total up and down shifts for the uncertainties, shown separately for (left) the muon and (right) the electron channels.

- 1225 • Statistical uncertainty in the anti- τ_{had} region, roughly 1%.
- 1226 • Systematic uncertainty from varying the transverse mass cut in the lepton fake factor
- 1227 control region definition, approximately 4% in the electron channel but only 0.7% in
- 1228 the muon channel.

1229 Similar to the multi-jet and W +jets fake factors, the lepton fake factors are subjected
 1230 to a closure test of their performance. Some disagreement between predicted and observed
 1231 events is observed in the $\Delta\phi(\ell, E_T^{miss})$ distribution, as can be seen in Figure 5.19. Thus,
 1232 $\Delta\phi(\ell, E_T^{miss})$ -dependent correction scale factors are derived. A systematic uncertainty of
 1233 10% is incorporated due to the subtraction of truth-matched MC events.

1234 With the multi-jet estimate (r_{QCD}) from the lepton fake factor method and the W +jets
 1235 and multi-jet fake factors, the combined fake factor of Equation 5.4 can be calculated. The
 1236 final prediction of the background with misidentified leptons and/or hadronic taus for several
 1237 kinematic variables is shown in Figures 5.20-5.21. A last set of shape systematics is considered
 1238 for the final misidentified background prediction where the W +jets fake factors, multi-jet
 1239 fake factors and r_{QCD} are separately varied by one standard deviation of their respective

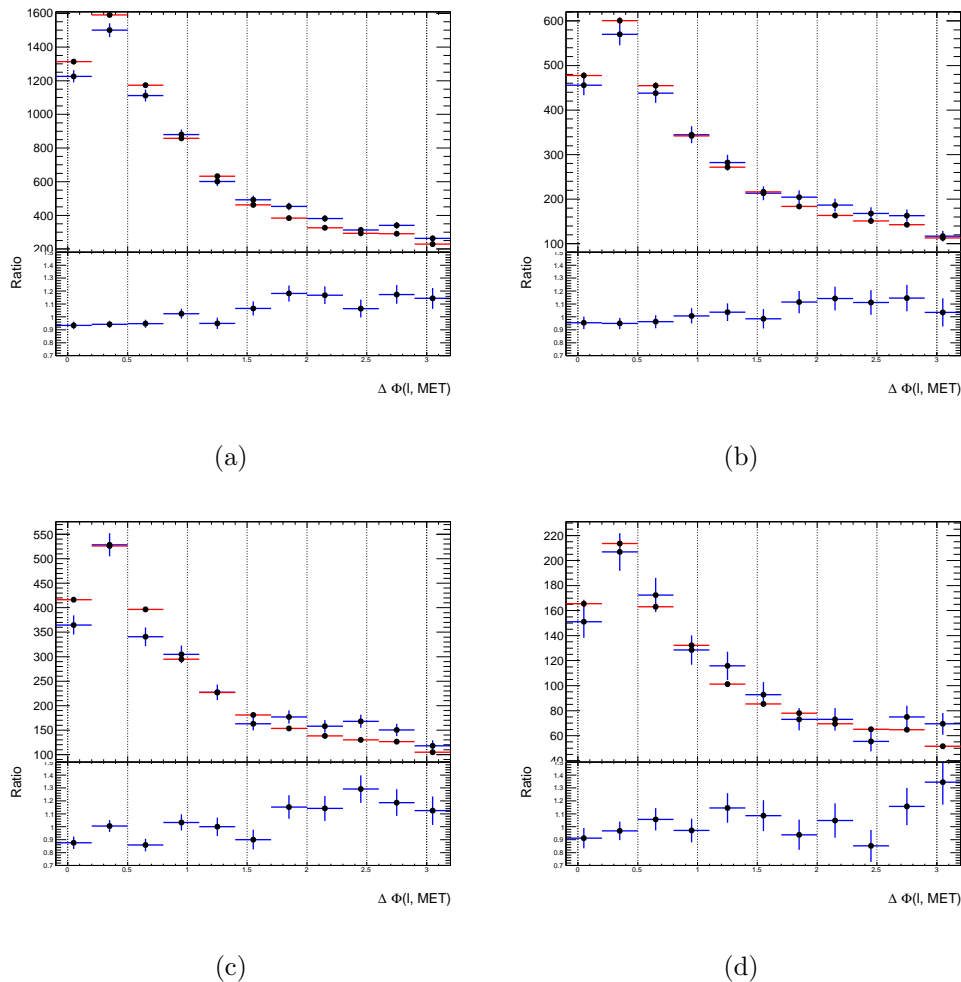


Figure 5.19: $\Delta\Phi(l, MET)$ distribution in (a) ehad 1 prong, (b) muHad 1 prong, (c) ehad 3 prong, (d) muhad 3 prong: The blue curve are the events passing TauID selection in the anti-lepton-isolation region. The red one there is for events that failed TauID but weighted with the fake factor.

1240 uncertainties. Since the W +jets and multi-jet are not different between the $e\mathcal{T}_{had}$ and $\mu\mathcal{T}_{had}$
 1241 channels, they are treated as correlated between the channels. The r_{QCD} fraction however is
 1242 treated uncorrelated since it is separately derived for each lepton channel.

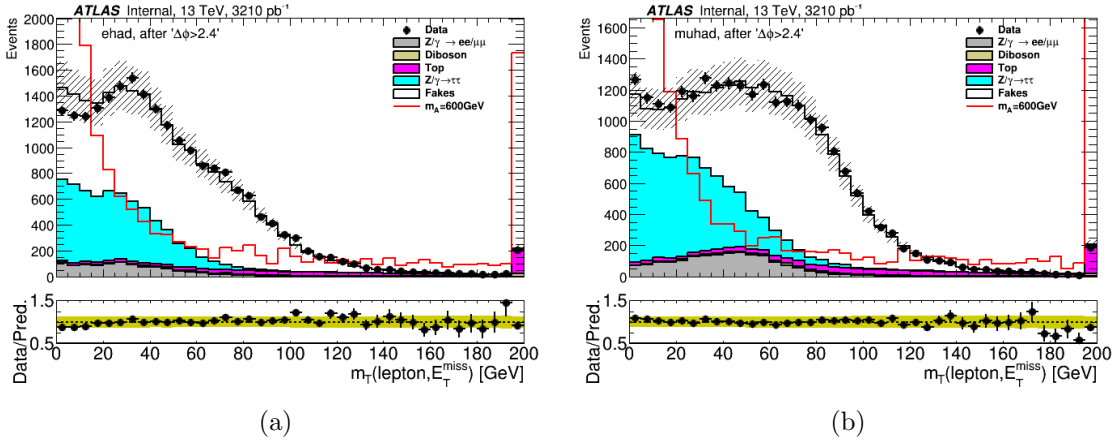


Figure 5.20: The transverse mass between the lepton and the E_T^{miss} before the $m_T(\ell, E_T^{miss})$ requirement for the electron (a) and the muon (b) channel.

1243 5.5 Systematic Uncertainties

1244 This section describes the systematic uncertainties pertinent to the use of simulated samples.
 1245 A description of systematic uncertainties for data-driven background predictions can be found
 1246 in Section 5.4.

1247 5.5.1 Luminosity and cross section uncertainties

1248 There is a 5% uncertainty on the the integrated luminosity measurement which should be
 1249 applied to any event taken from simulation. In the case of this analysis, these correspond to
 1250 events with truth-matched lepton and hadronic tau. The main backgrounds affected by this
 1251 uncertainty are $Z \rightarrow \tau\tau$ and $t\bar{t}$. The production cross-sections used to scale the simulated
 1252 events also have theoretical uncertainties. The most important simulated background sam-

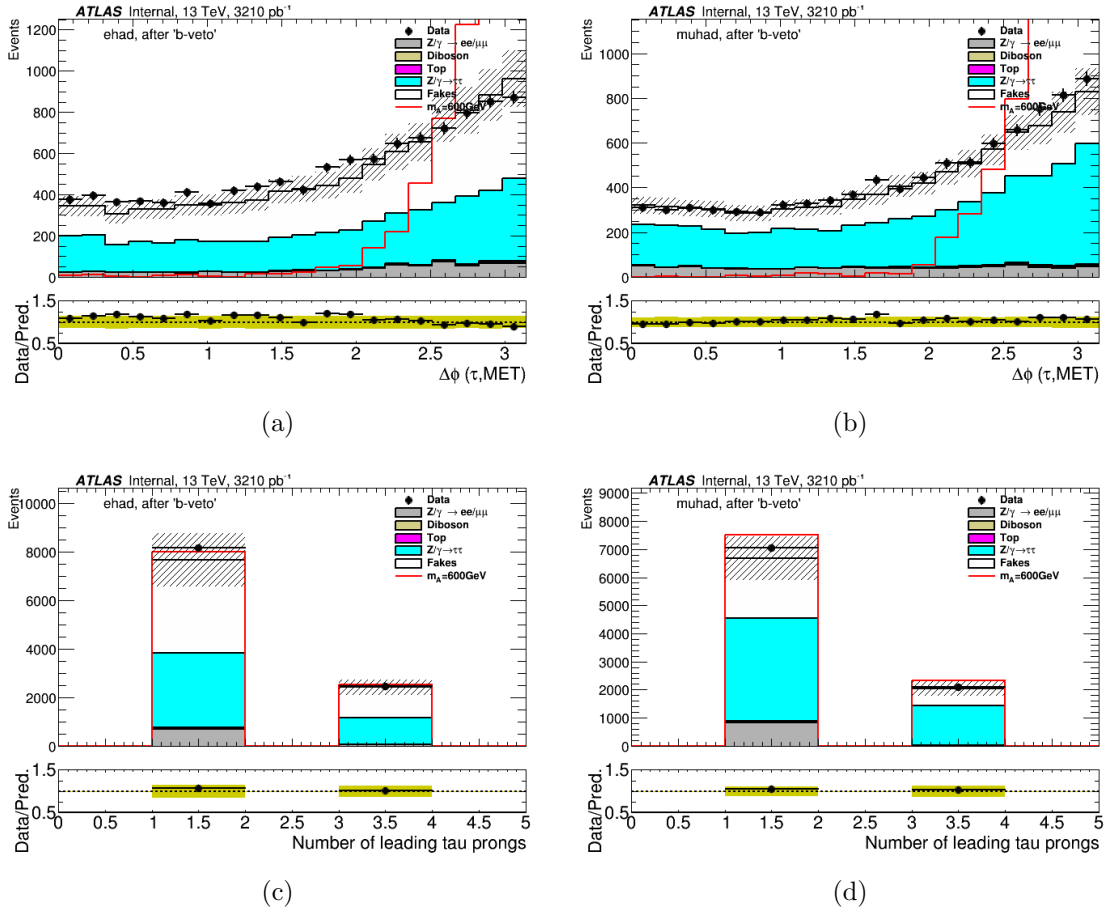


Figure 5.21: The distributions of $\Delta\phi(\tau_{had}, E_T^{miss})$ (a,b) and number of tau tracks (c,d) for the full selection in the $e\tau_{had}$ and $\mu\tau_{had}$ channels.

1253 ples used in this analysis are $Z \rightarrow \tau\tau$ and diboson, which carry uncertainties of 5% and 6%,
 1254 respectively.

1255 5.5.2 Detector-related uncertainties

1256 The simulated detector response and software performance in Monte Carlo generated events
 1257 has several systematic uncertainties. They can be due to:

- 1258 • The reconstruction and identification of τ_{had} (Tau reco/ID).
- 1259 • The reconstruction of the energy of the τ_{had} , also referred to as the τ_{had} energy scale
 1260 (Tau e-scale).
- 1261 • The efficiencies of muon triggers, as well as the subsequent reconstruction, isolation,
 1262 identification and energy scale of simulated muons (“Muon”).
- 1263 • The efficiencies of electron triggers, as well as the subsequent reconstruction, isolation,
 1264 identification and energy scale of simulated electrons (“Electron”).
- 1265 • Uncertainties in the E_T^{miss} calculation for simulated events (“MET”).
- 1266 • Jet energy scale and resolution (“Jet”).
- 1267 • The flavor-tagging algorithm efficiency (“ b -tagging”).
- 1268 • The simplified simulation used for b -associated production signal samples, which use
 1269 ALTFast II (“AF2”).
- 1270 • Pile-up uncertainties due to the reweighting of MC samples to match the average
 1271 interaction per bunch crossing ($\langle\mu\rangle$) profile of data events (“Pile-up”).

1272 The uncertainties are computed separately for the $e\tau_{had}$ and $\mu\tau_{had}$ channels, and a summary
 1273 can be found in Tables 5.9-5.12.

Table 5.9: The effect of the systematic uncertainties in the MC samples used for the background estimation for the $e\tau_{had}$, b -veto category. The effect on the normalization in % is shown per sample.

Electron channel, backgrounds, b-veto				
Systematic	$Z \rightarrow \ell\ell$	Top	$Z \rightarrow \tau\tau$	Diboson
Muon	0.00	0.11	0.00	0.06
Electron	1.99	1.48	1.27	1.43
Tau reco/ID	0.03	10.43	10.81	10.09
Tau e-scale	0.00	5.75	2.22	5.21
Jet	2.58	5.23	2.51	1.79
MET	1.35	1.13	0.67	0.89
b-tagging	0.02	6.53	0.03	0.01
Pile-up	1.91	3.13	3.30	2.88

Table 5.10: The effect of the systematic uncertainties in the MC samples used for the background estimation for the $\mu\tau_{had}$, b -veto category. The effect on the normalization in % is shown per sample.

Muon channel, backgrounds, b-veto				
Systematic	$Z \rightarrow \ell\ell$	Top	$Z \rightarrow \tau\tau$	Diboson
Muon	0.96	2.42	1.25	1.83
Electron	0.00	0.00	0.01	0.11
Tau reco/ID	0.00	10.84	11.06	10.71
Tau e-scale	0.00	5.53	4.51	5.88
Jet	3.17	5.00	2.97	3.76
MET	3.23	0.57	0.86	1.20
b-tagging	0.07	6.26	0.03	0.01
Pile-up	0.96	2.98	2.43	2.24

Table 5.11: The effect of the systematic uncertainties in the MC samples used signal events in the $e\tau_{had}$, b -veto category. The effect on the normalization in % is shown per sample.

Electron channel, signal, gluon fusion, b-veto category						
Systematic	ggH200	ggH300	ggH400	ggH500	ggH800	ggH1000
Electron	0.94	1.22	0.99	1.14	1.51	1.74
Tau reco/ID	11.32	9.05	7.84	7.43	7.99	8.66
Tau e-scale	8.55	5.43	5.07	4.27	4.27	3.27
Jet	2.75	3.21	1.87	2.07	1.95	2.07
MET	1.22	1.23	0.51	0.61	0.51	1.09
b-tagging	0.02	0.05	0.03	0.03	0.04	0.04
Pile-up	2.17	5.61	1.42	3.71	0.78	5.10
Electron channel, signal, b-associated production, b-veto category						
Systematic	bbH200	bbH300	bbH400	bbH500	bbH800	bbH1000
Muon	0.04	0.04	0.04	0.06	0.04	0.03
Electron	1.37	1.13	1.30	1.47	1.85	2.01
Tau reco/ID	11.39	8.90	8.10	7.36	7.96	8.60
Tau e-scale	5.62	5.17	4.42	3.70	4.04	0.93
Jet	3.13	2.15	2.06	2.28	1.86	2.26
MET	1.90	0.50	0.40	0.57	0.60	0.48
AF2	3.69	2.48	2.35	2.22	2.19	2.17
b-tagging	1.64	1.83	1.81	1.79	1.82	1.73
Pile-up	1.22	3.31	1.99	0.66	1.86	0.90

Table 5.12: The effect of the systematic uncertainties in the MC samples used for signal events in the $\mu\tau_{had}$, b -veto category. The effect on the normalization in % is shown per sample.

Muon channel, signal, gluon fusion, b-veto category						
Systematic	ggH200	ggH300	ggH400	ggH500	ggH800	ggH1000
Muon	1.84	2.31	2.70	2.83	3.13	3.32
Electron	0.00	0.00	0.00	0.00	0.00	0.00
Tau reco/ID	12.00	9.38	8.12	7.58	7.96	8.67
Tau e-scale	2.73	3.58	4.25	4.11	4.15	3.55
Jet	2.22	2.71	2.43	2.13	2.59	2.31
MET	0.56	0.60	1.06	0.55	0.57	0.58
b-tagging	0.03	0.05	0.04	0.04	0.06	0.05
Pile-up	0.88	1.69	0.63	1.33	3.40	3.96
Muon channel, signal, b-associated production, b-veto category						
Systematic	bbH200	bbH300	bbH400	bbH500	bbH800	bbH1000
Muon	1.79	2.46	2.71	2.99	3.23	3.38
Electron	0.06	0.09	0.05	0.02	0.04	0.03
Tau reco/ID	11.85	9.20	8.28	7.43	7.86	8.49
Tau e-scale	3.22	4.07	4.22	4.40	5.01	2.71
Jet	4.06	2.41	2.59	3.37	2.29	2.93
MET	0.78	1.12	0.56	0.46	0.65	0.57
AF2	2.91	2.57	2.49	2.43	2.22	2.20
b-tagging	1.50	1.73	1.76	1.81	1.96	1.84
Pile-up	0.81	2.25	0.26	2.62	4.16	2.52

1274 *5.5.3 Signal modelling uncertainties*

1275 Similarly to the $A \rightarrow Zh \rightarrow \ell\ell\tau\tau$ search, mismodelling in the simulated acceptance of our
 1276 signal events is accounted for as an uncertainty on the normalization of our signal samples.
 1277 The different MC tunes used to gauge the effect of incorrect event generation are described
 1278 in Ref. [65] and [66] for gluon fusion and b -associated production, respectively. The final
 1279 uncertainties differ for each signal mass hypothesis and are symmetrized according to their
 1280 highest values. The implementation of the uncertainties is done as a linear m_A -dependent
 1281 function:

1282 • $10.367 \times 10^{-5}m_A + 0.18065$, for b -associated production

1283 • $-2.908 \times 10^{-5}m_A + 0.1845$, for gluon fusion production

1284 where the mass of the Higgs boson, m_A , is given in units of GeV. Tables 5.13-5.14 show the
 1285 final signal modelling uncertainties.

Table 5.13: Summary of uncertainties of ggH lephad signal samples in bveto category.

Mass	1-	1+	2-	2+	renormMultFac do	renormMultFac up	pT0Ref do	pT0Ref up	scale	PDF	Total
200GeV	2.4%	0.8%	0.3%	0.5%	2.5%	1.8%	1.7%	2.5%	17.4%	4.1%	18.3%
500GeV	0.3%	2.2%	0.4%	0.1%	1.6%	0.9%	0.5%	0.5%	15.5%	4.8%	16.3%
1000GeV	1.1%	0.9%	1.1%	0.5%	1.6%	0.3%	1.1%	1.0%	15.1%	4.3%	15.8 %

Table 5.14: Summary of uncertainties of bbH lephad signal samples in bveto category.

Mass	1	2	3	combine tune variation	scale	PDF	Total
200 GeV	4.429%	3.698%	0.950%	5.848%	19.088%	5.756%	20.777%
500 GeV	5.888%	0.760%	3.055%	6.677%	20.182%	6.494%	22.228%
1000 GeV	1.069%	0.591%	0.666%	1.391%	25.719%	12.922%	28.816%

1286 **5.6 Results**

1287 The final distribution of the m_T^{tot} discriminant for the observed data is in good agreement
 1288 with the predicted background, as can be seen in Figure 5.22. Additional kinematic distri-
 1289 butions for the $e\tau_{had}$ and $\mu\tau_{had}$ channels are shown in Figures 5.23 and 5.24. The uncertainty
 1290 band includes both statistical and systematic uncertainty, with their likelihood-fit values, as
 1291 described in Appendix B.

1292 The results from the $e\tau_{had}$ and $\mu\tau_{had}$ b -veto categories are combined to improve the
 1293 sensitivity. As in the $A \rightarrow Zh$ analysis, the parameter of interest in the search is the signal
 1294 strength μ given by the ratio of the fitted signal production cross section to its counterpart
 1295 value predicted by the MSSM signal assumption. Upper limits on the cross section times
 1296 branching ratio of general heavy neutral Higgs bosons are set for both gluon-fusion and b -
 1297 associated production at 95% confidence-level. Figure 5.25 shows $\sigma \times BR$ limits for the
 1298 combined $e\tau_{had} + \mu\tau_{had}$ search. Separate limits for each Higgs lepton channel can be found
 1299 in Figure 5.26. The results are interpreted in the m_h^{mod+} scenario [25], and points in the
 1300 $m_A - \tan \beta$ plane with signal hypotheses incompatible the previously calculated cross section
 1301 upper limits are excluded.

1302 A search for neutral MSSM Higgs bosons decaying to tau pairs has already been conducted
 1303 in ATLAS using 8 TeV Run-1 data [67]. The search of $H/A \rightarrow \tau_{lep}\tau_{had}$ search presented here
 1304 aims for a public result that includes the $\tau_{had}\tau_{had}$ decay channel, and events with and without
 1305 b -tagged jets. The combined Run-2 analysis is more sensitive than the Run-1 analysis in the
 1306 entire mass range being considered (see Figure 5.28). An early Run-2 result without b -tagging
 1307 has already been made public [68].

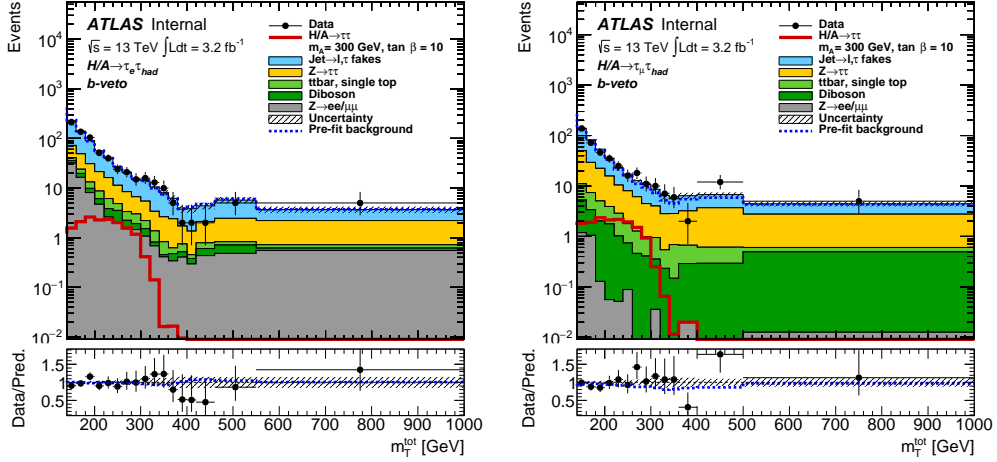
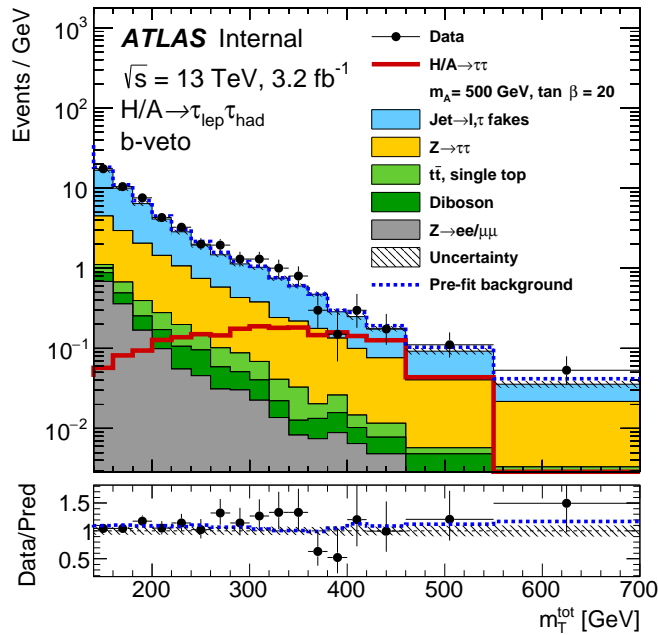
(a) $e\tau_{had}$ (b) $\mu\tau_{had}$ (c) $e\tau_{had} + \mu\tau_{had}$

Figure 5.22: Final distributions of the total transverse mass for $e\tau_{had}$ (a), $\mu\tau_{had}$ (b) and inclusive (c) categories.

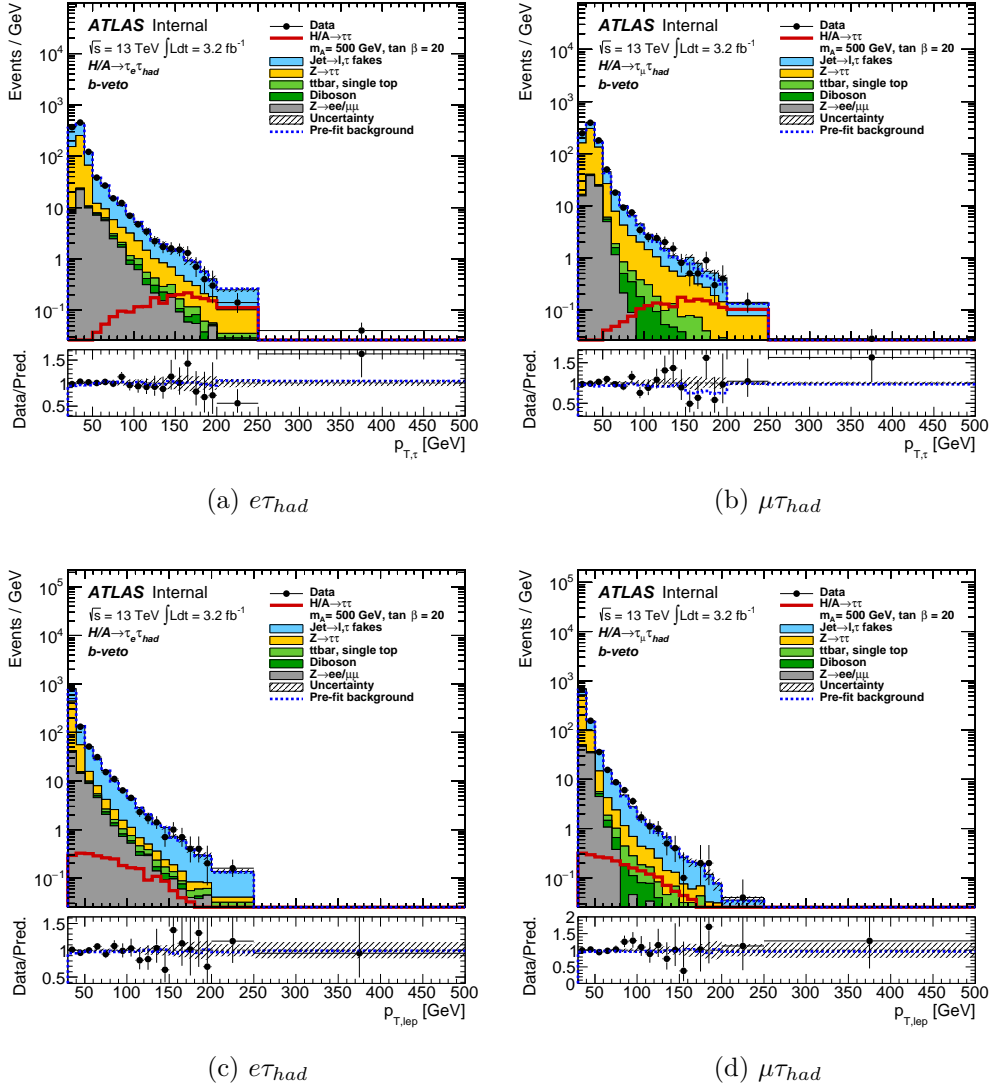


Figure 5.23: Distributions in the electron and muon channels of the $\tau_{had}p_T$, lepton p_T , E_T^{miss} and visible mass. The background predictions and uncertainties used are from the likelihood fit result (see Appendix B).

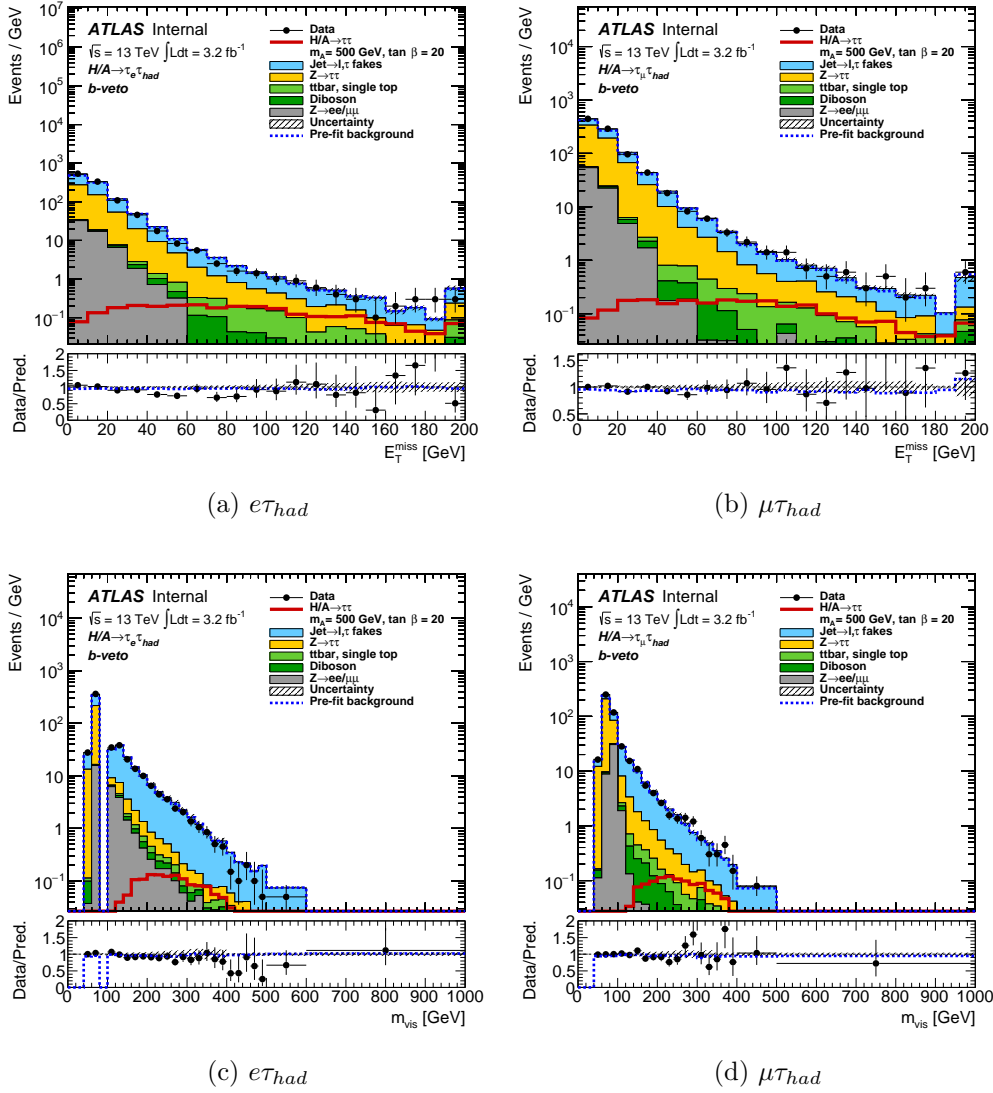
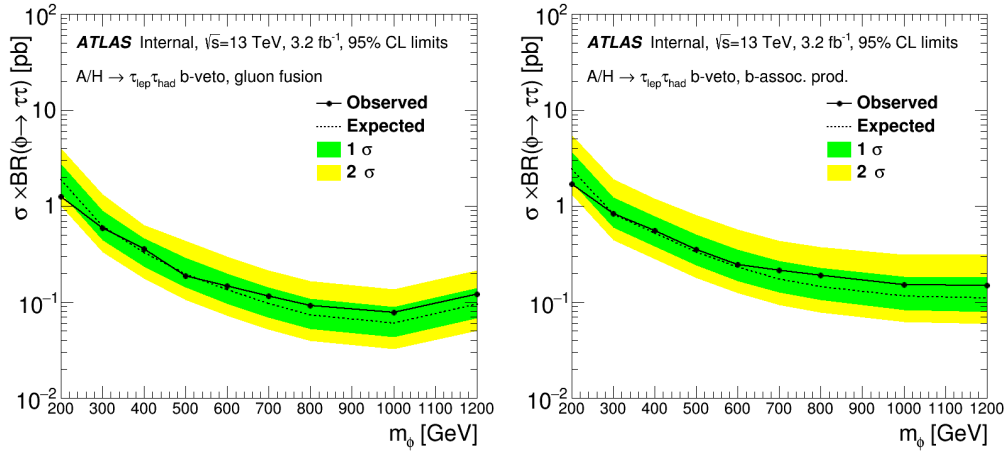


Figure 5.24: Distributions in the electron and muon channels of the $\tau_{had}p_T$, lepton p_T , E_T^{miss} and visible mass. The background predictions and uncertainties used are from the likelihood fit result (see Appendix B).



(a) b-veto, gluon fusion

(b) b-veto, b-associated production

Figure 5.25: The 95% CL upper limit on the production times branching ratio to $\tau\tau$ of a single scalar boson produced via gluon fusion or b-associated production for 3210 pb^{-1} of integrated luminosity at 13 TeV.

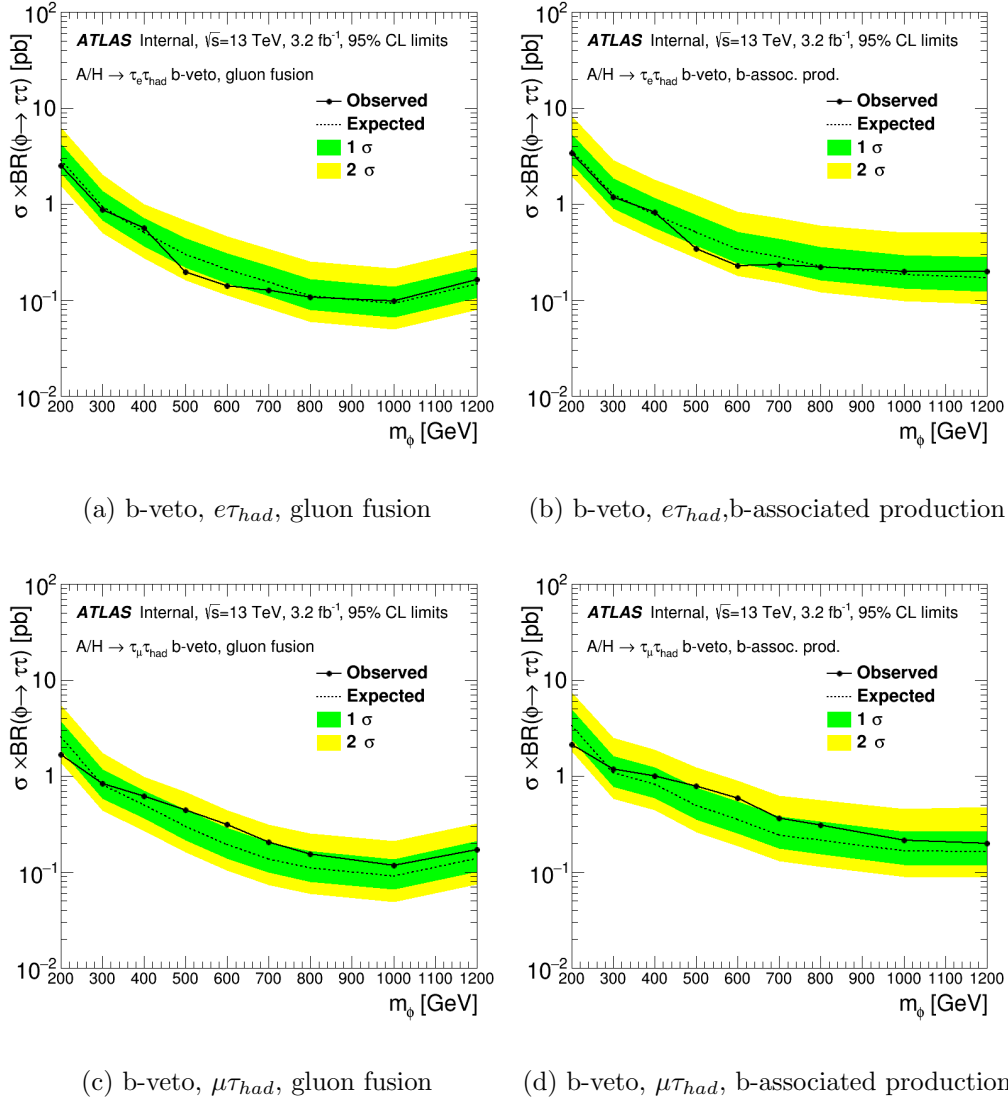


Figure 5.26: The 95% CL upper limit on the production times branching ratio to $\tau\tau$ of a single scalar boson produced via gluon fusion or b-associated production for 3210 pb^{-1} of integrated luminosity at 13 TeV. Each channel in the b-veto category is shown separately.

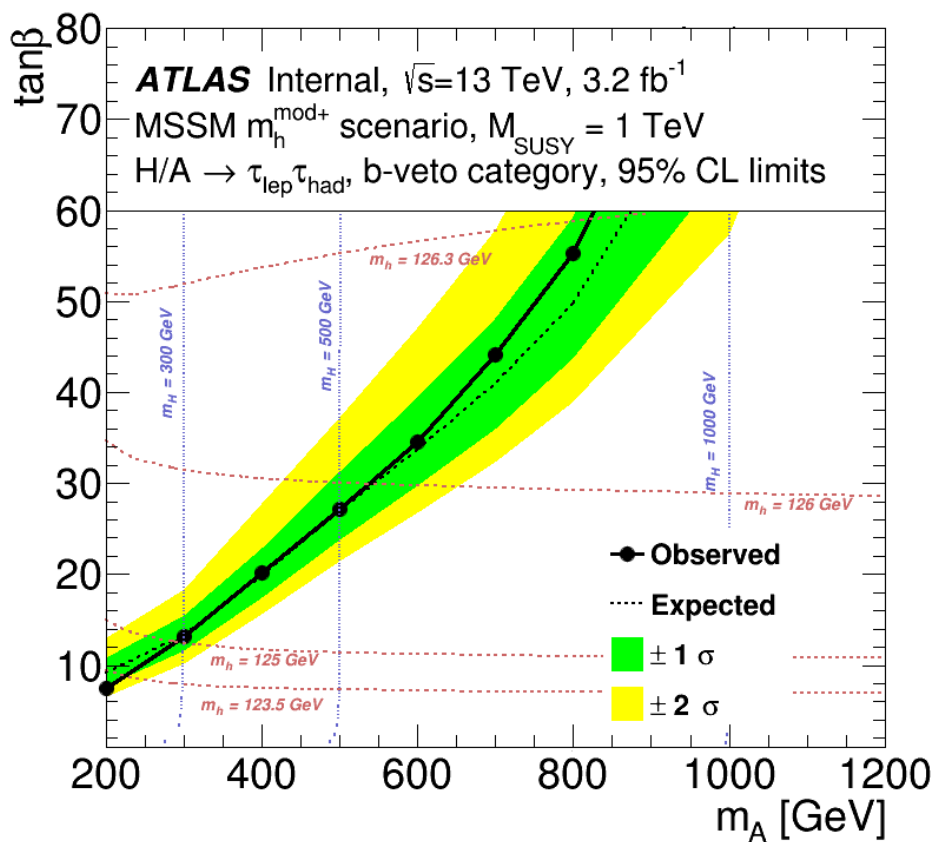


Figure 5.27: Interpretation of the results in the $m_h^{\text{mod}+}$ scenario of the MSSM.

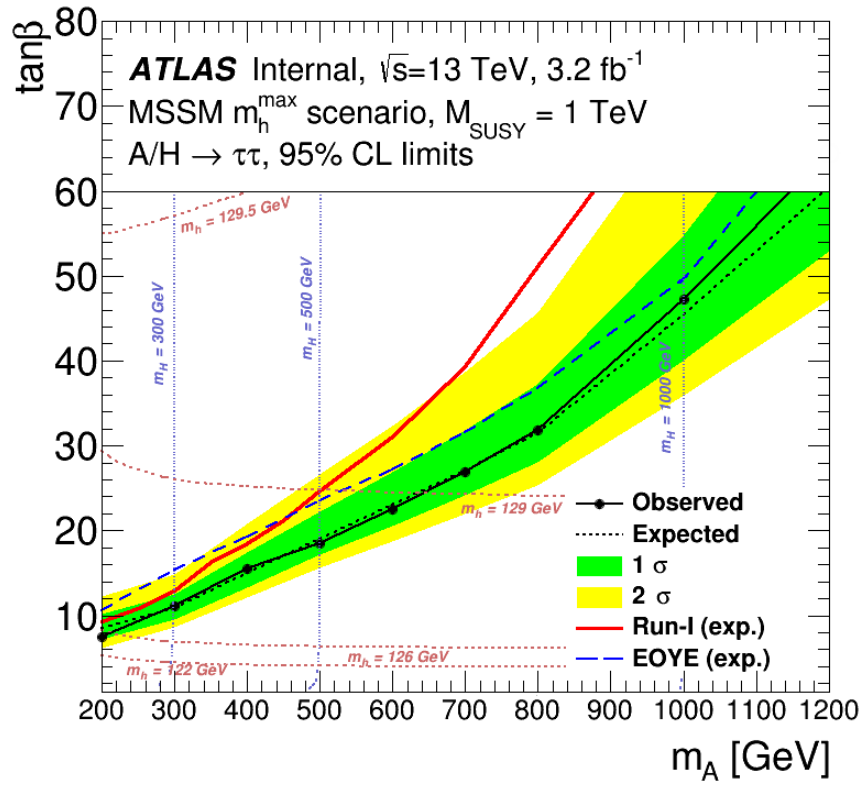


Figure 5.28: Comparison of the exclusion in the $m_A - \tan\beta$ plane of the m_h^{max} scenario for the combined $(\tau_{\text{lep}}\tau_{\text{had}} + \tau_{\text{had}}\tau_{\text{had}})$ Run-2 $H/A \rightarrow \tau\tau$ search and the Run-1 and preliminary Run-2 results (labeled “EOYE”).

Chapter 6

SUMMARY AND CONCLUSION

1308

1309

1310 The searches for a general CP-odd heavy Higgs boson A decaying to Zh in the $\ell\ell\tau_{lep}\tau_{had}$
1311 final state and for heavy neutral MSSM H/A Higgs bosons decaying to $\tau_{lep}\tau_{had}$ in events
1312 without b -tagged jets are presented. The former considers the gluon-fusion production mech-
1313 anism, while the latter considers both gluon-fusion and b -associated production modes. The
1314 Standard Model background is estimated using both simulated events and data-driven pre-
1315 dictions.

1316 Neither search shows statistically significant excesses compared to the SM prediction.
1317 Upper limits on cross section times branching ratio for a general 2HDM CP-odd A and
1318 neutral MSSM H/A are set. Results are also interpreted for different 2HDM and MSSM
1319 scenarios, with significant regions of the relevant parameter space being excluded.

1320 Though significant progress in probing the BSM Higgs sector has been made, large regions
1321 of the 2HDM and MSSM parameter space remain unexplored. The motivation for 2HDMs
1322 and supersymmetry are still powerful. As the LHC collects more data, refined versions of
1323 the present analyses are already being developed, and new physics may be just around the
1324 corner.

BIBLIOGRAPHY

1325

- 1326 [1] The ATLAS Collaboration, “Observation of a new particle in the search for the Standard
1327 Model Higgs boson with the ATLAS detector at the LHC”, *Phys. Lett.*, vol. B716, pp.
1328 1–29, 2012.
- 1329 [2] The CMS Collaboration, “Observation of a new boson at a mass of 125 GeV with the
1330 CMS experiment at the LHC”, *Phys. Lett.*, vol. B716, pp. 30–61, 2012.
- 1331 [3] The ATLAS Collaboration, “Study of the spin and parity of the Higgs boson in diboson
1332 decays with the ATLAS detector”, *Eur. Phys. J.*, vol. C75(10), p. 476, 2015. [Erratum:
1333 *Eur. Phys. J.*C76,no.3,152(2016)].
- 1334 [4] The ATLAS Collaboration, “Measurements of the Higgs boson production and decay
1335 rates and coupling strengths using pp collision data at $\sqrt{s} = 7$ and 8 TeV in the ATLAS
1336 experiment”, *Eur. Phys. J.*, vol. C76(1), p. 6, 2016.
- 1337 [5] The CMS Collaboration, “Precise determination of the mass of the Higgs boson and
1338 tests of compatibility of its couplings with the Standard Model predictions using proton
1339 collisions at 7 and 8 TeV”, *Eur. Phys. J.*, vol. C75(5), p. 212, 2015.
- 1340 [6] The CMS Collaboration, “Constraints on the spin-parity and anomalous HVV couplings
1341 of the Higgs boson in proton collisions at 7 and 8 TeV”, *Phys. Rev.*, vol. D92(1), p.
1342 012004, 2015.
- 1343 [7] The ATLAS Collaboration, “Evidence for the Higgs-boson Yukawa coupling to tau
1344 leptons with the ATLAS detector”, *JHEP*, vol. 04, p. 117, 2015.
- 1345 [8] The ATLAS Collaboration, “Search for the $b\bar{b}$ decay of the Standard Model Higgs boson
1346 in associated $(W/Z)H$ production with the ATLAS detector”, *JHEP*, vol. 01, p. 069,
1347 2015.
- 1348 [9] The CMS Collaboration, “Search for the Standard Model Higgs boson produced in
1349 association with a W or a Z boson and decaying to bottom quarks”, *Phys. Rev.*, vol.
1350 D89(1), p. 012003, 2014.
- 1351 [10] P. W. Higgs, “Broken symmetries, massless particles and gauge fields”, *Phys. Lett.*,
1352 vol. 12, pp. 132–133, 1964.

- 1353 [11] P. W. Higgs, “Broken Symmetries and the Masses of Gauge Bosons”, *Phys. Rev. Lett.*,
1354 vol. 13, pp. 508–509, 1964.
- 1355 [12] P. W. Higgs, “Spontaneous Symmetry Breakdown without Mass-
1356 less Bosons”, *Phys. Rev.*, vol. 145, pp. 1156–1163, 1966. URL
1357 <http://link.aps.org/doi/10.1103/PhysRev.145.1156>.
- 1358 [13] F. Englert and R. Brout, “Broken Symmetry and the Mass of Gauge
1359 Vector Mesons”, *Phys. Rev. Lett.*, vol. 13, pp. 321–323, 1964. URL
1360 <http://link.aps.org/doi/10.1103/PhysRevLett.13.321>.
- 1361 [14] G. S. Guralnik, C. R. Hagen and T. W. B. Kibble, “Global Conservation Laws
1362 and Massless Particles”, *Phys. Rev. Lett.*, vol. 13, pp. 585–587, 1964. URL
1363 <http://link.aps.org/doi/10.1103/PhysRevLett.13.585>.
- 1364 [15] S. P. Martin, “A Supersymmetry primer”, , 1997. [Adv. Ser. Direct. High Energy
1365 Phys.18,1(1998)].
- 1366 [16] P. Fayet, “Spontaneously broken supersymmetric theories of weak, electromagnetic
1367 and strong interactions”, *Physics Letters B*, vol. 69(4), pp. 489 – 494, 1977. URL
1368 <http://www.sciencedirect.com/science/article/pii/0370269377908528>.
- 1369 [17] J. Wess and B. Zumino, “Supergauge Transformations in Four-Dimensions”, *Nucl.*
1370 *Phys.*, vol. B70, pp. 39–50, 1974.
- 1371 [18] S. Dimopoulos and H. Georgi, “Softly broken supersymmetry and
1372 SU(5)”, *Nuclear Physics B*, vol. 193(1), pp. 150 – 162, 1981. URL
1373 <http://www.sciencedirect.com/science/article/pii/0550321381905228>.
- 1374 [19] G. C. Branco *et al.*, “Theory and phenomenology of two-Higgs-doublet models”, *Phys.*
1375 *Rept.*, vol. 516, pp. 1–102, 2012.
- 1376 [20] S. S. W. Greiner and E. Stein, *Quantum Chromodynamics* (Springer2007).
- 1377 [21] W. Greiner and B. Muller, *Gauge theory of weak interactions* (Springer1993). ISBN
1378 978-3-540-87842-1.
- 1379 [22] A. Djouadi, “The Anatomy of electro-weak symmetry breaking. II. The Higgs bosons
1380 in the minimal supersymmetric model”, *Phys. Rept.*, vol. 459, pp. 1–241, 2008.
- 1381 [23] A. Arbey *et al.*, “Implications of a 125 GeV Higgs for supersymmetric models”, *Phys.*
1382 *Lett.*, vol. B708, pp. 162–169, 2012.

- 1383 [24] A. Djouadi *et al.*, “The Minimal supersymmetric Standard Model:
1384 Group summary report”, in “GDR (Groupement De Recherche) - Su-
1385 persymetrie Montpellier, France, April 15-17, 1998”, (1998). URL
1386 https://inspirehep.net/record/481987/files/arXiv:hep-ph_9901246.pdf.
- 1387 [25] M. Carena *et al.*, “MSSM Higgs Boson Searches at the LHC: Benchmark Scenarios after
1388 the Discovery of a Higgs-like Particle”, *Eur. Phys. J.*, vol. C73(9), p. 2552, 2013.
- 1389 [26] L. H. C. S. W. Group, “BSM Higgs production cross sections at
1390 $\sqrt{s} = 13$ TeV (update in CERN Report 4 2016)”, , 2016. URL
1391 <https://twiki.cern.ch/twiki/bin/view/LHCPhysics/CERNYellowReportPageBSMAT13TeV>.
- 1392 [27] L. H. C. S. W. Group, “LHC Higgs Cross Section WG Picture Gallery”, , 2016. URL
1393 <https://twiki.cern.ch/twiki/bin/view/LHCPhysics/LHCHXSWGCrossSectionsFigures>.
- 1394 [28] L. Evans and P. Bryant, “LHC Machine”, *Journal of Instrumentation*, vol. 3(08), p.
1395 S08001, 2008. URL <http://stacks.iop.org/1748-0221/3/i=08/a=S08001>.
- 1396 [29] The ATLAS Collaboration, “The ATLAS Experiment at the CERN Large Hadron Col-
1397 lider”, *JINST*, vol. 3, p. S08003, 2008.
- 1398 [30] J. Alwall *et al.*, “MadGraph 5: going beyond”, *Journal of High Energy Physics*, vol.
1399 2011(6), pp. 1–40, 2011. URL [http://dx.doi.org/10.1007/JHEP06\(2011\)128](http://dx.doi.org/10.1007/JHEP06(2011)128).
- 1400 [31] T. Sjöstrand, S. Mrenna and P. Skands, “A brief introduction to PYTHIA 8.1”,
1401 *Computer Physics Communications*, vol. 178(11), pp. 852 – 867, 2008. URL
1402 <http://www.sciencedirect.com/science/article/pii/S0010465508000441>.
- 1403 [32] R. V. Harlander, S. Liebler and H. Mantler, “SusHi: A program for the calculation of
1404 Higgs production in gluon fusion and bottom-quark annihilation in the Standard Model
1405 and the MSSM”, *Comput. Phys. Commun.*, vol. 184, pp. 1605–1617, 2013.
- 1406 [33] D. Eriksson, J. Rathsman and O. Stal, “2HDMC: Two-Higgs-Doublet Model Calculator
1407 Physics and Manual”, *Comput. Phys. Commun.*, vol. 181, pp. 189–205, 2010.
- 1408 [34] T. Gleisberg *et al.*, “Event generation with SHERPA 1.1”, *Jour-
1409 nal of High Energy Physics*, vol. 2009(02), p. 007, 2009. URL
1410 <http://stacks.iop.org/1126-6708/2009/i=02/a=007>.
- 1411 [35] S. Frixione, P. Nason and C. Oleari, “Matching NLO QCD computations with parton
1412 shower simulations: the POWHEG method”, *Journal of High Energy Physics*, vol.
1413 2007(11), p. 070, 2007. URL <http://stacks.iop.org/1126-6708/2007/i=11/a=070>.

- 1414 [36] E. Re, “Single-top production with the POWHEG method”, *PoS*, vol. DIS2010, p. 172,
1415 2010.
- 1416 [37] B. P. Kersevan and E. Richter-Was, “The Monte Carlo event generator AcerMC versions
1417 2.0 to 3.8 with interfaces to PYTHIA 6.4, HERWIG 6.5 and ARIADNE 4.1”, *Comput.*
1418 *Phys. Commun.*, vol. 184, pp. 919–985, 2013.
- 1419 [38] The ATLAS Collaboration, “The ATLAS Simulation Infrastructure”, *Eur. Phys. J.*,
1420 vol. C70, pp. 823–874, 2010.
- 1421 [39] The ATLAS Collaboration, “Electron reconstruction and identification efficiency mea-
1422 surements with the ATLAS detector using the 2011 LHC proton-proton collision data”,
1423 *Eur. Phys. J.*, vol. C74(7), p. 2941, 2014.
- 1424 [40] The ATLAS Collaboration, “Electron and photon energy calibration with the ATLAS
1425 detector using LHC Run 1 data”, *Eur. Phys. J.*, vol. C74(10), p. 3071, 2014.
- 1426 [41] The ATLAS Collaboration, “Measurement of the muon reconstruction performance of
1427 the ATLAS detector using 2011 and 2012 LHC proton–proton collision data”, *Eur.*
1428 *Phys. J.*, vol. C74(11), p. 3130, 2014.
- 1429 [42] The ATLAS Collaboration, “Topological cell clustering in the ATLAS calorimeters and
1430 its performance in LHC Run 1”, , 2016.
- 1431 [43] M. Cacciari, G. P. Salam and G. Soyez, “The Anti-k(t) jet clustering algorithm”, *JHEP*,
1432 vol. 04, p. 063, 2008.
- 1433 [44] The ATLAS Collaboration, “Identification and energy calibration of hadronically de-
1434 caying tau leptons with the ATLAS experiment in pp collisions at $\sqrt{s}=8$ TeV”, *Eur.*
1435 *Phys. J.*, vol. C75(7), p. 303, 2015.
- 1436 [45] “Performance of Missing Transverse Momentum Reconstruction in ATLAS studied in
1437 Proton-Proton Collisions recorded in 2012 at 8 TeV”, (ATLAS-CONF-2013-082), 2013.
1438 URL <http://cds.cern.ch/record/1570993>.
- 1439 [46] A. Elagin, P. Murat, A. Pranko and A. Safonov, “A New Mass Reconstruction Technique
1440 for Resonances Decaying to di-tau”, *Nucl. Instrum. Meth.*, vol. A654, pp. 481–489, 2011.
- 1441 [47] P. Skands, “Introduction to QCD”, in “Proceedings, Theoretical Ad-
1442 vanced Study Institute in Elementary Particle Physics: Searching for New
1443 Physics at Small and Large Scales (TASI 2012)”, pp. 341–420 (2013). URL
1444 <https://inspirehep.net/record/1121892/files/arXiv:1207.2389.pdf>.

- 1445 [48] J. M. Campbell, R. K. Ellis and C. Williams, “Vector boson pair production at the
1446 LHC”, *JHEP*, vol. 07, p. 018, 2011.
- 1447 [49] S. Dittmaier *et al.*, “Handbook of LHC Higgs Cross Sections: 2. Differential Distribu-
1448 tions”, , 2012.
- 1449 [50] A. D. Martin, W. J. Stirling, R. S. Thorne and G. Watt, “Parton distributions for the
1450 LHC”, *Eur. Phys. J.*, vol. C63, pp. 189–285, 2009.
- 1451 [51] R. D. Ball *et al.*, “Impact of heavy quark masses on parton distributions and
1452 {LHC} phenomenology”, *Nuclear Physics B*, vol. 849(2), pp. 296 – 363, 2011. URL
1453 <http://www.sciencedirect.com/science/article/pii/S0550321311001842>.
- 1454 [52] The ATLAS Collaboration, “Search for a CP-odd Higgs boson decaying to Zh in pp
1455 collisions at $\sqrt{s} = 8$ TeV with the ATLAS detector”, *Phys. Lett.*, vol. B744, pp. 163–
1456 183, 2015.
- 1457 [53] S. Alioli, P. Nason, C. Oleari and E. Re, “NLO Higgs boson production via gluon fusion
1458 matched with shower in POWHEG”, *Journal of High Energy Physics*, vol. 2009(04), p.
1459 002, 2009. URL <http://stacks.iop.org/1126-6708/2009/i=04/a=002>.
- 1460 [54] T. Sjöstrand *et al.*, “An introduction to PYTHIA 8.2”, *Com-
1461 puter Physics Communications*, vol. 191, pp. 159 – 177, 2015. URL
1462 <http://www.sciencedirect.com/science/article/pii/S0010465515000442>.
- 1463 [55] T. Sjöstrand, S. Mrenna and P. Skands, “PYTHIA 6.4 physics and man-
1464 ual”, *Journal of High Energy Physics*, vol. 2006(05), p. 026, 2006. URL
1465 <http://stacks.iop.org/1126-6708/2006/i=05/a=026>.
- 1466 [56] J. Alwall *et al.*, “The automated computation of tree-level and next-to-leading
1467 order differential cross sections, and their matching to parton shower simula-
1468 tions”, *Journal of High Energy Physics*, vol. 2014(7), pp. 1–157, 2014. URL
1469 [http://dx.doi.org/10.1007/JHEP07\(2014\)079](http://dx.doi.org/10.1007/JHEP07(2014)079).
- 1470 [57] M. Wiesemann *et al.*, “Higgs production in association with bottom
1471 quarks”, *Journal of High Energy Physics*, vol. 2015(2), pp. 1–35, 2015. URL
1472 [http://dx.doi.org/10.1007/JHEP02\(2015\)132](http://dx.doi.org/10.1007/JHEP02(2015)132).
- 1473 [58] C. ATLAS *et al.*, “The simulation principle and performance of the ATLAS fast
1474 calorimeter simulation FastCaloSim”, *Tech. Rep. ATL-PHYS-PUB-2010-013*, CERN,
1475 Geneva, 2010. URL <https://cds.cern.ch/record/1300517>.

- 1476 [59] “Electron identification measurements in ATLAS using $\sqrt{s} = 13$ TeV data with 50 ns
1477 bunch spacing”, *Tech. Rep. ATL-PHYS-PUB-2015-041*, CERN, Geneva, 2015. URL
1478 <https://cds.cern.ch/record/2048202>.
- 1479 [60] The ATLAS Collaboration, “Muon reconstruction performance of the ATLAS detector
1480 in proton–proton collision data at $\sqrt{s} = 13$ TeV”, *Eur. Phys. J.*, vol. C76(5), p. 292,
1481 2016.
- 1482 [61] T. A. collaboration, “Pile-up subtraction and suppression for jets in ATLAS”, , 2013.
- 1483 [62] “Commissioning of the ATLAS b -tagging algorithms using $t\bar{t}$ events in early
1484 Run-2 data”, *Tech. Rep. ATL-PHYS-PUB-2015-039*, CERN, Geneva, 2015. URL
1485 <https://cds.cern.ch/record/2047871>.
- 1486 [63] “Performance of missing transverse momentum reconstruction for the ATLAS detector
1487 in the first proton-proton collisions at at $\sqrt{s} = 13$ TeV”, *Tech. Rep. ATL-PHYS-PUB-*
1488 *2015-027*, CERN, Geneva, 2015. URL <https://cds.cern.ch/record/2037904>.
- 1489 [64] D. Cavalli *et al.*, “Reconstruction of Soft Missing Transverse Momentum with Inner
1490 Detector Tracks”, *Tech. Rep. ATL-COM-PHYS-2015-209*, CERN, Geneva, 2015. URL
1491 <https://cds.cern.ch/record/2002888>, intended as backup for MET paper.
- 1492 [65] The ATLAS Collaboration, “Measurement of the Z/γ^* boson transverse momentum
1493 distribution in pp collisions at $\sqrt{s} = 7$ TeV with the ATLAS detector”, *JHEP*, vol. 09,
1494 p. 145, 2014.
- 1495 [66] “ATLAS Run 1 Pythia8 tunes”, *Tech. Rep. ATL-PHYS-PUB-2014-021*, CERN,
1496 Geneva, 2014. URL <https://cds.cern.ch/record/1966419>.
- 1497 [67] The ATLAS Collaboration, “Search for neutral Higgs bosons of the minimal supersym-
1498 metric Standard Model in pp collisions at $\sqrt{s} = 8$ TeV with the ATLAS detector”,
1499 *JHEP*, vol. 11, p. 056, 2014.
- 1500 [68] “Search for Neutral Minimal Supersymmetric Standard Model Higgs Bosons
1501 $H/A \rightarrow \tau\tau$ produced in pp collisions at $\sqrt{s} = 13$ TeV with the AT-
1502 LAS Detector”, *Tech. Rep. ATLAS-CONF-2015-061*, CERN, Geneva, 2015. URL
1503 <https://cds.cern.ch/record/2114827>.
- 1504 [69] P. Fayet, “Supersymmetry and Weak, Electromagnetic and Strong Interactions”, *Phys.*
1505 *Lett.*, vol. B64, p. 159, 1976.

- 1506 [70] P. Fayet, “Relations between the masses of the superpartners of
1507 leptons and quarks, the goldstino coupling and the neutral cur-
1508 rents”, *Physics Letters B*, vol. 84(4), pp. 416 – 420, 1979. URL
1509 <http://www.sciencedirect.com/science/article/pii/0370269379912292>.
- 1510 [71] A. L. Read, “Presentation of search results: the CL s technique”, *Journal*
1511 *of Physics G: Nuclear and Particle Physics*, vol. 28(10), p. 2693, 2002. URL
1512 <http://stacks.iop.org/0954-3899/28/i=10/a=313>.
- 1513 [72] L. Breiman, J. H. Friedman, R. A. Olshen and C. J. Stone, *Classification and Regression*
1514 *Trees* (Chapman & Hall, New York 1984).
- 1515 [73] A. Hoecker *et al.*, “TMVA: Toolkit for Multivariate Data Analysis”, *PoS*, vol. ACAT,
1516 p. 040, 2007.
- 1517 [74] K. Cranmer, “Practical Statistics for the LHC”, in “Proceedings, 2011 Eu-
1518 ropean School of High-Energy Physics (ESHEP 2011)”, pp. 267–308 (2015).
1519 URL <https://inspirehep.net/record/1356277/files/arXiv:1503.07622.pdf>,
1520 [,247(2015)].
- 1521 [75] G. Cowan, K. Cranmer, E. Gross and O. Vitells, “Asymptotic formulae for likelihood-
1522 based tests of new physics”, *Eur. Phys. J.*, vol. C71, p. 1554, 2011. [Erratum: *Eur.*
1523 *Phys. J.*C73,2501(2013)].

Appendix A

TAU IDENTIFICATION

1524

1525

1526 A description of the reconstruction procedure for hadronic taus in ATLAS is found in
1527 Sections 4.2 and 5.2. Unfortunately, generic overlap removal between hadronically decaying
1528 taus and QCD-jets usually does not meet the $\text{jet} \rightarrow \tau_{had}$ background rejection requirements
1529 of ATLAS analyses. Because the online reconstruction of hadronic taus and jets must be
1530 fast, it is easier to optimize the discrimination between the two with a dedicated offline
1531 algorithm. For the majority of Run-1 ATLAS analyses that involved τ_{had} 's, this algorithm
1532 was the TauID [44]. This appendix will describe in more detail how the TauID is able to
1533 distinguish hadronic taus from QCD jets.

1534 **A.1 Overview**

1535 The discrimination provided by the TauID is achieved through the use of Boosted Decision
1536 Trees (BDT's), a type of multivariate classifier [72]. A decision tree is fundamentally a
1537 branching collection of if-statements that assigns a classification score to any input given the
1538 path in the if-statement sequence the input followed. Because of their structural differences,
1539 separate BDT's are provided for 1-track and 3-track hadronic taus. The BDT development
1540 is done with the Toolkit for Multivariate Analysis (TMVA) [73].

1541 One of the advantages of BDT's is that the decision tree trains itself on what each if-
1542 statement (called *nodes*) should be, as well as the branching sequences they are applied in.
1543 This is done by giving two samples to the classifier that are representative of the events the
1544 user wishes to separate. For the case of the TauID, one is a collection of truth-matched τ_{had}
1545 objects from a simulated $Z \rightarrow \tau\tau$ sample, and the other is made of nearly all Run-1 data
1546 events collected by jet triggers. The BDT is told to find the optimal set of cuts that give

1547 maximum separation between the reconstructed taus from those two sets. The rejection of
 1548 background events is done by applying a cut on the classification score that the BDT outputs
 1549 (i.e. the BDT score). True- τ_{had} sample events receive a signal-like score close to 1, while the
 1550 multi-jet events receive a background-like score close to 0. A BDT score distribution for the
 1551 TauID can be seen in Figure A.1(a). To avoid biases due to differences in the p_T spectrum
 1552 of the samples, the multi-jet events are reweighted according to the true- τ_{had} transverse
 1553 momentum distribution. A similar reweighting is done for the distribution of the number
 1554 of primary vertices, since the simulated samples do not perfectly match the pileup profile
 1555 observed in data.

1556 To improve the rejection performance, the BDT classifier is also subjected to a reweighting
 1557 procedure called *boosting*. The TauID employs the most popular type of boosting algorithm,
 1558 called adaptive boosting or *AdaBoost*. Adaptive boosting consists of applying the classifier
 1559 sequentially and, at each iteration, reweight previously misclassified events by a boosting
 1560 weight. The boosting weight is defined as

$$\alpha = \frac{1 - \text{err}}{\text{err}}, \quad (\text{A.1})$$

1561 where err is the misclassification rate of the previous tree. Thus, a tree with a misclassification
 1562 rate of 20% will have its misclassified events weighted by a factor of 4, forcing the next
 1563 classifier to take these misclassified events into stronger consideration during its training.
 1564 After the boosting weight is applied, the samples are renormalized to their original scale so
 1565 that the event weight sum is constant. For *AdaBoost*, the classifier score of a boosted event
 1566 is given by

$$y_{\text{boost}} = \frac{1}{N_{\text{collection}}} \cdot \sum_i^{N_{\text{collection}}} \ln(\alpha_i) \cdot h_i(\mathbf{x}), \quad (\text{A.2})$$

1567 where $h_i(\mathbf{x})$ is the unboosted classification score of the i -th event using the input variable
 1568 set \mathbf{x} .

1569 It is important to note that one cannot give the BDT an endless number of variables to
 1570 select on, or allow it to have too large branching sequences (i.e. large *depth*), otherwise one

1571 runs into the issue of overtraining. Overtraining occurs because when the tree has excessive
 1572 depth, too many input variables and not enough event population, it will find progressively
 1573 finer cuts that exploit statistical effects in the training variable distributions that are not
 1574 representative of the physical processes trying to be separated. Since more depth and input
 1575 variables generally lead to higher separation power, one must find the optimal training setup
 1576 that is just short of causing overtrained behavior. One way to reduce overtraining is through
 1577 the practice of pruning, which removes nodes and branches that have low separation power.
 1578 In the end, one can check if the BDT classifier has been overtrained by comparing its perfor-
 1579 mance on training events and events from the same input samples that were not used in the
 1580 training (test events). For the TauID, roughly 1/3 of events of each sample are randomly
 1581 selected for testing purposes and kept in reserve, while the remaining 2/3 are used for the
 1582 training. Figure A.1(b) shows a comparison of the classification performance of an early
 1583 TauID tuning that suffered from overtraining. The classification performance is displayed as
 1584 the functional dependence of the rejection efficiency on the signal acceptance, i.e. the cut on
 1585 the BDT score used.

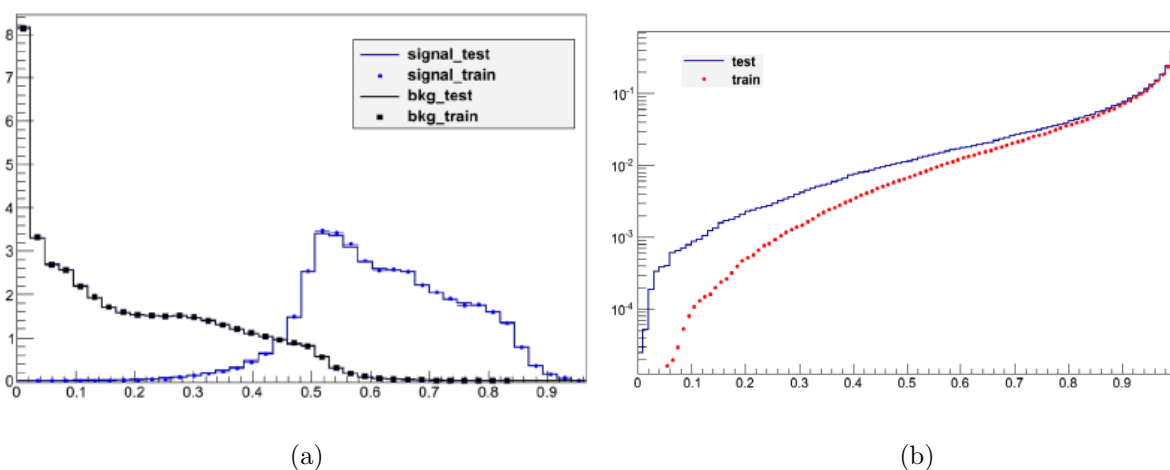


Figure A.1: A typical BDT score distribution from the TauID classifier (left) and an over-
 trained BDT from an early iteration of the TauID (right), where the background rejection
 with events used for training was higher than for events used for testing.

1586 A.2 Discriminating variables

1587 The chosen discriminating variables used to train the BDT classifier are those that capture
 1588 the differences between τ_{had} and QCD jets. Perhaps the most important difference between
 1589 the two is that τ_{had} -jets are generally more collimated than QCD jets. The former has a cone
 1590 angle of typically $\Delta R \lesssim 0.2$, compared to the latter's $\Delta R \sim 0.4$. Thus, it is useful to break
 1591 down the shower cone into two regions: the $\Delta R \leq 0.2$ *core region*, and the $0.2 < \Delta R < 0.4$
 1592 *isolation region*. With those two regions, it is easy to define several input variables centered
 1593 around the energy or track distribution in those two regions, such as the number of tracks
 1594 in the isolated region N_{track}^{iso} , and the centrality fraction f_{cent} , defined below. Because taus
 1595 have a finite lifetime, it is also possible to use variables that exploit the tau decay length.

1596 The Run-1 TauID was the first time in ATLAS that information from π^0 mesons orig-
 1597 inating from the τ_{had} were used in τ_{had} identification. The π^0 identification was done by
 1598 another BDT-based algorithm that used track and cluster information to identify deposits
 1599 likely due to neutral pions. The number of π^0 's in the jet is used as a discriminant variable,
 1600 and their energy and transverse momenta helps define two others. The full list of input
 1601 variables used to train the Run-1 TauID classifier is given below, with distributions shown
 1602 in Figures A.2-A.5.

- 1603 • Leading track momentum fraction (f_{track}): defined as the p_T of the leading track in the
 1604 core region divided by the sum of all the energy in all TopoClusters in the core region.
 1605 A correction based on the number of primary vertices is applied in order to remove
 1606 biases due to pile-up.
- 1607 • Central energy fraction (f_{cent}): the fraction of the energy from topo clusters with
 1608 $\Delta R < 0.1$ divided by that of the entire core region. Similarly to f_{track} , a correction
 1609 based on the number of primary vertices is applied to remove biases due to pile-up.
- 1610 • Number of π^0 mesons (N_{π}^0): the number of neutral pions reconstructed in the core
 1611 region.

- 1612 • Number of tracks in the isolation region ($N_{\text{track}}^{\text{iso}}$): Number of τ_{had} -associated tracks in
1613 the isolation region.
- 1614 • Track radius (R_{track}): the p_T -weighted angular distance of all charged tracks in the
1615 core and isolation regions.
- 1616 • Maximum ΔR (ΔR_{Max}): The ΔR between the reconstructed center of the τ_{had} cone
1617 and the the core region track with highest angular separation to it.
- 1618 • Transverse flight path significance (S_T^{flight}): The decay length of the secondary ver-
1619 tex reconstructed from the core tracks associated with the τ_{had} decay divided by its
1620 estimated uncertainty.
- 1621 • Leading track IP significance ($S_{\text{leadtrack}}$): The transverse impact parameter of the
1622 highest- p_T track with respect to the primary tau vertex divided by its estimated un-
1623 certainty.
- 1624 • Track mass (m_{track}): The invariant mass from the sum of all tracks in the core and
1625 isolation regions, assuming the tracks have the mass of a charged pion.
- 1626 • Track-plus- π^0 -system mass ($m_{\pi^0+\text{track}}$): Similar to m_{track} but also including all π^0
1627 mesons reconstructed in the core region.
- 1628 • Ratio of track-plus- π^0 -system p_T ($p_T^{\pi^0+\text{track}}/p_T$): Ratio of the transverse momentum
1629 estimated using both tracks and π^0 's to the p_T measured using only the calorimeter
1630 information.

1631 Not all variables are used for both 1-track and 3-track τ_{had} . Table A.1 summarizes which
1632 variables are used for each prong type.

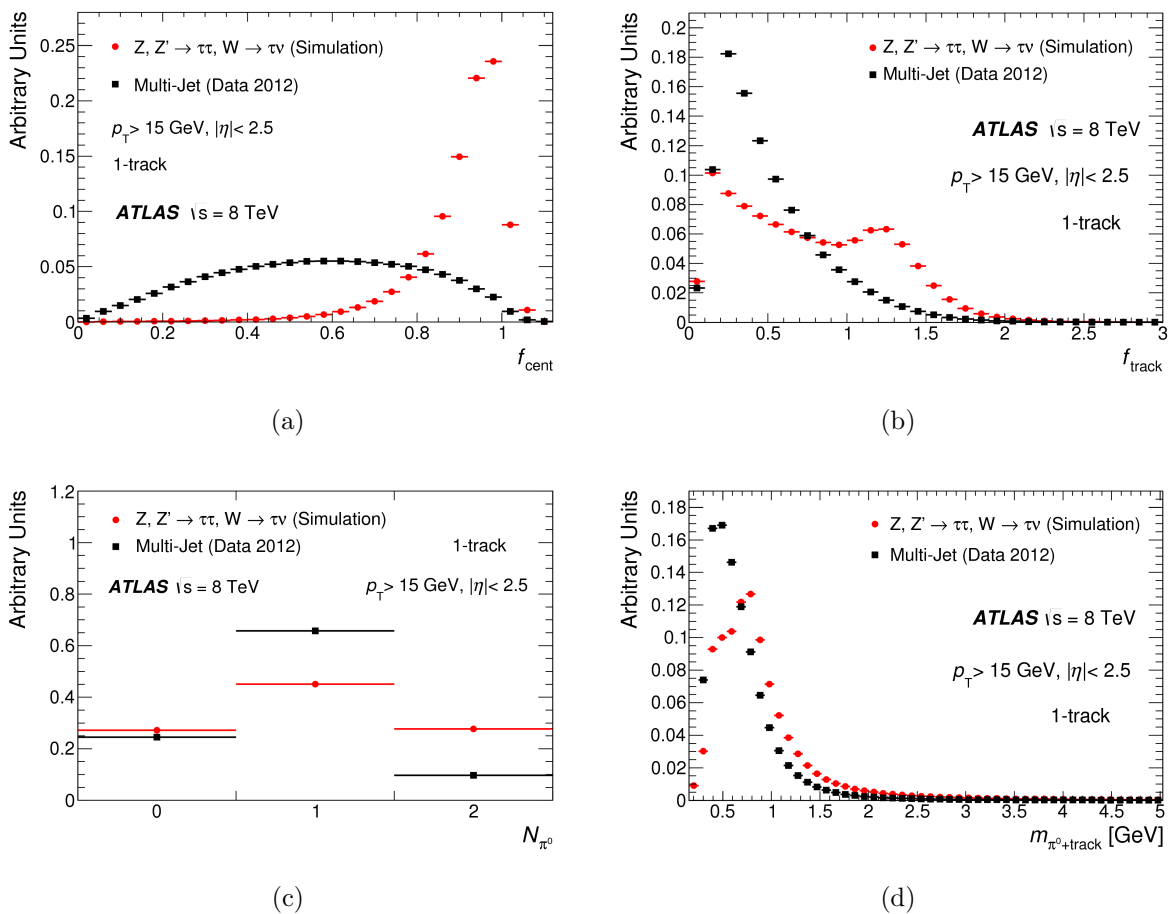


Figure A.2: Distributions of the variables used in the training of the Run-1 TauID classifier of 1-track hadronic taus.

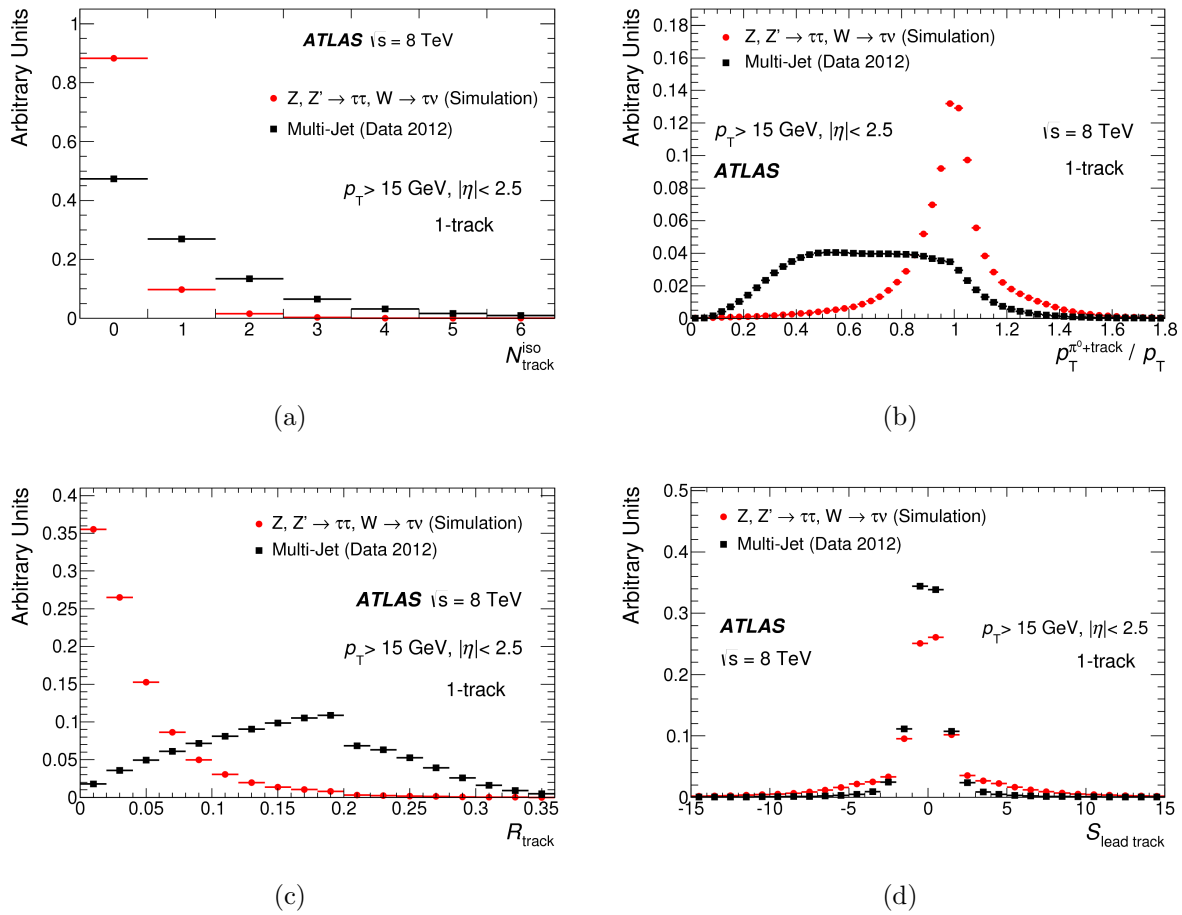


Figure A.3: Distributions of the variables used in the training of the Run-1 TauID classifier of 1-track hadronic taus.

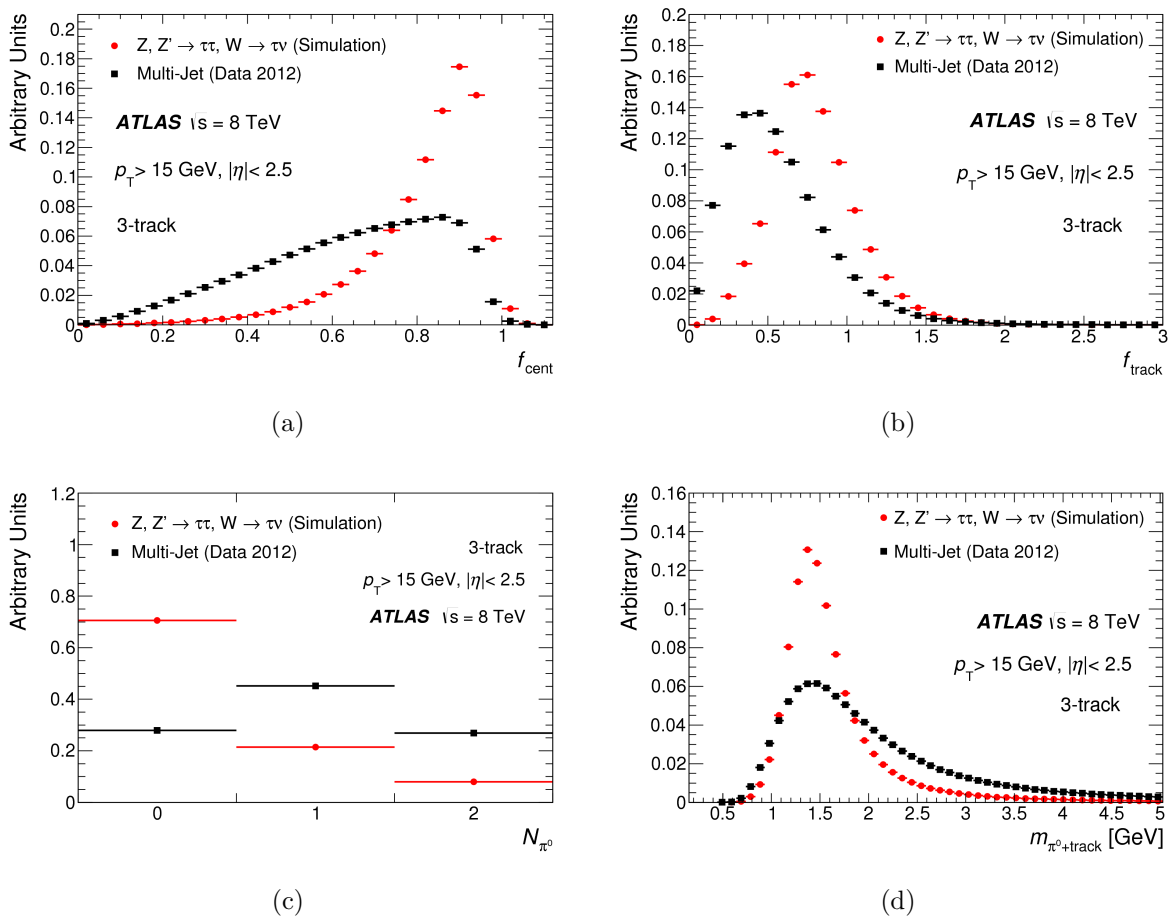


Figure A.4: Distributions of the variables used in the training of the Run-1 TauID classifier of 3-track hadronic taus.

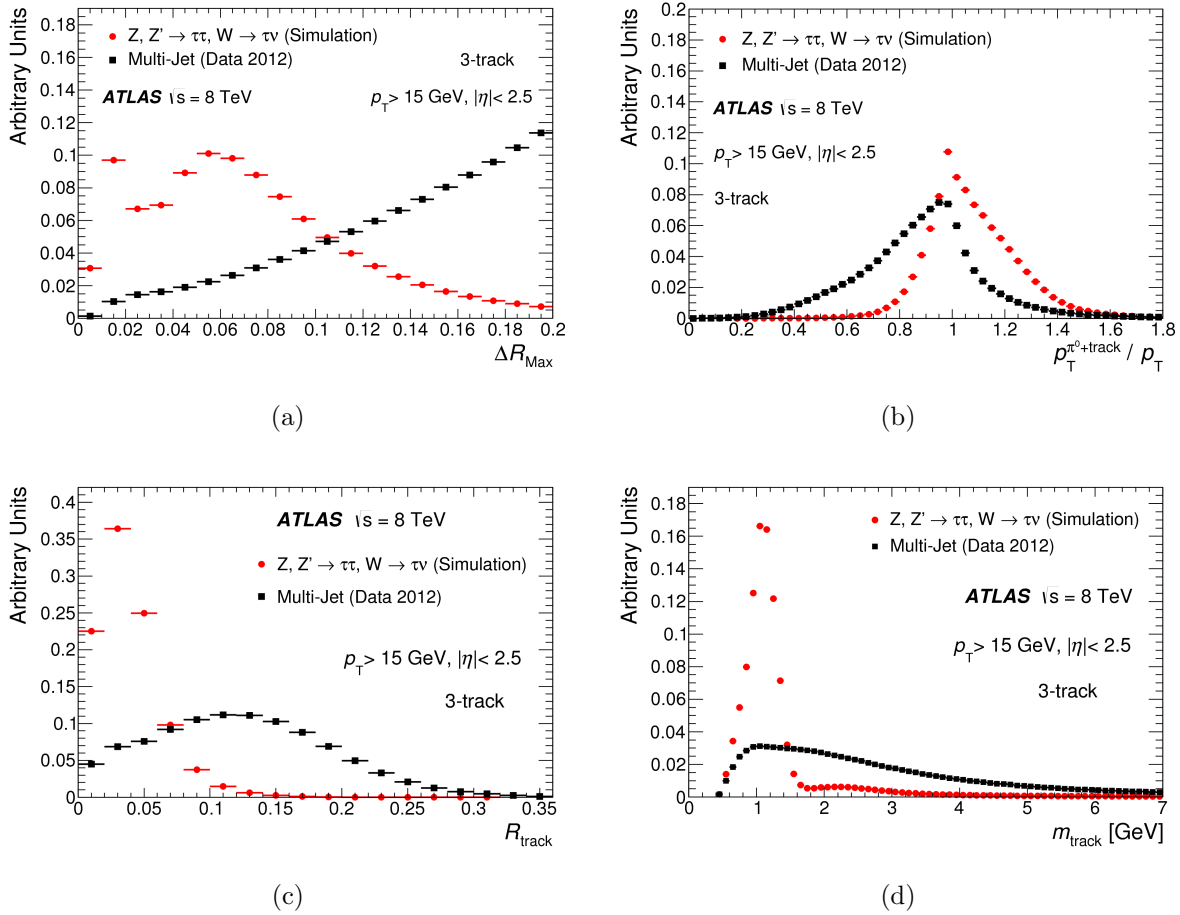


Figure A.5: Distributions of the variables used in the training of the Run-1 TauID classifier of 3-track hadronic taus.

Variable	1-track	3-track
f_{track}	•	•
f_{cent}	•	•
$S_{leadtrack}$	•	
N_{track}^{iso}	•	
R_{track}	•	•
ΔR_{Max}		•
S_T^{flight}		•
m_{track}		•
$p_T^{\pi^0+track}/p_T$	•	•
$m_{\pi^0+track}$	•	•
N_{π^0}	•	•

Table A.1: The list of variables used by the Run-1 TauID algorithm. The bullets indicate whether the variable is used in the training of the 1-track and/or 3-track classifier.

1633 **A.3 Final performance and working points**

1634 Hadronic taus produced at the LHC have a large range of transverse momentum. Because the
 1635 τ_{had} properties are correlated with p_T , using a single cut on the BDT score distribution would
 1636 lead to a corresponding p_T -dependent selection efficiency of the classifier. However, it is often
 1637 more convenient to have an identification requirement with constant signal efficiencies, so that
 1638 analyses can have predictable signal acceptances across their region of interest. To achieve
 1639 this, three working points representing different signal acceptance (and background rejection)
 1640 profiles are defined (in order of higher to lower signal acceptance): “loose”, “medium” and
 1641 “tight”, with identification efficiencies of 65% (70%), 55%(60%), 35%(40%) for 1-track (3-
 1642 track) hadronic taus, shown in Figure A.6. The final performance of the Run-1 TauID
 1643 classifier is shown in Figure A.7.

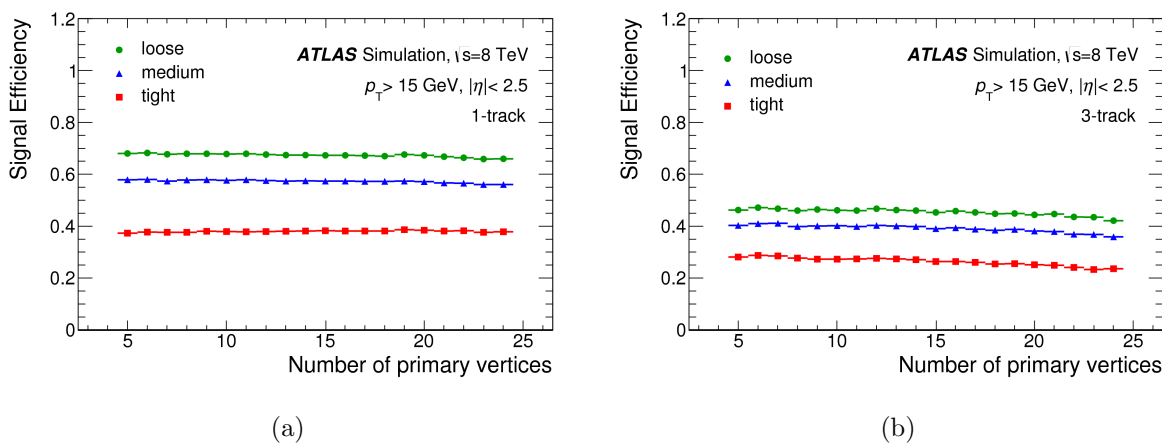


Figure A.6: The signal efficiency as a function of the reconstructed number of primary vertices for 1-track (a) and 3-track (b) hadronic taus.

1644 **A.4 Updates for Run-2**

1645 The TauID used in early Run-2 analysis is very similar to the Run-1 tuning. Because not
 1646 enough data was collected, the classifier is still trained on Run-1 data. The main difference is

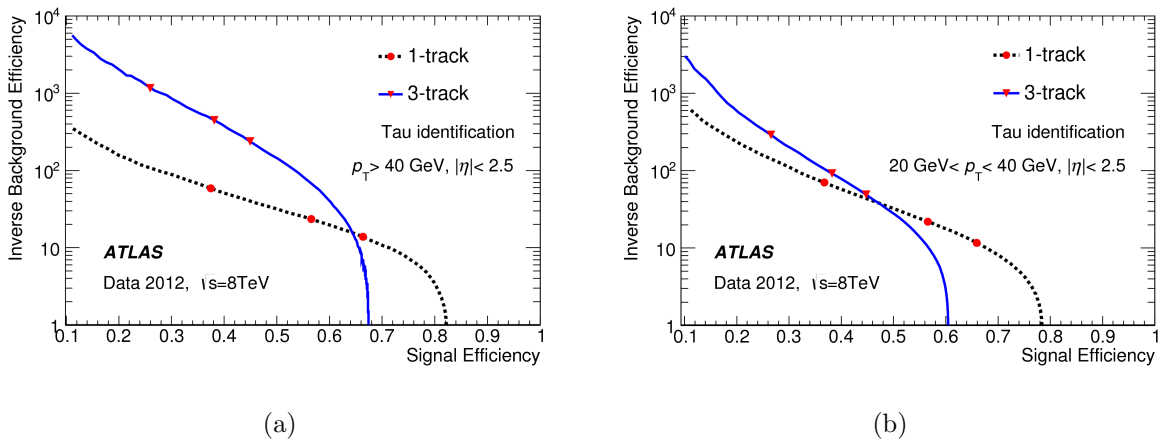


Figure A.7: The background rejection as a function of the signal efficiency for low ($p_T < 40$ GeV) and high ($p_T > 40$ GeV) transverse momenta hadronic taus. Red markers indicate the three efficiency working points described in the text.

1647 that variables defined using reconstructed π^0 , were replaced with variables that contain the
 1648 explicit low-level cluster energy information that were previously used in π^0 identification.
 1649 The new variables are:

- 1650 • $E_{\pi^\pm}^{EM} / E^{EM}$: the ratio of the EM calorimeter clusters associated with charged tracks to
 1651 the total total energy in the EM calorimeter associated with the tau decay.
- 1652 • p_T^{EM} / p_T^{tracks} : the ratio of the transverse momentum reconstructed in the EM calorimeter
 1653 divided by the transverse momentum of the track system.

1654 The final performance was very similar to the Run-1 TauID. However, the new configuration
 1655 uses lower-level input variables and is independent of the substructure algorithm, making it
 1656 more flexible.

Appendix B

STATISTICAL TREATMENT OF RESULTS

B.1 Overview

This Appendix aims to summarize the statistical methods used in interpreting the search results presented in this thesis. For a more detailed review, see Ref. [74].

The parameter of interest in both searches is the signal strength μ , given by the ratio of the fitted signal production cross section times branching ratio to its counterpart value predicted by the signal model being tested. Thus, the case $\mu = 0$ corresponds to signal events being absent, while $\mu = 1$ suggests a signal presence that is compatible with the assumption under study. The statistical compatibility of the result with different μ assumptions is done via a binned likelihood function from the product of Poisson probability terms. The different uncertainties are incorporated as nuisance parameters with gaussian distribution functions. Specifically, the likelihood for the signal strength μ is:

$$\mathcal{L}(\mu, \theta) = \prod_{j=\text{bin and channel}} \mathcal{F}_P(N_j | \mu \cdot s_j(\theta) + b_j(\theta)) \prod_{\theta_i} \mathcal{F}_G(\theta_i | 0, 1) \quad (\text{B.1})$$

where the terms in the equation above are:

- The number of observed events in bin j of the m_T^{tot} distribution N_j .
- The number of *expected* signal and background events s_j and b_j .
- The Poisson distribution $\mathcal{F}_P(N_j | \mu \cdot s_j + b_j)$ of N_j events with mean $\mu \cdot s_j + b_j$.
- The nuisance parameter vector θ .
- The gaussian distribution $\mathcal{F}_G(\theta_i | 0, 1)$ of the nuisance parameter θ_i , with mean 0 and variance 1.

1677 In case no excess of events is observed with regards to the background prediction, upper
 1678 limits on the production cross section times branching ratio of the signal process being
 1679 searched for are set. To derive this upper limit, the test statistic \tilde{q}_μ is defined:

$$\tilde{q}_\mu = \begin{cases} -2 \ln(\mathcal{L}(\mu, \hat{\theta}(\mu)) / \mathcal{L}(0, \hat{\theta}(0))) & \text{if } \hat{\mu} < 0 \\ -2 \ln(\mathcal{L}(\mu, \hat{\theta}(\mu)) / \mathcal{L}(\hat{\mu}, \hat{\theta})) & \text{if } 0 \leq \hat{\mu} \leq \mu \\ 0 & \text{if } \hat{\mu} > \mu \end{cases}$$

1680 where $\mathcal{L}(\mu, \theta)$ denotes the binned likelihood function, μ is the parameter of interest (i.e. the
 1681 signal strength parameter), and θ are the nuisance parameters. The pair $(\hat{\mu}, \hat{\theta})$ corresponds
 1682 to the global maximum of the likelihood, while $(x, \hat{\theta})$ corresponds to a maximum in which
 1683 $\mu = x$. Similarly, the nuisance parameters that maximize the likelihood for in the absence of
 1684 signal or for a certain value of μ are denoted by $\hat{\theta}(0)$ and $\hat{\theta}(\mu)$, respectively. Thus, the test
 1685 statistic for a certain μ value is compared to either the fitted value $\hat{\mu}$ (in case this is positive)
 1686 or to zero (in case this is negative). Signal strengths smaller than the global maximum value
 1687 can never be excluded. If some excess of events is observed, a similar test statistic is defined:

$$q_0 = \begin{cases} -2 \ln(\mathcal{L}(0, \hat{\theta}) / \mathcal{L}(\hat{\mu}, \hat{\theta})) & \text{if } \hat{\mu} \geq 0, \\ 0 & \text{if } \hat{\mu} < 0. \end{cases}$$

1688 In this case the test statistic is the ratio of the global maximum of the likelihood compared
 1689 to that for the null hypothesis (also referred to as the background only hypothesis).

1690 In order to exclude a hypothesis based on the observed data, the p -value must be calcu-
 1691 lated. The p -value is the probability of obtaining an equal or more extreme outcome were
 1692 the experiment to be repeated a large number of times. To reject signal hypotheses at 95%
 1693 confidence-level, we must find μ^{upper} such that

$$p_\mu = \int_{\tilde{q}_\mu, obs}^{\infty} f(\tilde{q}_\mu | \mu, \theta) d\tilde{q}_\mu = 5\%, \quad (\text{B.2})$$

1694 where $f(\hat{q}_\mu | \mu, \hat{\theta}(\mu, \text{obs}))$ is the probability distribution function (pdf) for a test statistic \tilde{q}_μ
 1695 However, it is possible that a downward fluctuation of the data causes μ^{upper} to become

1696 very small, beyond the sensitivity of the analysis being conducted. This problem is solved
 1697 by using the modified frequentist approach known as CL_S [71]. The CL_S method uses the
 1698 p -value ratio

$$p'_\mu \equiv \frac{p_\mu}{1 - p_b}, \quad (\text{B.3})$$

1699 where p_b is the p -value for the same test statistic but assuming a background-only hypothesis

$$p_b \equiv \int_{\tilde{q}_{\mu, \text{obs}}}^{\infty} f(\tilde{q}_\mu | 0, \hat{\theta}(\mu = 0, \text{obs})) d\tilde{q}_\mu. \quad (\text{B.4})$$

1700 We can also interpret the results directly in the parameter space of the models under consid-
 1701 eration by scanning the signal predictions of the points of the the 2HDM and MSSM planes
 1702 and checking if they are still allowed by the upper limits that were just set.

1703 It is important to note that it is not necessary to conduct a large number of pseudo-
 1704 experiments in order to get a probability distribution for the test statistic. It can be shown
 1705 that for sufficiently large data samples, the likelihood ratios that appear in the definitions of
 1706 the test statistic converge to specific analytical forms [75]. This result is called the *asymptotic*
 1707 *approximation*, and has been used in both searches presented in this thesis. For illustration
 1708 purposes, we write the asymptotic form of the *pdf* $f(\tilde{q}_\mu | \mu)$:

$$f(\tilde{q}_\mu | \mu) = \frac{1}{2} \delta(\tilde{q}_\mu) + \begin{cases} \frac{1}{2\sqrt{2\pi}} \frac{e^{-\tilde{q}_\mu/2}}{\sqrt{\tilde{q}_\mu}} & \text{if } 0 < \tilde{\mu} \leq \mu^2/\sigma^2, \\ \frac{1}{2\sqrt{2\pi}\sigma} \exp\left[-\left(\frac{\tilde{q}_\mu + \mu^2/\sigma^2}{2(2\mu/\sigma)^2}\right)^2\right] & \text{if } \tilde{q}_\mu > \mu^2/\sigma^2, \end{cases} \quad (\text{B.5})$$

1709 where σ is the variance of $\hat{\mu}$.

1710 It is also useful to check the impact of the nuisance parameters on the likelihood fit.
 1711 This is done by checking the shift in the signal strength, $\Delta\hat{\mu}$, due to $\pm 1\sigma$ variations of each
 1712 nuisance parameter. Confirming that the fitted nuisance parameter values are compatible
 1713 with their pre-fit assumptions is also a good indication the systematic uncertainties used are
 1714 adequate. Two typical fit scenarios are considered: an *unconditional* fit where μ is allowed
 1715 to float, and a *conditional* fit where $\mu = 1$. The former allows one to find the signal strength
 1716 that is most compatible with the observed data, while the latter allows one to see how
 1717 the nuisance parameters change to accommodate the signal assumption. Figures B.1-B.2

1718 show nuisance parameter rankings for the MSSM Higgs to ditau search. The parameters
 1719 are ranked according to their impact on $\hat{\mu}$, and black markers indicate the deviations of the
 1720 fitted parameter values from their initial assumptions.

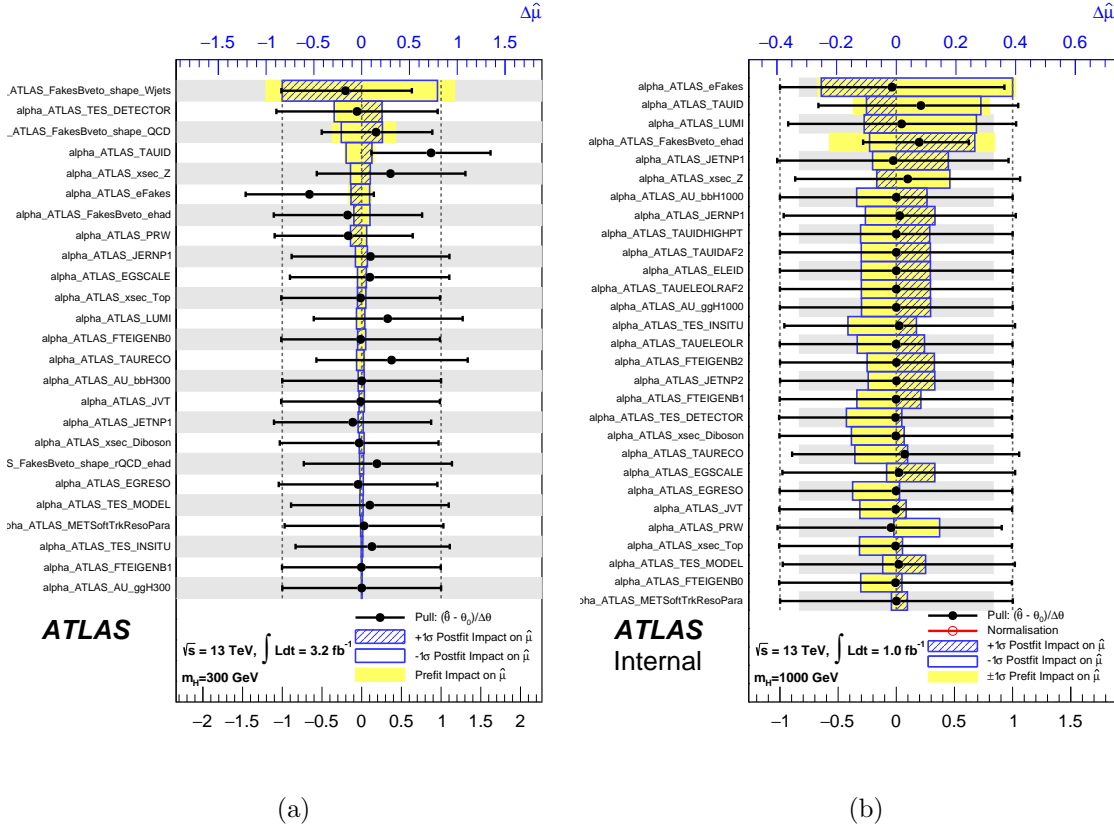


Figure B.1: Nuisance parameter rankings in the $e\tau_{had}$ channel for signal mass hypothesis of 300 and 1000 GeV.

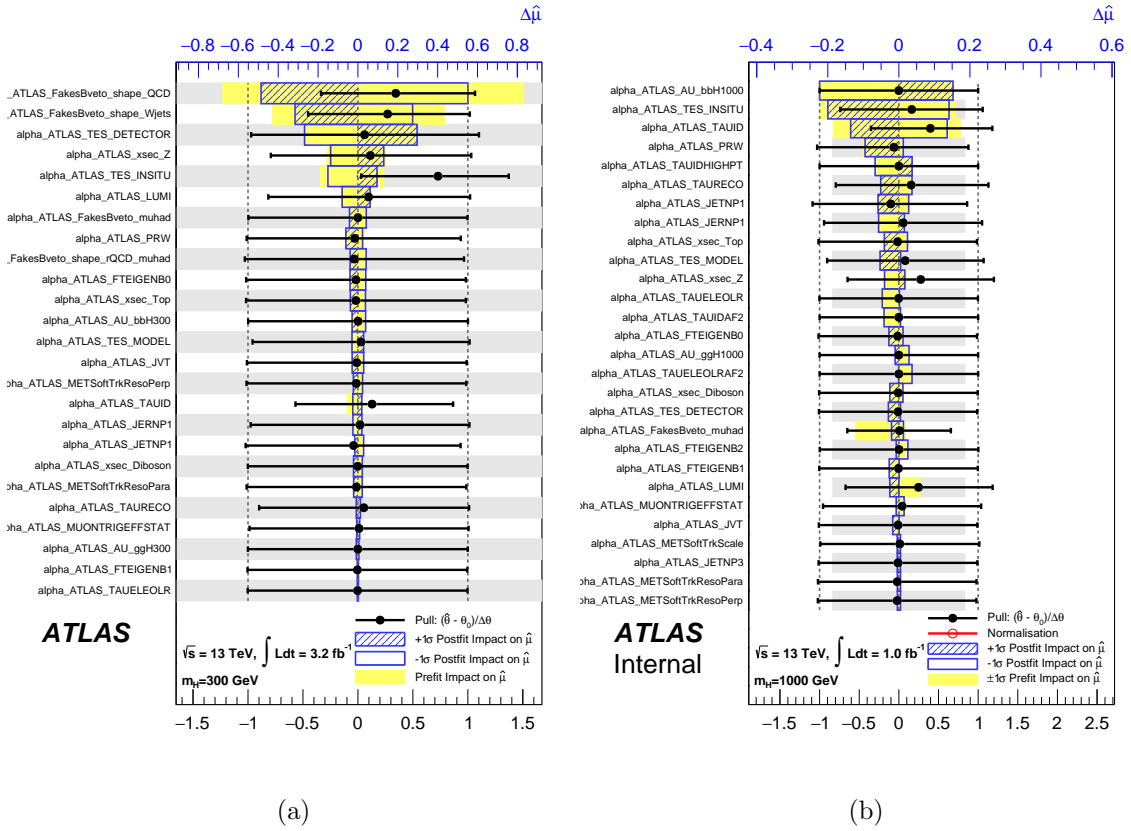


Figure B.2: Nuisance parameter rankings in the $\mu\tau_{had}$ (bottom) channel for signal mass hypothesis of 300 and 1000 GeV.